Montanuniversität Leoben

Dissertation

TEM investigations on interactions of dislocations with boundaries

Peter J. Imrich

Leoben, April 2015

April 2015

This doctoral thesis was typeset by the use of KOMA-Script and LaTeX 2_ε.

Erich Schmid Institute of Materials Science
Austrian Academy of Sciences
Department Materials Physics
Montanuniversität Leoben
Jahnstrasse 12
8700 Leoben
Austria
esi.oeaw.ac.at

Affidavit

I declare in lieu of oath, that I wrote this thesis and performed the associated research myself, using only literature cited in this volume.

Leoben, April 2015

Acknowledgments

Persuing a Doctorate is a long journey with many ups and downs. Frustration and euphoria take turns while the thesis gradually evolves. It is when you reach the end and look back that you realize your work would not have been possible without the help of countless people. Therefore I would like to express my gratitude to everyone who helped, supported and guided me along the way.

First of all I am grateful to my doctoral advisor Gerhard Dehm, who mentored me during the whole period of my thesis and gave me the opportunity to present my research at numerous conferences around the globe. Furthermore, I would like to thank Reinhard Pippan, who gave me financial support throughout my time in Leoben.

Micromechanical experiments are arduous to conduct and need elaborate equipment. Many people have helped me with the operation of instruments, by fruitful discussions and helpful advice. Foremost, I thank Christoph Kirchlechner who already supported me before the beginning of my diploma thesis and continued to do so all along my doctoral work. Thank you for being extremely helpful and open to discussions at all times! I warmly thank Daniel Kiener and Christian Motz for giving me valuable advice and aiding me during the preparation of manuscripts and Jörg Thomas and Zaoli Zhang for guidance regarding the transmission electron microscope.

I would like to express my appreciation to Gabriele Felber, Herwig Felber and Franz Hubner for all the sample pre-preparation, fabrication of sample holders and various technical gadgets. Many thanks to Victoria Schrutt, who was responsible for the administration and made a big effort to keep the institute running as smoothly as possible while being so cordial and cheerful.

My sincere thanks goes out to all my office colleagues, especially Andrea Bachmaier, Karoline Kormout, Thomas Leitner and Xiang Zhou, for providing an atmosphere to share work as well as laughter. I warmly thank Josef Kreith for advice on coordinate transformations and for discussions on the picoindenter, Berhard Völker for discussions on (in situ) TEM and Stefan Wurster for being helpful in so many areas from

instructions on furnaces to discussions on EBSD.

I would like to express my appreciation to everyone else at ESI, who contributed to the excellent work atmosphere and to all my friends who enriched my leisure time.

Finally I'd like to convey my heartfelt thanks to my family for their guidance, love and sympathy. Thank you for all the opportunities you gave me and your support at all times.

Abstract

The mechanical properties of materials strongly depend on their size when sample dimensions reach below several micrometers. Methods developed to conduct compression, tension and bending experiments on miniaturized single crystalline samples made it possible to understand this mechanical size effect that leads to an increase in yield strength with decreasing sample size. However, the majority of commercially used metals or alloys are multicrystalline, i. e., are an assembly of numerous single crystalline grains. Micromechanical testing provides the perfect platform to select specific grain boundaries and produce samples that incorporate a single boundary or multiple boundaries of the same type. This allows studying the effect of one grain boundary type on the deformation behavior. The use of in situ deformation techniques in the transmission electron microscope (TEM) adds the benefit of observing dislocation-grain boundary interactions while recording force-displacement data.

This thesis is aimed at further understanding the influence of grain boundaries on the mechanical behavior. Taperless Cu pillars of different sizes, reaching from 7 µm down to 200 nm in width were manufactured using focused ion beam (FIB) milling techniques and tested in situ inside a scanning electron microscope or a TEM. Bicrystalline samples incorporating an arbitrary large angle grain boundary parallel to the compression direction show an increase in yield strength and hardening and less serrated flow. Samples with a single coherent twin boundary along the compression axis on the other hand exhibit similar deformation characteristics as single crystals of the component grains. In situ TEM and scanning TEM deformation experiments on twinned samples confirm the lack of strengthening and no stress concentrations due to the twin boundary can be found in the tested orientation. A stochastic variation of dislocation density was found in the 200 nm sized samples, but never a complete dislocation starvation. Further experiments on 1 µm sized compression pillars comprised of several twin lamellas inclined to the compression direction reveal that the majority of deformation is taking place parallel to the boundaries.

Kurzfassung

Die mechanischen Eigenschaften von Materialien zeigen eine deutliche Größenabhängigkeit, wenn die Probendimensionen im Bereich weniger Mikrometer oder darunter liegen. Neuartige Methoden zur Durchführung mikromechanischer Druck-, Zug- und Biegeversuche machen es möglich diesen mikromechanischen Größeneffekt, der zu einer Steigerung der Festigkeit mit abnehmender Progengröße führt, zu verstehen. Der Großteil der kommerziell verwendeten Metalle bzw. Legierungen ist jedoch multikristallin, d. h. besteht aus einer Vielzahl einkristalliner Körner. Mikromechanische Methoden ermöglichen es nun miniaturisierte Proben herzustellen, die nur eine einzelne oder mehrere Korngrenzen der gleichen Art beinhalten, um deren Einfluss auf das Verformungsverhalten zu untersuchen. In situ Versuche im Transmissionselektronenmikroskop (TEM) erlauben neben der Aufzeichnung von Kraft-Verschiebungs-Kurven zudem die Beobachtung von Versetzungs-Korngrenzen-Wechselwirkungen.

Das Ziel dieser Arbeit ist es den Einfluss von Korngrenzen auf das Verformungsverhalten besser zu verstehen. Dafür wurden miniaturisierte Druckproben unterschiedlicher Größe von 200 nm bis 7 µm Dicke mittels Rasterionenmikroskop (FIB) hergestellt und in situ im Rasterelektronenmikroskop oder TEM verformt. Bikristalline Proben mit einer Großwinkelkorngrenze parallel zur Druckrichtung zeigen erhöhte Festigkeit, ausgeprägte Verfestigung und schwächer gezahntes Fließverhalten. Druckproben mit einer einzelnen kohärenten Zwillingsgrenze weisen dahingegen ein ähnliches Verformungsverhalten auf wie Einkristalle. In situ Versuche an Proben mit Zwillingsgrenze, die im TEM bzw. Raster-TEM Modus erfolgten, bestätigen diese Ergebnisse und zeigen, dass keine Spannungskonzentrationen im Bereich der Zwillingsgrenze vorhanden sind. Ferner wird eine stochastische Variation der Versetzungsdichte beobachtet, aber nie eine vollständige Verarmung an Versetzungen. Weitere Experimente an 1 µm großen Druckproben mit mehreren Zwillingsgrenzen die in einem Winkel zur Druckrichtung liegen, zeigen, dass der Großteil der Verformung parallel zu den Grenzflächen stattfindet.

Videre credere est
Seeing is believing

Contents

Abbreviations and Symbols

3D DDD	three dimensional discrete dislocation dynamics
CSL	coincidence site lattice
CTB	coherent twin boundary
FE	finite element
FIB	focused ion beam
FRS	Frank-Read source
GIS	gas injection system
GND	geometrically necessary dislocations
ISE	indentation size effect
LAGB	large angle grain boundary
MD	molecular dynamics
MS	macrosample
OFHC	oxygen-free high thermal conductivity
OIM	orientation imaging microscopy
SEM	scanning electron microscope
SSD	statistically stored dislocations
STEM	scanning transmission electron microscope
TEM	transmission electron microscope
Ag	silver
Al	aluminum
Au	gold
B	boron
Cu	copper
Mo	molybdenum
Ni	nickel
ϵ	plastic strain
$\dot{\epsilon}$	plastic strain rate
$\boldsymbol{g}$	slip direction
$\boldsymbol{n}$	glide plane normal

ν ..... Poisson's ratio
ρ ..... dislocation density
ρ_G ..... geometrically necessary dislocation density
ρ_S ..... statistically stored dislocation density
σ_0 ..... bulk strength
σ_0 ..... lattice resistance
σ_y ..... yield strength
τ ..... shear stress
Θ ..... rotation angle between transmitting slip systems
θ ..... rotation axis for the misorientation between two grains
a ..... interatomic spacing
b ..... Burgers vector
D ..... grain size
d ..... sample diameter
D_S ..... dislocation spacing
E ..... Young's modulus
G ..... shear modulus
hkl ..... Miller indices for crystallographic planes or directions
k ..... Hall-Petch strengthening coefficient
L ..... size of dislocation source
L_p ..... pile-up length
N ..... number of dislocations in a pile-up
n ..... scaling exponent for the mechanical size effect

1 Introduction

The majority of commercially used metals or alloys are multicrystalline, i. e., comprised of numerous grains between a couple of micrometers down to several nanometers in size. It was found, that the strength of metals scales inversely proportional to the grain size, giving rise to a multitude of industrial processes that lead to a reduction in grain size, nowadays essential for the production of structural materials. The reason for this improvement in mechanical properties lies in the interactions of dislocations, the carrier for deformation in metals, and the grain boundaries that separate individual single crystalline grains. While it is easy to describe the strength increase in macroscopic dimensions, the exact effects of specific grain boundaries on the deformation behavior remain unknown. Mechanical testing techniques that were developed to investigate the deformation behavior of miniaturized samples from several microns down to tens of nanometers provide the perfect platform to produce samples that contain only a single boundary or multiple boundaries of the same type. In situ mechanical testing inside the scanning electron microscope or the transmission electron microscope provides additional information on surface topography or dislocation activity of the sample, respectively. The next chapter will briefly introduce the concept of grain boundaries, their classification and influence on materials deformation as well as small scale materials behavior.

2

Basic Concepts and Literature

2.1. Grain boundaries

The interface between two crystallites of the same phase is called grain boundary. It is a planar defect in the material and defined by the orientation of both grains and the orientation of the boundary plane. Specifying all of them separately would lead to an over-determined system; only five parameters are needed to define a grain boundary:

- 2 parameters for the rotation axis $\boldsymbol{o}^*$
- 1 parameter for the rotation angle θ
- 2 parameters for the boundary plane in relation to one grain

Methods to describe the misorientation between two grains include the Rodrigues-Frank vector[1], Euler angles and quaternions[2]. In praxis, grain boundaries are often defined by specifying the grain boundary plane for both crystals, A and B as well as the rotation axis and the rotation angle: $\theta^\circ[h_o k_o l_o], (h_{nA} k_{nA} l_{nA})/(h_{nB} k_{nB} l_{nB})$. This notation provides a quicker view on the crystallography of the boundary.

*The three-dimensional direction of a unit vector is defined by two parameters; a third one is only needed if the magnitude of the vector is important (in this case it defines the rotation angle)

There are different ways to classify grain boundaries, the simplest method is to divide them into small- and large-angle grain boundaries[3]. Small angle grain boundaries with a misorientation of $\lesssim 15°$ can be realized by an array of dislocations in the boundary plane. A sequence of edge dislocations lead to a symmetrical tilt boundary, where the rotation vector lies in the boundary plane (Fig. 2.1 a). A network of at least two types of screw dislocations can produce a twist boundary, where the rotation vector is normal to the boundary plane (Fig. 2.1 c).

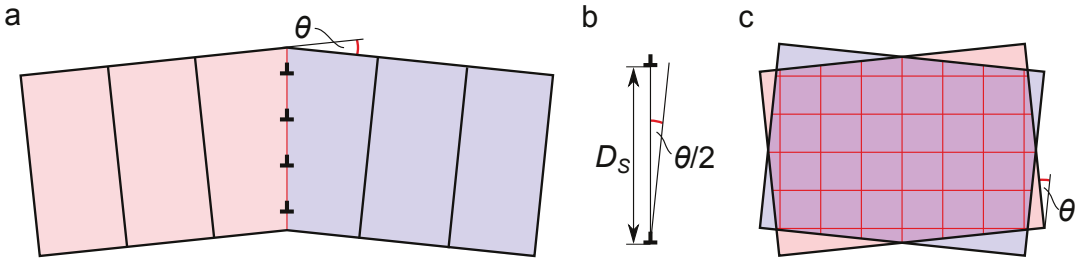

Figure 2.1.: (a) Tilt grain boundary with a sequence of edge dislocations, (b) distance between dislocations, (c) twist grain boundary with two sets of screw dislocations.

For a symmetrical tilt boundary a simple relationship between the distance D_S between dislocations and the tilt angle θ can be given:

$$\sin\frac{\theta}{2} = \frac{b}{2D_S} \tag{2.1}$$

with b being the Burgers vector of the edge dislocation (Fig. 2.1 b). For low θ the distance between the dislocations reduces to $D_S \approx b/\theta$. When the misorientation angle increases ($\gtrsim 15°$) the dislocation distance gets shorter and shorter until it is energetically unfavorable.

2.1.1. Coincidence Site Lattice Theory

Large angle grain boundaries normally feature a more complex interface structure that cannot be described by simple arrays of dislocations. For special orientation relationships between two crystals, however, lattice points of both crystals coincide. Such boundaries are classified by the coincidence site lattice (CSL) theory[4]. The ratio of coincidence sites to the total number of sites gives the degree of matching. This leads to a ratio of 1 for low angle grain boundaries, since the distortion is accommodated only by dislocations, thus making them $\Sigma 1$ boundaries. Twin boundaries, which will be discussed shortly are $\Sigma 3$ boundaries, meaning that 1/3 of the lattice points of both crystals match. Small deviations from the perfect CSL orientation are

again accounted for by regularly spaced dislocations since CSL boundaries tend to have lower grain boundary energies than arbitrary large angle grain boundaries[5].

2.1.2. Twin boundaries

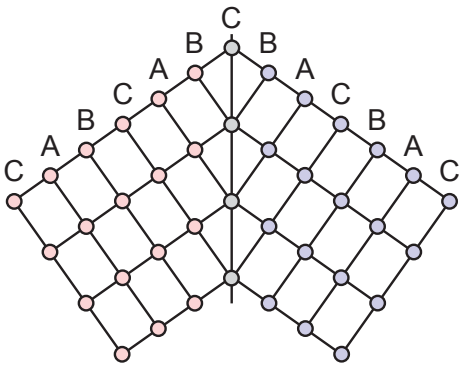

Figure 2.2.: Atoms at a coherent (111) twin boundary viewed in $[11\bar{2}]$ direction. The stacking sequence of (111) planes over the boundary is $ABCBA$.

Coherent twin boundaries (CTB) have a special low energy configuration that does not include dislocations at the interface while preserving dense packing. Figure 2.2 shows a CTB with (111) boundary plane, viewed in the $[11\bar{2}]$ direction. In a face centered cubic (fcc) metal this boundary is produced by a stacking sequence of $\{111\}$ planes of $ABCBA$ with C being the twin plane. This can be realized by a rotation of 60° or 180° around $\langle 111 \rangle$, a rotation of 70.53° around $\langle 110 \rangle$ or by mirroring the crystal across a $\{111\}$ plane. For a CTB the boundary plane is always of $\{111\}$ type, while the same misorientation between two grains with a different grain boundary plane (e. g. $\{112\}$) produces incoherent twin boundaries. In materials with low stacking fault energy such as Ag, Au, Cu and fcc alloys twin boundaries are often observed, especially after deformation followed by an annealing step (annealing twins).

2.2. Influence of grain boundaries on the mechanical behavior

Real materials are seldom single crystalline, but contain numerous single crystalline grains that are separated by grain boundaries. Hall and Petch[6,7] showed that the yield strength σ_y of polycrystalline materials depend on the average grain size D,

which is described by the Hall-Petch relationship:

$$\sigma_y = \sigma_0 + \frac{k}{\sqrt{D}} \tag{2.2}$$

Here σ_0 is the lattice resistance and k the strengthening coefficient, both constants for a specific material. The strength increase is due to the boundaries acting as barriers for dislocation movement; for smaller grains, the mean free path for dislocations is reduced and dislocations pile up at grain boundaries. A reduction in grain size leads to higher strengths which is widely used to improve materials properties by grain refinement. New techniques made it possible to produce metals with very small grains below 100 nm in size which are reported to be much stronger than coarse grained materials[8,9]. A material that has recently received tremendous attention includes a high percentage of coherent twin boundaries. Nanotwinned Cu for example, consisting of ultra-fine grains ($\sim$500 nm) and twin lamellas from 100 nm down to several nanometers in width shows exceptional strength and unexpectedly high ductility[10].

2.2.1. Dislocation-Boundary Interactions

The interaction mechanisms between dislocations and grain boundaries can be manifold. Depending on the misorientation between both grains, the grain boundary orientation and the slip system of the impinging dislocations, pile-up, absorption into the grain boundary or slip transmission can be the case. Latter permits dislocations to transfer from one grain to the other, thus providing a longer mean free path and greater deformation of the sample.

Several models for the prediction of slip transmission in bicrystals were introduced and some proved to accurately predict dislocation transmission through boundaries. As summarized by Clark et al.[11], these are:

1. The angle Θ by which dislocations will have to rotate their line direction has to be minimized[12](see Fig. 2.3). Equivalently, the factor M which is defined as:

$$M = \boldsymbol{L_1} \cdot \boldsymbol{L_i} \tag{2.3}$$

   has to be maximum. $\boldsymbol{L_1}$ and $\boldsymbol{L_i}$ are the lines of intersection between the grain boundary and the incoming or outgoing slip system, respectively.

2. The shear stress acting on the transmitted dislocation is maximum[13], which is the case when:

$$N = (\boldsymbol{n_1} \cdot \boldsymbol{n_i})(\boldsymbol{g_1} \cdot \boldsymbol{g_i}) + (\boldsymbol{n_1} \cdot \boldsymbol{g_i})(\boldsymbol{g_1} \cdot \boldsymbol{n_i}) \tag{2.4}$$

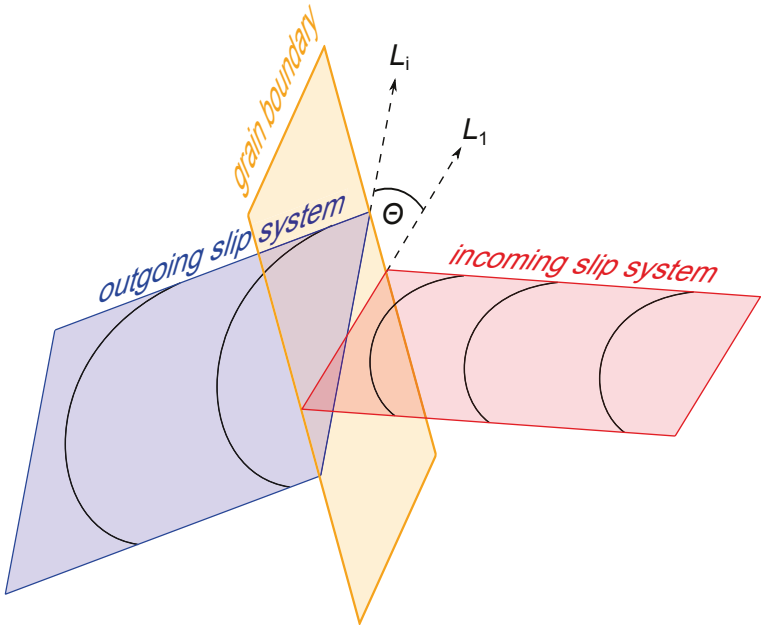

Figure 2.3.: Transmission of dislocations at a grain boundary.

is maximum. With $\boldsymbol{n_1}$ and $\boldsymbol{g_1}$ being the incoming slip plane normal and slip direction, respectively and $\boldsymbol{n_i}$ and $\boldsymbol{g_i}$ the slip plane normal and slip direction of all slip systems in the adjacent grain.

3. If two or more slip directions have similar shear stresses, the one that minimizes the energy of the residual grain boundary dislocation is preferred[14]. The Burgers vector of the residual dislocation ($\boldsymbol{b_r}$) is simply the difference between incoming ($\boldsymbol{b_1}$) and outgoing Burgers vector ($\boldsymbol{b_i}$):

$$\boldsymbol{b_r} = \boldsymbol{b_1} - \boldsymbol{b_i} \tag{2.5}$$

The importance of residual grain boundaries increases when numerous dislocations are transmitted in the same region and lots of residual grain boundary dislocations are generated. Then other slip systems which reduce this number can be more favorable[14].

2.3. Small scale materials behavior of single crystals

Already in 1956 Brenner[15] showed that the tensile stresses of metallic whiskers in the low micrometer region exhibit exceptional strengths, close to theoretical values. Interestingly, the yield strengths increased for smaller whiskers, scaling approximately

with the inverse of the diameter. He argued that this increase is due to the distribution of external defects, occasional grain boundaries or internal defects such as Frank Read Sources. The shear stress τ required to activate such a dislocation source depicted in Fig. 2.4 is given as:

$$\tau = \frac{Gb}{L} \tag{2.6}$$

with G being the shear modulus, b the Burgers vector and L the distance between the pinning points.

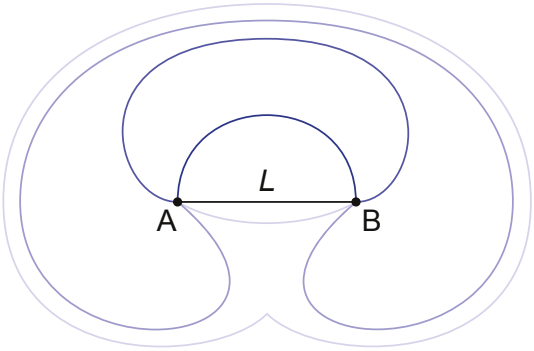

Figure 2.4.: Frank Read dislocation source with pinning points A and B and length L.

Experiments on thin films, small bending beams and torsion of thin wires, brought forward a theory that uses strain gradients to explain the mechanical size effect in yield strength called strain gradient plasticity[16]. It includes the idea of geometrically necessary dislocations (GND) which are required to accommodate the non-uniform deformation of the material. These dislocations are of the same type and their density ρ_G is proportional to the strain gradient of the material. Smaller bending beams for example feature a higher stress- and therefore a higher strain-gradient, resulting in increased GND densities. These dislocations lead to Taylor hardening and can be added to the density of statistically stored dislocations (SSD) ρ_S in a Taylor relationship:

$$\tau_y = CGb\sqrt{\rho_S + \rho_G} \tag{2.7}$$

with C being a constant in the range of 0.3[17]. This theory was also used to describe the increase in hardness that was found for decreasing indentation depths for nanoindentation experiments, called indentation size effect (ISE)[18]. However, strain gradient plasticity failed to explain the mechanical size effect that was found for small pillars deformed by uniaxial deformation that do not exhibit strain gradients[19]. This sparked new interest in the study of micron-sized samples and the introduction of focused ion beam (FIB) systems provided a useful instrument to manufacture

miniaturized compression[20], tension[21] and bending[22] samples. Experimental results proved that higher yield stresses are reached with decreasing diameter, following a power law behavior:

$$\sigma_y = \sigma_0 + kd^{-n} \tag{2.8}$$

linking the yield strength σ_y to the sample diameter d with a scaling exponent n, similar to Eq. 2.2, σ_0 being the bulk strength and k a materials constant. The value for n was initially proposed as ~ 0.6 for fcc metals[23] but remained a controversial subject, since it was shown to depend on many factors[24] and researchers go as far as claiming a constant factor of 1 for all materials[25]. Despite the disputed scaling parameter, the reasons for the mechanical size effect are generally agreed on. Several mechanisms operate simultaneously depending on sample size, dislocation density and crystal structure. For fcc metals, these are:

1. *Truncation Hardening*
   The decrease in sample size leads to a truncation of dislocation sources due to an intersection with the surface. Smaller dislocation sources (being of Frank Read or single armed type) need higher activation stresses, as shown in Eq. 2.6 and result in an increase in yield strength[26].

2. *Exhaustion Hardening*
   Due to the interaction of dislocations with obstacles (e. g., dislocation pile-up) a dislocation source can cease to operate. An increase in stress is needed to reactivate the original or activate a new dislocation source[27].

3. *Starvation Hardening*
   The probability of dislocation annihilation at a nearby free surface is higher for smaller samples resulting in a reduced chance of dislocation multiplication through dislocation-dislocation interactions. The decrease in dislocation density can lead to a lack of dislocation sources and the need to nucleate dislocations from the free surface which requires higher stresses[28].

4. *Source Statistics*
   The number of dislocations and dislocation sources decreases with reduced sample size and dislocation density. The statistical variation of source lengths and slip systems can lead to a lack of dislocation sources on slip systems with high Schmid factors and hence an increase in strength combined with a stochastic variation of yield stresses for small samples[29,30].

2.4. Influence of grain boundaries in microsamples

It is easy to describe the strengthening due to grain boundaries on a continuum level as mentioned in Sec. 2.2; yet, the Hall-Petch relationship does not incorporate the discrete dislocation-grain boundary interaction processes that are dependent on many factors including boundary type, Schmid factors in both grains and stress-levels. Since it is impractical to extract the behavior of single grain boundaries by deforming polycrystalline materials with numerous grains, it makes sense to test samples which are comprised of very few grains, preferably only two (bicrystals). The use of micromechanical methods for testing grain boundaries entails multiple benefits: (i) Bicrystalline samples can be prepared locally at selected grain boundaries providing that the grain size is large enough. (ii) The mean free path from either grain to the boundary is smaller, leading to an increased influence of dislocation-boundary interactions compared to dislocation-dislocation interactions.

The influence of boundaries on the deformation behavior of micromechanical samples can be manifold. A vertical separation of a single crystalline micropillar into two half-pillars (Fig. 2.5 b) will already lead to an increase in strength due to the mechanical size effect mentioned in Sec. 2.3, since the smallest dimension of a micromechanical sample defines the strength[31]. If both parts are joined together, forming a grain boundary at the intersection, the increase in strength and hardening behavior will depend strongly on the boundary type and two cases represent the possible extremes. An impenetrable boundary will lead to strong dislocation pile-up and consequently hardening of the pillar. Furthermore, a decreased source size that can be accommodated by each grain in the pillar results in higher strengths. For a penetrable boundary the barrier strength and the applied stress (that is dependent on pillar size) will determine the impact on stress-strain behavior.

In the previous years several groups have studied small scale behavior of interfaces, including grain boundaries and phase boundaries. Experiments were performed on nanolayered composites of multiple phases[32–35] as well as nanocrystalline[35–39] and nanotwinned materials[40,41]. Since the aim of this thesis is to understand the influence of single grain boundaries, the following section will focus on micromechanical experiments in that area.

2.4.1. Micromechanical experiments on bicrystalline samples

The first micromechanical experiments were conducted by Ng and Ngan[42] on bicrystalline Al compression pillars with $\sim 6\,\mu m$ diameter and a large angle grain boundary running from top to bottom of the pillar roughly parallel to the compression di-

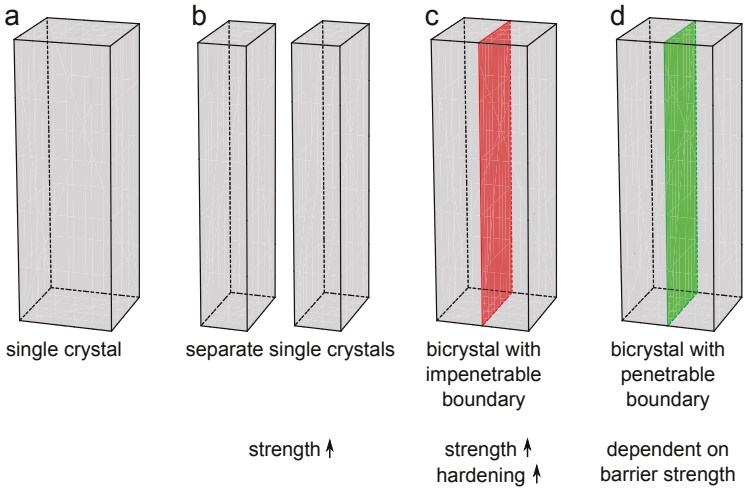

Figure 2.5.: Extreme cases of bicrystals and strengthening behavior.
due to the mechanical size effect pillars (b) and (c) will exhibit an increase in strength while the stress-strain behavior of (d) is dependent on the barrier strength of the boundary.

rection. The bicrystals showed higher strength, pronounced hardening and smaller strain bursts with a higher frequency compared to the single crystalline pillars. These effects are attributed to accumulation of dislocations at the boundary which lead to forest hardening, dipole interaction and junction formation—altogether impeding the movement of dislocations and reducing their mean free path.

Similar results were found for Au pillars in the size range of 440 nm–2.7 µm with an aspect ratio of 3:1 by Schamel[43]. While revealing similar yield strengths, differences were found concerning work hardening and intermittent plasticity. The bicrystals with a 17° tilt boundary with single slip oriented crystals exhibit stronger work hardening similar to multislip orientations and a drastic reduction in load drops, compared to single crystalline samples. Likewise, this is explained by increased dislocation-dislocation interactions and dislocation avalanches being blocked by the grain boundary.

A similar stress-strain response was also found in simulations. Fan et al.[44] simulated bicrystalline Al micropillars with 500 nm side length including a 10° tilt boundary by three-dimensional discrete dislocation dynamics (3D DDD). Depending on a threshold stress and energetic considerations dislocation penetration and dislocation emission was allowed. This lead to higher strength and less serrated flow of the bicrystals and was again explained by the impeded movement and accumulation of dislocations. Similar arguments were given earlier by Csikor et al.[45], stating that grain boundaries in polycrystals limit dislocation avalanches and lead to a smoother

deformation behavior.

Contrary to theses experiments are compression tests on Al bicrystals with 400 nm–2 µm in diameter by Kunz et al.[46]. Lower work hardening and larger strain bursts were reported for bicrystals compared to single crystals and explained by a low dislocation storage in the bicrystalline samples, leading to stronger stochastic behavior. These explanations are based on post-mortem TEM analyses that reveal a reduced dislocation density near the boundary, suggesting that the boundary acted as a dislocation sink.

Interestingly, Tucker et al.[47] found that the stochastic flow in molecular dynamics (MD) simulations of Al bicrystals can depend on the orientation of the single grains. Smoother as well as jerkier deformation compared to single crystalline pillars was found depending on the dislocation-dislocation interactions. Lots of interactions including the formation of defects lead to smoother behavior while dislocation escape to the surface caused dislocation starvation and strongly serrated flow. The samples in this study, however, were only 30 nm in diameter, facilitating dislocation starvation.

Kheradmand et al.[48–51] also found strengthening in bicrystalline Ni compression pillars oriented for single and multiple slip for each grain, respectively. Yet, only pillars smaller than 1–2 µm with increased dislocation-boundary interaction showed a strength increase, while larger pillars (3–5 µm) were claimed to be dominated by dislocation-dislocation interactions, similar to the multislip oriented single crystalline compression samples.

References for Chapter 2

[1] F. Frank. Orientation Mapping. *Metallurgical Transactions A*, 19:403–408, 1988.

[2] S.L. Altmann. *Rotations, Quaternions and Double Groups*. Clarendon Press, Oxford, 1986.

[3] D. Brandon. The structure of high-angle grain boundaries. *Acta Metallurgica*, 14(11):1479–1484, 1966.

[4] M. Kronberg and F. Wilson. Secondary recrystallization in copper. *AIME TRANS*, 185:501–514, 1949.

[5] G.C. Hasson and C. Goux. Interfacial energies of tilt boundaries in aluminium. Experimental and theoretical determination. *Scripta Metallurgica*, 5(10):889–894, 1971.

[6] E. Hall. The deformation and ageing of mild steel: III discussion of results. *Proceedings of the Physical Society. Section B*, 64(9):747, 1951.

[7] N. Petch. The cleavage strength of polycrystals. *J. Iron Steel Inst*, 174(1):25–28, 1953.

[8] H. Gleiter. Nanocrystalline materials. *Progress in Materials Science*, 33(4):223–315, 1989.

[9] M.A. Meyers, A. Mishra, and D.J. Benson. Mechanical properties of nanocrystalline materials. *Progress in Materials Science*, 51(4):427–556, 2006.

[10] L. Lu, Y. Shen, X. Chen, L. Qian, and K. Lu. Ultrahigh strength and high electrical conductivity in copper. *Science*, 304(5669):422, 2004.

[11] W.A.T. Clark, R.H. Wagoner, Z.Y. Shen, T.C. Lee, I.M. Robertson, and H.K. Birnbaum. On the criteria for slip transmission across interfaces in polycrystals. *Scripta Metallurgica et Materialia*, 26(2):203–206, 1992.

[12] Z. Shen, R.H. Wagoner, and W.A.T. Clark. Dislocation pile-up and grain boundary interactions in 304 stainless steel. *Scripta Metallurgica*, 20(6):921–926, 1986.

[13] J.D. Livingston and B. Chalmers. Multiple slip in bicrystal deformation. *Acta Metallurgica*, 5(6):322–327, 1957.

[14] T. Lee, I. Robertson, and H. Birnbaum. Anomalous slip in an FCC system. *Ultramicroscopy*, 29(1):212–216, 1989.

[15] S. Brenner. Tensile strength of whiskers. *Journal of Applied Physics*, 27(12):1484–1491, 1956.

[16] N.A. Fleck, G.M. Muller, M.F. Ashby, and J.W. Hutchinson. Strain gradient plasticity: Theory and experiment. *Acta Metallurgica et Materialia*, 42(2):475–487, 1994.

[17] M.F. Ashby. The deformation of plastically non-homogeneous materials. *Philosophical Magazine*, 21(170):399–424, 1970.

[18] W.D. Nix. Mechanical properties of thin films. *Metallurgical and Materials Transactions A*, 20(11):2217–2245, 1989.

[19] M.D. Uchic, D.M. Dimiduk, J.N. Florando, and W.D. Nix. Sample dimensions influence strength and crystal plasticity. *Science*, 305(5686):986, 2004.

[20] J.R. Greer, W.C. Oliver, and W.D. Nix. Size dependence of mechanical properties of gold at the micron scale in the absence of strain gradients. *Acta Materialia*, 53(6):1821–1830, 2005.

[21] D. Kiener, W. Grosinger, G. Dehm, and R. Pippan. A further step towards an understanding of size-dependent crystal plasticity: In situ tension experiments of miniaturized single-crystal copper samples. *Acta Materialia*, 56(3):580–592, 2008.

[22] C. Motz, T. Schöberl, and R. Pippan. Mechanical properties of micro-sized copper bending beams machined by the focused ion beam technique. *Acta Materialia*, 53(15):4269–4279, 2005.

[23] R. Dou and B. Derby. A universal scaling law for the strength of metal micropillars and nanowires. *Scripta Materialia*, 61(5):524–527, 2009.

[24] S.I. Rao, D.M. Dimiduk, T.A. Parthasarathy, M.D. Uchic, M. Tang, and C. Woodward. Athermal mechanisms of size-dependent crystal flow gleaned from three-dimensional discrete dislocation simulations. *Acta Materialia*, 56(13):3245–3259, 2008.

[25] D.J. Dunstan and A.J. Bushby. The scaling exponent in the size effect of small scale plastic deformation. *International Journal of Plasticity*, 40(0):152–162, 2013.

[26] B. von Blanckenhagen, P. Gumbsch, and E. Arzt. Dislocation sources and the flow stress of polycrystalline thin metal films. *Philosophical Magazine Letters*, 83(1), 2003.

[27] S.I. Rao, D.M. Dimiduk, M. Tang, T.A. Parthasarathy, M.D. Uchic, and C. Woodward. Estimating the strength of single-ended dislocation sources in micron-sized single crystals. *Philosophical Magazine*, 87(30):4777–4794, 2007.

[28] J.R. Greer and W.D. Nix. Nanoscale gold pillars strengthened through dislocation starvation. *Physical Review B*, 73(24):245410, 2006.

[29] T.A. Parthasarathy, S.I. Rao, D.M. Dimiduk, M.D. Uchic, and D.R. Trinkle. Contribution to size effect of yield strength from the stochastics of dislocation source lengths in finite samples. *Scripta Materialia*, 56(4):313–316, 2007.

[30] P. Sudharshan Phani, K.E. Johanns, E.P. George, and G.M. Pharr. A simple stochastic model for yielding in specimens with limited number of dislocations. *Acta Materialia*, 61(7):2489–2499, 2013.

[31] N.M. Jennett, R. Ghisleni, and J. Michler. Enhanced yield strength of materials: The thinness effect. *Applied physics letters*, 95(12):–, 2009.

[32] N. Mara, D. Bhattacharyya, P. Dickerson, R. Hoagland, and A. Misra. Deformability of ultrahigh strength 5 nm Cu/Nb nanolayered composites. *Applied physics letters*, 92:231901, 2008.

[33] D. Bhattacharyya, N.A. Mara, P. Dickerson, R.G. Hoagland, and A. Misra. Compressive flow behavior of Al-TiN multilayers at nanometer scale layer thickness. *Acta Materialia*, 59(10):3804–3816, 2011.

[34] J.Y. Zhang, G. Liu, and J. Sun. Comparisons between homogeneous boundaries and heterophase interfaces in plastic deformation: Nanostructured Cu micropil-

lars vs. nanolayered Cu-based micropillars. *Acta Materialia*, 61(18):6868–6881, 2013.

[35] J.Y. Zhang, S. Lei, Y. Liu, J.J. Niu, Y. Chen, G. Liu, X. Zhang, and J. Sun. Length scale-dependent deformation behavior of nanolayered Cu/Zr micropillars. *Acta Materialia*, 60(4):1610–1622, 2012.

[36] A. Rinaldi, P. Peralta, C. Friesen, and K. Sieradzki. Sample-size effects in the yield behavior of nanocrystalline nickel. *Acta Materialia*, 56(3):511–517, 2008.

[37] D. Jang and J.R. Greer. Size-induced weakening and grain boundary-assisted deformation in 60 nm grained Ni nanopillars. *Scripta Materialia*, 64(1):77–80, 2011.

[38] X.W. Gu, C.N. Loynachan, Z. Wu, Y.-W. Zhang, D.J. Srolovitz, and J.R. Greer. Size-Dependent Deformation of Nanocrystalline Pt Nanopillars. *Nano letters*, 12(12):6385–6392, 2012.

[39] J.Y. Zhang, G. Liu, and J. Sun. Strain rate effects on the mechanical response in multi- and single-crystalline Cu micropillars: Grain boundary effects. *International Journal of Plasticity*, 50(0):1–17, 2013.

[40] D. Jang, C. Cai, and J.R. Greer. Influence of Homogeneous Interfaces on the Strength of 500 nm Diameter Cu Nanopillars. *Nano letters*, 2011.

[41] D. Jang, X. Li, H. Gao, and J.R. Greer. Deformation mechanisms in nanotwinned metal nanopillars. *Nature Nanotechnology*, 2012.

[42] K.S. Ng and A.H.W. Ngan. Deformation of micron-sized aluminium bi-crystal pillars. *Philosophical Magazine*, 89(33):3013–3026, 2009.

[43] M. Schamel. *The influence of interfaces on small-scale mechanical behavior: From fcc metals to polymer/ceramic composites*. PhD thesis, ETH Zurich, 2014.

[44] H. Fan, Z. Li, and M. Huang. Toward a further understanding of intermittent plastic responses in the compressed single/bicrystalline micropillars. *Scripta Materialia*, 66(10):813–816, 2012.

[45] F.F. Csikor, C. Motz, D. Weygand, M. Zaiser, and S. Zapperi. Dislocation avalanches, strain bursts, and the problem of plastic forming at the micrometer scale. *Science*, 318(5848):251–254, 2007.

[46] A. Kunz, S. Pathak, and J.R. Greer. Size effects in Al nanopillars: Single crystalline vs. bicrystalline. *Acta Materialia*, 59(11):4416–4424, 2011.

[47] G.J. Tucker, Z.H. Aitken, J.R. Greer, and C.R. Weinberger. The mechanical behavior and deformation of bicrystalline nanowires. *Modelling and Simulation in Materials Science and Engineering*, 21(1):015004, 2013.

[48] N. Kheradmand, A. Barnoush, and H. Vehoff. Investigation of the role of grain boundary on the mechanical properties of metals. *Journal of Physics: Conference Series*, IOP Publishing, 240(1), 2010.

[49] N. Kheradmand and H. Vehoff. Orientation Gradients at Boundaries in Micron-Sized Bicrystals. *Advanced Engineering Materials*, 14(3):153–161, 2012.

[50] N. Kheradmand, J. Dake, A. Barnoush, and H. Vehoff. Novel methods for micromechanical examination of hydrogen and grain boundary effects on dislocations. *Philosophical Magazine*, 92(25-27):3216–3230, 2012.

[51] N. Kheradmand, H. Vehoff, and A. Barnoush. An insight into the role of the grain boundary in plastic deformation by means of a bicrystalline pillar compression test and atomistic simulation. *Acta Materialia*, 61(19):7454–7465, 2013.

3

Differences in deformation behavior of bicrystalline Cu micropillars containing a twin- or a large angle grain boundary

Peter J. Imrich[a], Christoph Kirchlechner[b,c], Christian Motz[a,d], Gerhard Dehm[b,c]

[a]Erich Schmid Institute of Materials Science, Austrian Academy of Sciences, Leoben, Austria
[b]Department of Materials Physics, Montanuniversität Leoben, Austria
[c]Max-Planck-Institut für Eisenforschung, Düsseldorf, Germany
[d]Department of Materials Science, Saarland University, Saarbrücken, Germany

3. Differences in deformation behavior of bicrystalline Cu micropillars containing a twin- or a large angle grain boundary

Abstract

Micrometer-sized compression pillars containing a grain boundary are investigated to better understand under which conditions grain boundaries have a strengthening effect. The compression experiments were performed on focused ion beam (FIB) fabricated micrometer-sized bicrystalline Cu pillars including either a large angle grain boundary (LAGB) or a coherent twin boundary (CTB) parallel to the compression axis and additionally on single crystalline reference samples. Pillars containing a LAGB show increased strength, stronger hardening and smaller load drops compared to single crystals and exhibit a bent boundary and pillar shape. Samples with CTB show no major difference in stress-strain data compared to the corresponding single crystalline samples. This is due to the special orientation and symmetry of the twin boundary and is reflected in a characteristic pillar shape after deformation. The experimental findings can be related to the dislocation-boundary interactions at the different grain boundaries and are compared with three dimensional discrete dislocation dynamics (3D DDD) simulations.

3.1. Introduction

The mechanical behavior of samples in small dimensions is different from that of bulk materials. The most striking feature is a drastic increase in strength with decreasing specimen size. This decrease in specimen size can either be one-dimensional as for thin films[1–3], two-dimensional as for thin wires[4] or three-dimensional as for small compression[5], bending[6] or tensile samples[7]. In 2004 a technique was developed by Uchic et al.[5] to create and mechanically test compression pillars that are small in all three dimensions, using a focused ion beam system (FIB). These single crystalline micron- and submicron sized compression pillars show increasing yield strength with decreasing sample size. This so called mechanical size effect was confirmed by numerous microcompression, tension and bending experiments on samples from approximately 100 nm–20 µm in diameter[5–13] and is now well established and fairly well understood. The reason for the "smaller is stronger" effect is based on the dislocation density and number of available dislocation sources as has been shown by e. g. Bei et al.[14]. Depending on the sample size, different processes including source statistics[15,16], dislocation starvation[17], source truncation[16] and dislocation exhaustion[18] have been proposed to describe the size effect and the stochastic flow behavior of microsamples. The critical stress to activate a dislocation source, that can be either of Frank-Read or single arm type, scales inversely with the source size.

A decrease in sample dimensions leads to a reduction in source size which in turn increases the flow stress.

Efforts to quantify the size effect have mostly come up with a power law description of the yield strength, σ_y:

$$\sigma_y = \sigma_0 + kd^{-n} \tag{3.1}$$

linking the yield strength to the diameter d of the sample with a scaling exponent n, similar to a Hall-Petch type law, although the underlying mechanisms are completely different. σ_0 corresponds to the bulk strength of the material and k is a constant in Eq. 3.1. Numbers for the scaling exponent range from 0.2 or even 0 in ceramics[19] up to 0.6–1 in fcc metals[20]. However, defining an exact value for the scaling exponent has aroused controversy, since it was shown to depend on many factors, including dislocation- and pinning point density[21]. Dunstan et al.[22] even go as far as claiming a constant exponent of 1 for all materials arguing that deviations are due to special circumstances or ambiguous fitting of logarithmized data.

Looking at real world materials, we know that the majority of commercially used metals are polycrystalline, i. e. comprised of numerous grains with grain sizes reaching from a few centimeters down to several nanometers. It was discovered by Hall[23] and Petch[24] that the yield strength of metals scales inversely with the square root of the average grain size. This effect shows the importance of grain boundaries concerning deformation behavior and is of major importance for the strengthening of materials by grain refinement. The discovery led to many scientific studies trying to understand the ongoing mechanisms and create novel materials with advanced mechanical properties by altering the grain size[25–27].

Recently, micromechanical testing was applied to specimens containing two or more grains[28–48] in order to gain information on the influence of extrinsic and intrinsic feature size on the stress-strain behavior as well as on the underlying deformation mechanisms. In a polycrystalline macrosample the behavior of individual grain boundaries is not clearly identifiable due to simultaneous plasticity in many grains. By studying bicrystalline micropillars, specific gain boundary types can be tested in uniaxial compression, which avoids the complication of an unknown stress state in polycrystalline samples. Thus, pillar micro-compression offers the possibility to apply different stress states onto dislocations transmitting the boundary. Up to now, there have been experiments on multiphase nanolayered composites[28–31], nanocrystalline[31–34,36] and nanotwinned materials[35,37]. The studies most relevant to this work, however, are on fcc compression samples that include one single grain boundary. Ng and Ngan[38] first conducted experiments on bicrystalline Al pillars with approximately 6 µm diameter

and a large angle grain boundary running through the pillar along the compression direction. They found that the bicrystals show higher strength, stronger hardening and smaller strain bursts with a higher frequency. The less jerky deformation and the hardening behavior are attributed to the high density of stored dislocations that accumulate due to the boundary and lead to more frequent dislocation-dislocation interactions. Forest hardening, dipole interaction, junction formation and dislocation pile-up impede easy propagation of dislocations which leads to less serrated materials flow. A similar stress-strain response is found by Fan et al.[39] using 3D DDD to simulate Al micropillars with 500 nm side length. The simulations include a 10° tilt boundary that allows dislocation penetration and dislocation emission depending on a threshold stress and energetic considerations. Again, higher strength and less serrated flow is found for the bicrystals and explained with the impeded movement and accumulation of dislocations.

Experiments by Kunz et al.[40] on smaller Al bicrystals with 400 nm to 2 µm in diameter stand in stark contrast to these results. They report lower hardening and larger strain bursts which is explained by low dislocation storage in the pillars leading to a larger stochasticity of deformation. TEM analyses reveal a low dislocation density near the boundary indicating that the boundary might act as a dislocation sink. Another explanation given is a sudden localized breakdown of the boundary that triggers large bursts. An interesting molecular dynamics (MD) study by Tucker et al.[41] shows, that the deformation behavior of 30 nm sized bicrystalline nanowires can be either smoother or jerkier compared to single crystalline samples. This is said to be determined by the dislocation-dislocation interactions inside the material. A smooth behavior was found when dislocations intersect each other and form defects, lowering the mean free path, while jerky deformation was predominant when the dislocations easily escaped the crystal leading to dislocation starvation. Kheradmand et al.[43–46] claims that there is a change in the hardening mechanism when decreasing the pillar size. While larger Ni pillars (3–5 µm) are dominated by hardening due to dislocation-dislocation interactions and the flow curve is controlled mainly by the strongest component crystal, the influence of dislocation-boundary interactions increases in smaller pillars ($\leq$ 1–2 µm) and leads to strengthening compared to the single crystals.

From the current understanding an impenetrable boundary leads to an increase of dislocation density through dislocation accumulation while a boundary acting as a sink will lower the dislocation density. Depending on the sample size and dislocation density this has different effects on the mechanical behavior: (i) small samples tend to harden through dislocation starvation so an increase in dislocation density leads

to easier dislocation multiplication, thus easier deformation, (ii) large samples tend to harden through dislocation-dislocation interactions so an increase in dislocation density leads to more restrained dislocation motion, thus hardening. At this point it is hard to say how big the influence of the continuity constraints at the boundary and the activation of different slip systems on the deformation behavior are. The fact that grain boundaries can also act as sources should not be omitted, but it is clear that multiple factors have to be considered to describe the full impact of grain boundaries on the deformation behavior.

In the present study the authors try do advance the understanding of bicrystalline samples by investigating the deformation behavior of Cu microcompression pillars containing a large angle grain boundary (LAGB) or a coherent twin boundary (CTB). For comparison, single crystalline pillars of the same size were tested for all four crystal orientations forming the bicrystals. The sample shape as well as the stress-strain behavior will be discussed and related to disloca tion interactions and finally compared to 3D DDD simulations of samples with an impenetrable and a semipermeable boundary.

3.2. Experimental details and simulation setup

In the following part the sample preparation route, sample dimensions and testing procedure as well as the setup for the DDD simulations will be described. All samples were prepared with a LEO 1540 XB dual beam FIB workstation operating with Ga^+ ions at an accelerating voltage of 30 kV. The currents used range from 5 nA down to 100 pA for coarse to fine milling, respectively. At least two pillars were tested for each pillar type, i. e. for each single crystal orientation and each boundary type but only one representative set of pillars is shown for clarity. The exact micropillar preparation route differed due to the different geometries and availability of the bulk material and is described in detail below.

3.2.1. Large angle grain boundary (LAGB)

For the micro-compression tests on the LAGB thin slices were cut off from a bulk bicrystalline copper sample with an arbitrary large angle grain boundary. These slices were then electro-chemically etched to produce a wedge with a sharp edge for faster manipulation by the ion beam to form micropillars, following the approach of Moser et al.[49]. On each of the wedges that were prepared with this method, two pillars from each grain and one incorporating the LAGB were cut with a nominal

size of $7 \times 7 \times 21\,\mu m^3$ leading to an aspect ratio of 1:3. All pillars were milled with the ion beam perpendicular to the compression axis to ensure parallel sidewalls, i. e. the cross-section is constant throughout the whole pillar length. This avoids strain gradients that are caused by a tapered sample geometry. For achieving a top surface that is perpendicular to the compression axis the sample was overtilted by 1–2°. The grain boundary intersects the diagonal of the rectangular pillar and lies parallel to the compression axis. µLaue measurements show a difference in grain orientation of 22.8° around $[1\bar{3}4]$ and compression directions close to $[40\bar{1}]$ and [310] for grain 1 and grain 2, respectively. A rough estimation of the grain boundary plane using SEM images and µLaue data leads to $(3\,\bar{1}\,12)$ in respect to grain 1.

Figure 3.1.: SEM micrographs of micropillars after compression. (a) Compression sample of grain 1. (b) Bicrystalline pillar containing a LAGB that is composed of grain 1 and grain 2. (c) Compression sample of grain 2.

The pillars were loaded in 2–4 steps with a strain rate of $\sim 10^{-3}\,s^{-1}$ to a total plastic strain of 8–18 % using the displacement controlled straining device described in Ref. [50]. Force displacement data was recorded during compression and high resolution scanning electron microscopy (SEM) images were taken before and after deformation.

3.2.2. Coherent twin boundary (CTB)

The sample that was used for testing the mechanical properties of a twin boundary was grown from OFHC copper of 99.999 % purity by the Bridgman method and contained a CTB along the growth direction. A small rod with square cross-section was cut off, electropolished, glued to a sample holder and then processed with the FIB to form micropillars with a nominal size of $4.3 \times 4.3 \times 13\,\mu m^3$ resulting in an aspect ratio of 1:3. All pillars were shaped near the sample edge to be able to observe the deformation process in situ in the SEM. The side surfaces were cut perpendicular to the compression axis and the front and back surfaces parallel to the compression axis. To ensure a constant cross-section and avoid tapering of the sample throughout the entire gauge length, the front and back surfaces were cut with an overtilt of 1–2°. This method led to a pillar with a constant, but slightly trapezoidal cross-section (2° of FIB-taper on the sidewalls from front to back) for this type of sample. One compression sample in each grain and one sample incorporating the CTB was produced. The bicrystalline sample contains a CTB that runs through the middle of the pillar parallel to its sidewalls straight from top to bottom and extends through the whole bulk sample. Both crystals are oriented such that the compression axis is close to a $\langle 0\bar{1}1 \rangle$ direction. After mechanical testing the same strip of material was ground and electropolished and another set of pillars was made.

Mechanical testing was carried out in situ in a LEO 982 SEM using an ASMEC UNAT microindenter. The displacement controlled compression experiments were performed in two consecutive steps to a plastic strain of 15–19 % with a displacement rate of $10\,nm\,s^{-1}$ leading to a strain rate of $\sim 8 \times 10^{-4}\,s^{-1}$. During the experiment force displacement data as well as secondary electron images of the deforming pillar were collected (for a time-lapse of the compression experiment see supplementary movie 3.1).

3.2.3. Setup of the 3D discrete dislocation dynamics simulation

To assist the interpretation of the bicrystalline micro-compression experiments 3D DDD simulations were performed. Only a short overview on the simulation method will be given here, for further details the reader is referred to[51–54].

The boundary value problem is solved according to the superposition principle of Ref.[51], where a finite element (FE) framework is utilized to apply the boundary conditions, image forces, etc. From the superimposed stress fields of the FE framework and the dislocation structure the Peach-Koehler force acting on each dislocation segment is calculated and the equation of motion is solved using standard time inte-

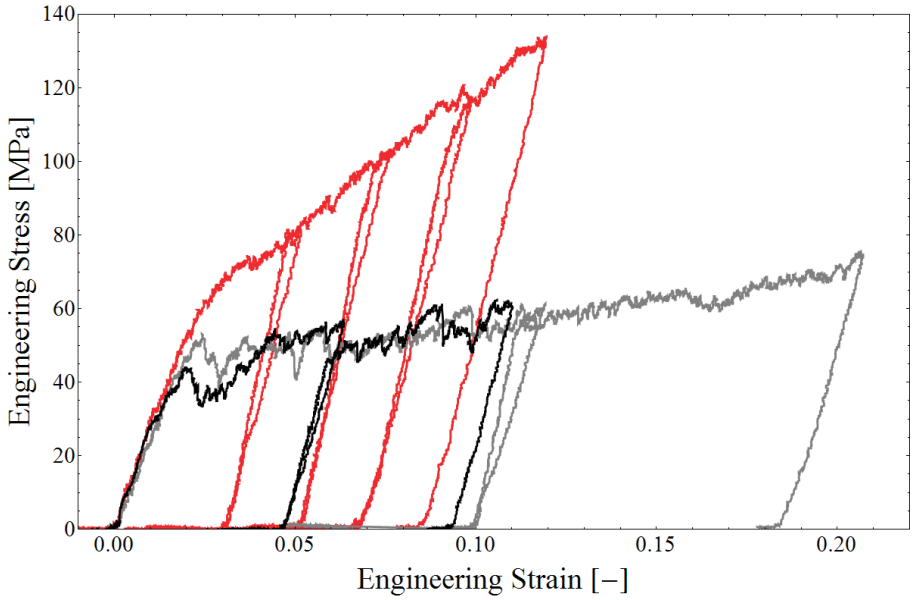

Figure 3.2.: Engineering stress–strain curve of the single-crystalline Cu pillars of grain 1 (gray), grain 2 (black) and the bicrystalline pillar containing a LAGB (red). While the single crystals show similar behavior, the bicrystal exhibits increased yield strength and shows stronger hardening.

gration schemes. Subsequently, the dislocation structure is updated and a new time step is calculated.

The specimen size was chosen with $w \times t \times l = 0.5 \times 0.5 \times 1.5\,\mu m^3$ and $1.0 \times 1.0 \times 3.0\,\mu m^3$ to keep computational time low. The material properties of aluminum were used as standard material, namely shear modulus $G = 27\,GPa$, Poisson's ratio $\nu = 0.347$ and lattice constant $a = 404\,pm$. The authors know that there is a difference in cross-slip probability between Al and Cu. However, the full anisotropic behavior of Cu cannot yet be simulated by DDD and only the principle response is of interest here which can be well captured with the used material parameters. For the simulations displacement controlled boundary conditions are utilized, where the top surface is moved downwards in the [001] direction (compression) and the bottom surface is fixed in that direction. The strain rate was chosen in the region of $10^{-3}\,s^{-1}$, so that strain rate effects due to inertia are avoided. As an initial dislocation structure randomly distributed Frank-Read sources with a size of $L = 500\,a$ were used. This value was chosen since it correlates with the mean dislocation distance of 224 nm for the chosen dislocation density of $2 \times 10^{13}\,m^{-2}$ and well describes the experimental observations. A single crystal with [001] orientation aligned with the compression axis was simulated. At the center plane at $w = 0.5\,\mu m$ (similar to the experiments) three

different types of boundaries were introduced: (i) no boundary, all dislocations can freely move within the crystal, (ii) an impenetrable boundary where all dislocations are blocked and (iii) a semipermeable boundary where only dislocations on a specific glide system (glide plane normal $n_3 = (\bar{1}\bar{1}1)$, Burgers vector $b_2 = [011]$) can pass.

The choice of orientation was deliberately chosen to deviate from the experimental orientation. To approximate the CTB boundary to the best possibility (the introduction of a $\Sigma 3$ boundary is not supported by the DDD code) a $\Sigma 1$ boundary was introduced where only dislocations of one glide system can be transmitted. To assure that cross-slip is the dominant deformation mechanism at the boundary, no dislocation source was placed on the permeable system. To keep the Schmid factor high and constant before and after the cross-slip event, as is the case in the CTB bicrystal, an orientation with symmetric slip systems had to be chosen. Since a [110] compression direction would lead to cross-slip into a slip-system parallel to the compression direction with a Schmid factor of zero, [100] was used as compression direction. This orientation was also used for the single crystal and $\Sigma 1$ crystal with impenetrable boundary to allow best comparability between the simulation results. The DDD results will be presented in section 3.4.4 to interpret and discuss the experimental results.

3.3. Micro-compression results

In this section the SEM micrographs of the micropillars and the corresponding stress-strain curves are presented, only one representative set of LAGB and CTB samples is depicted for clarity.

3.3.1. LAGB

The single- and bicrystalline pillars after compression are shown in Fig. 3.1. All single crystals have very distinct slip steps as is characteristic for this material and pillar size[55]. On every single crystalline pillar two $\{111\}\,[\bar{1}10]$ glide systems can be identified that account for the deformation. The bicrystal on the other hand has many small but few large slip steps. These steps extend solely through one grain and stop at the grain boundary. The only larger surface steps that are visible near the sample edges fade away when getting closer to the boundary (Fig. 3.1 b). On both side surfaces of the pillar a small step of varying height was formed where the boundary intersects the free surface.

The stress-strain curve depicted in Fig. 3.2 confirms the expected behavior. While

Figure 3.3.: SEM micrographs of micropillars after compression; the CTB is nearly parallel to the viewing direction going from top to bottom of the pillar. (a) Compression sample of grain 1. (b) Bicrystalline pillar containing a CTB that is comprised of grain 1 and grain 2. It can be clearly seen that the slip steps of both grains meet perfectly along a straight line, the CTB. (c) Compression sample of grain 2.

the single crystals show the typical serrated flow with very little hardening, the bicrystal exhibits a higher yield strength, much stronger hardening and less pronounced load drops. The yield strengths of the pillars are 52 MPa, 44 MPa and 62 MPa for grain 1, grain 2 and the bicrystal, respectively. This leads to a 19 % and 41 % strength increase for the bicrystal compared to grain 1 and grain 2, respectively. All yield strengths are measured at 1 % strain or at the peak yield stress for smooth or abrupt elastic-plastic transitions, respectively. It has to be noted, that the slope of the unloading curves deviates from the expected behavior. This is due to a faster unloading speed of the strongly damped indenter but does not affect the loading part of the experiment and the stress measurement.

The bicrystalline pillar containing a CTB is shown in Fig. 3.3 together with two single crystalline compression samples after deformation. As for other multiple slip oriented single crystalline pillars these deform in a characteristic manner. The distinct glide steps that were formed at the surface can be clearly distinguished. The bicrystalline pillar shows similar behavior when separately looking at each compo-

nent crystal, i. e. the two $\{\bar{1}\bar{1}1\}$ $[\bar{1}10]$ glide systems activated for each twin orientation match those of the corresponding single crystal. Contrary to the LAGB bicrystal each of the two slip systems of grain 1 is connected at the twin boundary with the corresponding slip systems in grain 2, as can be clearly seen in Fig. 3.3 b. The planes of the individual systems always meet perfectly at the CTB and all slip steps extend through both grains, which leaves the boundary unbent and produces large slip steps which can easily be identified in the side view in Fig. 3.4. The deformation of the pillar occurs through collective slip of both grains into the same direction along a set of two $\{\bar{1}\bar{1}1\}$ planes that enclose an angle of 141°.

While one could think that the introduction of the CTB would lead to a strengthening of the compression sample like for the LAGB, Fig. 3.5 proves the opposite. The stress-strain curves show similar elastic slopes, yield points and hardening behavior for both kinds of pillars. Both single crystals show a smooth elastic-plastic transition at yield stresses of 120 MPa and 135 MPa while the bicrystal exhibits a peak yield stress of 131 MPa and shows slight softening before the stress increases and reaches a plateau at approximately 145 MPa.

3.4. Discussion

The opposing results of the LAGB and the CTB is the central aspect of the following discussion which is complemented by 3D DDD simulations. The results of the single crystalline Cu samples that were tested in the scope of this paper are comparable regarding deformation morphology, stress-strain behavior, reproducibility and results documented in literature[4–13,55–59] and thus are not further discussed.

3.4.1. LAGB

Two very distinctive differences are visible by analyzing the LAGB pillar by SEM compared to the adjacent single crystalline pillars. The glide steps at the surface are much weaker and more glide steps are observed, indicating less localized plasticity. Additionally, the different flow behavior of the individual grains leads to a large distortion of the pillar, with a deflection of the grain boundary in the center of the sample of approximately 17° compared to the pristine orientation. This distortion is most likely caused by the different mechanical properties of the two crystal orientations in the LAGB pillar combined with the constraints imposed by the testing setup. The Young's moduli in compression direction are fairly similar with 75 GPa and 79 GPa for grain 1 and grain 2, respectively, as calculated from the elastic constants[60]. Elas-

Figure 3.4.: Side view of the deformed bicrystalline pillar from Fig. 3.3 b. The CTB runs from left to right through the top surface of the pillar and is nearly parallel to the viewing plane. Both grains are displaced simultaneously into the same directions parallel to the image plane.

tic buckling can be excluded due to the aspect ratio of length to thickness of ~ 3; however, elastoplastic buckling as discussed in[61] could cause the observed bending.

The stress-strain curve (Fig. 3.2) of the LAGB pillar is dominated by a higher yield strength, stronger hardening and smaller load drops compared to the corresponding single crystalline pillars. The most apparent reason for the strength increase of 19 % to 41 % at 1 % strain is the reduction in source size in the component grains through truncation hardening. It should be noted that the evaluation of yield strength in micromechanical samples is influenced by the strain at which it is analyzed. Since an evaluation at 0.2 % strain as for macroscopic samples is not sensible due to the lack of accuracy in micromechanical tests, we performed our measurements at 1 %

strain. As discussed in the introduction, the use of a constant size effect exponent for the strengthening power law is controversial, however, to get an estimate for the increase in yield strength, the phenomenological scaling law by Dou and Derby[20] and the source activation stress formula by Rao et al.[18] were used. Rao et al. calculated the critical resolved shear stress of double-ended and single-ended dislocation sources of 30° mixed type with varying lengths from 233–933 Burgers vectors and fit the simulation data with the following equation:

$$\tau(L) = kG\frac{\ln(L/b)}{L/b} \tag{3.2}$$

Here L is the source length, G the shear modulus, b the Burgers vector and k a constant with values of 0.06 to 0.18 for single-ended to double-ended sources. Since the bicrystal is slightly smaller in size compared to the single crystalline samples, it must first be calculated how much this size difference contributes to the strengthening of the pillar. This only amounts to 9 % to 13 % using the concepts of Dou and Derby or Rao et al., respectively. Assuming that the size of the dislocation sources is limited by the free surfaces and the grain boundary, the smallest distance to the surface or boundary defines the strength of the dislocation source for continuous operation. The largest possible source size is the radius of the largest circle that can be inscribed into the triangular base area of each grain. Using this length, a strength increase of 55 % or 81 % can be calculated for Dou and Derby or Rao, respectively. Both calculations overestimate the experimental values, so one could question whether source truncation is the sole mechanism that defines strengthening of the bicrystal similar to observations by Ng and Ngan[38]. However, the largest suitable single ended sources have an activation shear stress of only 4 to 7 MPa, calculated by the Rao model. Thus it is easily reasoned that the expected sources in the micropillar are much smaller (155–535 nm when using the shear stresses from the experiment). This could be the cause for the less pronounced source truncation effect for these large samples.

3.4.2. CTB

The numerous small slip steps at the sample surface, the stronger hardening and the less serrated flow can be explained by exhaustion hardening as defined by Rao et al.[21] that is enhanced due to the grain boundary. Ng and Ngan[38] and Fan et al.[39] state that a LAGB can act as a barrier to dislocations, leading to a dislocation pile-up and increase in dislocation density. These accumulated dislocations act as forest

Figure 3.5.: Engineering stress–strain curve of the single-crystalline compression samples of grain 1 (gray), grain 2 (black) and the bicrystalline sample containing a CTB (green).

dislocations and lower the mean free path for dislocation-slip. Therefore sources will exhaust faster due to dislocation-dislocation and dislocation-boundary interactions and the developing backstresses. Further deformation needs higher stresses to reactivate these sources or activate other less favorable ones[21], explaining the strong hardening and the numerous slip steps. The continuous increase in dislocation density results in steady hardening. Since the measurement of strain hardening rate is prone to the instrumental boundary conditions, like for instance the lateral compliance of the indenter system[62], no quantitative values will be given here. However, the curves clearly show that the strain hardening in the bicrystal is considerably higher compared to the single crystals. Note that the same indenter and the same macro-sample were used, ensuring the same unknown lateral compliance.

Regarding the serration amplitude we will consider a single dislocation with a Schmid factor of 0.5 that traverses a pillar from one side to the other. The generated displacement of 1.8 Å in compression direction leads to a load drop of 0.65 MPa in a 21 µm long sample, when using a Young's modulus of 75 GPa. When a new dislocation source gets activated and produces a dislocation burst in a single crystal, where dislocations can easily escape to the surface, a pronounced load drop will be the consequence. In the bicrystal the lower mean free path leads to smaller but more frequent dislocation steps, resulting in a smaller serration amplitude.

These observations agree well with the results from Ng and Ngan[38]. Interestingly, their TEM investigations show no evidence of pile-up at the grain boundary but a high density of stored dislocations in the whole pillar. This can be caused by a spreading of dislocations onto different parallel slip planes by double cross-slip when approaching a developing pile-up, a reorganization of the dislocation structure after the removal of the compressive load as expressed by the authors or the dissolution of the pile-up to the surface during TEM lamella preparation[63]. Contrary to their experiments no barreling and no pronounced sliding of the boundary is observed in our study. There is a step less than 100 nm in size where the grain boundary intersects the surface, however, it is much smaller than the $\sim 1\,\mu m$ wide step seen by Ng and Ngan[38]. Further agreement can be found with the simulations of Fan et al.[39] even though their simulated samples allow dislocation transmission through the boundary at a threshold stress.

Other experimental results, however, are very contrary to the findings presented here. It seems as though the properties of the grain boundary are significantly different to the LAGB that we tested. Bicrystalline Al compression pillars in the range of 400 nm to 2 µm by Kunz et al.[40] exhibit higher strain bursts and lower hardening rates, completely opposing the findings presented above. As mentioned in the introduction, this behavior is said to be due to the absorption of dislocations at the boundary that is claimed to act as a sink for dislocations, based on post-mortem TEM studies revealing no dislocation pile-ups at the boundary. If the boundary truly acts as a dislocation sink, it could enhance the dislocation starvation process, explaining the large strain bursts. The lower hardening rate, however, would need a stress independent dislocation generation mechanism for this theory to be coherent, e. g. the grain boundary acting as a source of dislocations as well. Kheradmand et al.[43–46] claim that there is a change in hardening mechanism when decreasing the pillar size. If this boundary was also acting as a dislocation sink, the increased influence of the boundary in smaller samples would make sense due to enhanced dislocation starvation. For larger samples that harden due to dislocation-dislocation interactions the hardening and softening mechanisms would have to cancel each other out, leading to a similar behavior to single crystals. The discrepancy in strain bursts and hardening behavior found in MD simulations by Tucker et al.[41] matches this argumentation, showing more continuous flow for low mean free paths with enhanced dislocation-dislocation interactions and larger serrations for unimpeded dislocation movement leading to starvation.

3.4.3. CTB

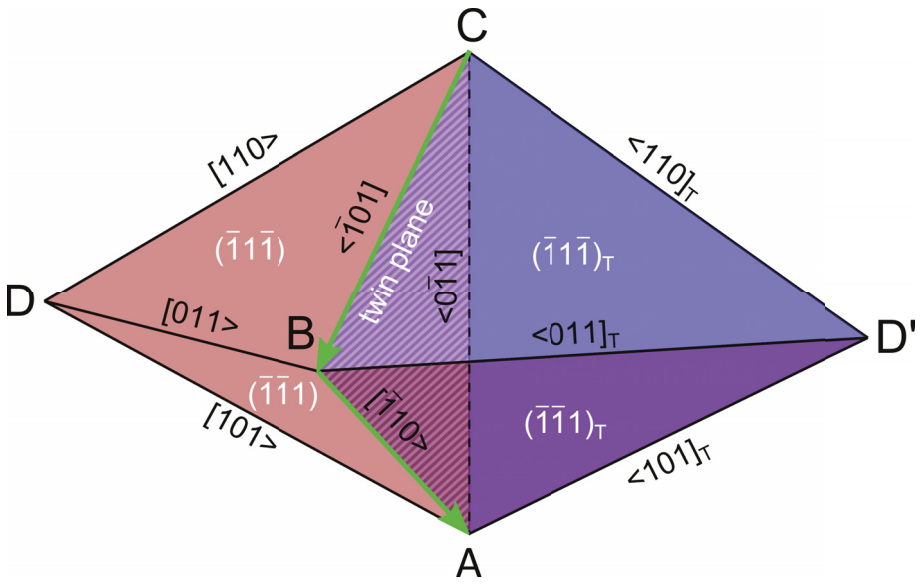

Figure 3.6.: Thompson tetrahedron *ABCD* that is mirrored across the (111) plane (*ABC*) creating the geometry of a twin boundary. The $\langle\bar{1}10\rangle$ Burgers vectors *BA*, *CB* and *CA* are shared by both grains. Green arrows depict the acting Burgers vectors. The compression direction (close to $[0\bar{1}1]$ in the experiments) is from top to bottom of the image along the dotted line. In this setup the screw dislocation *CB* can cross-slip from the glide plane *BCD* in the red grain into *BCD'* in the blue grain.

Contrary to the sample containing a LAGB the CTB pillar behaves similar to the single crystalline samples, i. e. having similar yield strength and hardening behavior. It deforms in a very interesting way showing glide on conjugated slip systems. Since the direction of deformation at the slip steps is identical for both grains, it is easy to argue that the Burgers vector in both slip systems must be the same. To understand the geometry of the CTB pillar it is best to imagine a Thompson tetrahedron that is mirrored across the (111) plane (Fig. 3.6). This common mirror plane represents the twin boundary, leaving three other $\{\bar{1}\bar{1}1\}$ planes on each tetrahedron. As for every fcc metal there are 12 possible slip systems in each grain (four slip planes with three Burgers vectors each). Only three Burgers vectors are shared by both grains, i. e. lie on the common (111) mirror plane. Since the CTB plane in this experiment is parallel to the compression direction there is no shear stress acting on it. However, dislocations with one of the three shared Burgers vectors can glide on one slip plane in each grain. These dislocations will always have the highest Schmid factor when the twin boundary is parallel to the compression direction as shown by Li et al.[48].

The two Burgers vectors with Schmid factor $m \neq 0$ in this experiment that can lead to collective sliding of both sides are depicted as arrows in Fig. 3.6. An activation of such combined systems leads to the observed geometry of the deformed pillars.

Different explanations can be given to explain the lack of source truncation strengthening due to the separate grains. Analog to the LAGB the size of sources can be calculated from the resolved shear stresses by the Rao method[18]. The calculated size of the single arm sources ranges from 79–180 nm for the CTB bicrystal, thus being significantly smaller than half the pillar size. As for the LAGB this could lead to a diminished influence of the source truncation process. Irrespective of that, there are some scenarios that can explain the unchanged strength (Please note that the source morphologies in Fig. 3.8 should be seen as simplified illustrations to support the basic understanding):

1. The CTB does not pose a barrier at all for the dislocations and they can easily transfer from one grain to the other while experiencing a bend at the boundary (Fig. 3.8 a)

2. A single arm dislocation source that has a pinning point in the grain boundary operates (Fig. 3.8 b)

3. A dislocation source that has one pinning point in each grain and spans over the twin boundary operates (Fig. 3.8 c)

4. A source (single arm or Frank-Read type) in one grain is activated and produces dislocations that approach the boundary and cross-slip into the second grain after piling up at the boundary (Fig. 3.8 d)

The points above are discussed in detail below. In all cases it is assumed that the dislocations have a Burgers vector parallel to the twin plane, as depicted in Fig. 3.6. In case 1 the sources can operate like in a single crystal since the dislocations are not blocked by the twin boundary and immediately transfer to the other grain, when meeting the boundary. Case 2 illustrates a special case of example 1 where the pinning point is exactly at the grain boundary, e. g. formed during the growth process. The source operates and two cross-slip events are needed for each full rotation. Another possibility (case 3) is a dislocation created during the growth process that spans from one grain to the other and is then pinned on both sides (Fig. 3.8 c). With easy cross-slip, the sources would split up into two single arm sources and operate similar to case 1 while reconnecting, when the dislocation segments meet again in between the pinning points. With hard cross-slip an additional revolution of one side would

lead to a screw dislocation laid down at the boundary that would annihilate upon operation of the second source.

Figure 3.7.: DDD simulations of (a) $0.5 \times 0.5 \times 1.5\,\mu m^3$ and (b) $1 \times 1 \times 3\,\mu m^3$ compression pillars. Bold lines: engineering stress; thin lines: dislocation density; black: single crystals; red: bicrystals with impenetrable boundary; green: bicrystals with a semipermeable boundary (only dislocations of one slip system can transfer to the other grain).

If cross-slip is not easily achieved, but sufficient stress is needed to transfer dislocations through the boundary, case 1 would transform to case 4 (Fig. 3.8 d). While in situ TEM experiments on twinned Cu films by Dehm et al.[64] show a single dislocation crossing a twin boundary at shear stresses in the order of 25 MPa calculated by fitting the dislocation radius, other publications show the need of much higher stresses. MD simulations by Jin et al.[65] demonstrate that global shear stresses of 465–510 MPa are

needed for a screw dislocation to cross the twin boundary. Chassagne et al.[66] calculate a critical reaction stress of close to 400 MPa for transmitting a screw dislocation into a nanotwin and in situ TEM studies by Lee et al.[67] on austenitic steel show a considerable dislocation pile-up of suitably oriented screw dislocations at a CTB. In situ experiments by Chassagne et al.[66] also show that a pile-up of 8 dislocations is needed for dislocations to be transmitted through an annealing twin. This indicates that unimpeded cross-slip might not always be the case in copper and the possibility of a higher cross slip resistance should be discussed. When the CTB acts as a barrier with a certain threshold stress, dislocations would approach the boundary and pile up along it (Fig. 3.8 d). A pile-up can produce very high stresses locally since the shear stress at the first dislocation τ_1 can be described by $\tau_1 = \tau \cdot N$, with τ being the global shear stress and N the number of dislocations in the pile-up[68]. The number of dislocations as a function of shear stress τ, shear modulus G, Burgers vector b and pile-up length L_p for screw dislocations can be calculated as follows:

$$N = \frac{L_p \tau \pi}{Gb} \tag{3.3}$$

For the resolved shear stress of 53 MPa that was acting on the glide planes during deformation of the twin pillar, a pile-up of 10 dislocations can be calculated assuming a pile-up length of as little as 0.7 µm (approximately a third of the grain size). This pile-up leads to a stress at the dislocation front of approximately 530 MPa, being comparable with the values calculated by MD simulations. So even a moderate threshold stress for dislocation transmission can lead to similar results. Of course there is the possibility of more complicated processes, however, no deformation along the twin boundary or other features that would indicate the formation of dislocations with different Burgers vectors could be observed. To really resolve the barrier strength of the CTB and confirm the transfer process, further research using µLaue diffraction and TEM are necessary.

3.4.4. DDD simulations

The DDD simulations were carried out to validate the completely different mechanical behavior of the bicrystalline samples. The simulations of both, the bicrystals with impenetrable boundary as well as with semipermeable boundary resemble the behavior of the LAGB and CTB samples, respectively (Fig. 3.7). All simulated pillars with impenetrable boundary are characterized by tremendous hardening coupled with a strong rise in dislocation density due to dislocation pile-up/accumulation near

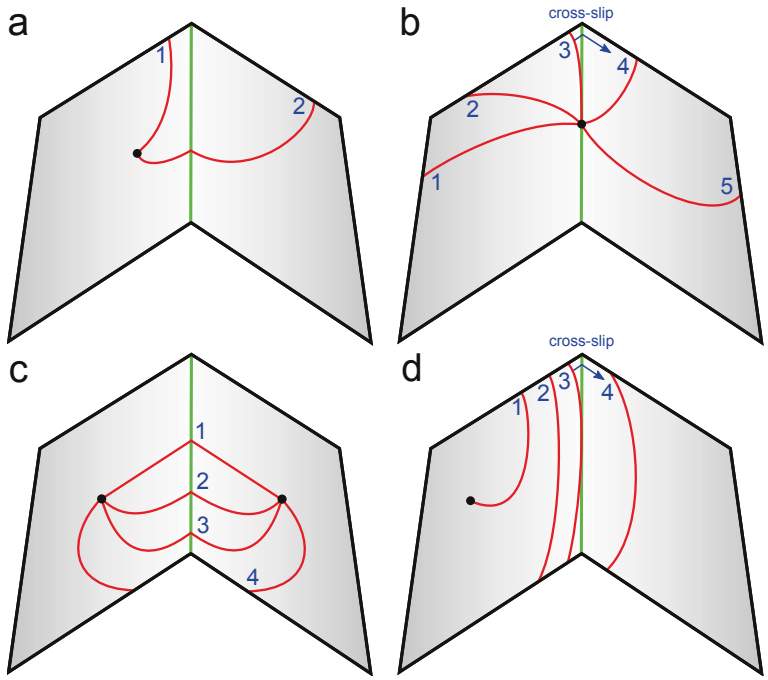

Figure 3.8.: Operation modes of various source types (black lines: glide planes; black dots: pinning points; green: twin boundary; red: dislocations). (a) Single-arm source that operates in a bicrystal with no cross-slip resistance. The same mechanism would work for a Frank-Read source. (b) Dislocation source with a pinning point in the boundary. Cross-slip occurs from 3 to 4. (c) Frank-Read source that has pinning points in both grains and crosses the boundary. From 1 to 3 the source operates parallel and is split into two single-arm sources at 4. (d) Source from (a) in a bicrystal with moderate cross-slip resistance. Dislocations will align along the CTB and transfer when the stress is sufficiently high.

the boundary.

The smaller pillar with semipermeable boundary ($0.5 \times 0.5 \times 1.5\,\mu m^3$) reaches a plateau at the same stress level as the single crystal, while the larger pillar with semipermeable boundary ($1 \times 1 \times 3\,\mu m^3$) exhibits a yield strength close to the one with impenetrable boundary and quickly levels off to a flow stress close to the single crystal. Since the pillars with semipermeable boundary contain no dislocation source on the slip system that is able to cross the boundary, all passing dislocations have to undergo cross-slip first. It is interesting to see, that these pillars behave similar to the single crystals, even though it is less likely to generate cross-slipping dislocations compared to the experimental orientation. With a $\langle 100 \rangle$ direction parallel to the compression axis, 8 equivalent slip systems with high Schmid-factors can be activated in the DDD simulation, of which one is allowed to cross the boundary. The CTB pillar of the experiment has four equivalent slip systems for its $\langle \bar{1}10 \rangle$ orientation, while two

of them can cross the boundary by cross-slip. This leads to the conclusion that a single easy deformation pathway determines the deformation behavior as long as the size and dislocation density of the sample provide enough sources on the required slip system.

3.5. Summary and Conclusion

Compression experiments on single crystalline and bicrystalline micrometer-sized Cu pillars were conducted. The pillars were deformed in displacement controlled mode to strains between 8 % and 19 % and show strongly varying behavior. Bicrystals containing the LAGB exhibit a bent pillar shape with a strong deflection of the grain boundary. Numerous small slip steps at the sample surface indicate the activation of many sources and no slip traces could be found that cross the interface. The stress-strain data shows increased yield stress and stronger hardening compared to the single crystalline pillars. This is attributed mostly to source truncation hardening in the smaller individual grains and the need for activation of less favorable sources due to exhaustion hardening. The examined boundary proves to be an effective barrier to dislocations making deformation more difficult and leading to a noticeable hardening.

The CTB pillar on the other hand shows no strengthening compared to the single crystals. This is explained by the special CTB orientation where screw dislocations can cross-slip from one grain into the other without impediment of the CTB at the applied stress. This proves that the strengthening effect of twin boundaries strongly depends on their orientation. While twin boundaries may strengthen bulk materials and even micropillars if the twin density is high enough, there are scenarios where twin boundaries do not significantly change the materials behavior.

Additional 3D DDD simulations show considerable hardening for an impenetrable boundary while a semipermeable boundary exhibits a behavior that is very close to the single crystals. In conclusion, the influence of boundaries can differ significantly, depending on the boundary type, orientation, sample size and dislocation density.

Acknowledgments

The authors thank LL Li, XH An and ZF Zhang of the Shenyang National Laboratory for Materials Science in China for providing the bulk Cu bicrystals. J Kreith of the Montanuniversität Leoben in Austria is acknowledged for the help with crystal orientations and coordinate transformations.

3. Differences in deformation behavior of bicrystalline Cu micropillars containing a twin- or a large angle grain boundary

Supplementary Material

The supplementary videos are included digitally on the storage medium located at the end of this thesis.

References for Chapter 3

[1] W.D. Nix. Mechanical properties of thin films. *Metallurgical and Materials Transactions A*, 20(11):2217–2245, 1989.

[2] E. Arzt, G. Dehm, P. Gumbsch, O. Kraft, and D. Weiss. Interface controlled plasticity in metals: dispersion hardening and thin film deformation. *Progress in Materials Science*, 46(3-4):283–307, 2001.

[3] G. Dehm. Miniaturized single-crystalline fcc metals deformed in tension: New insights in size-dependent plasticity. *Progress in Materials Science*, 54(6):664–688, 2009.

[4] B. Yang, C. Motz, W. Grosinger, W. Kammrath, and G. Dehm. Tensile behaviour of micro-sized copper wires studied using a novel fibre tensile module. *International journal of materials research*, 99(7):716–724, 2008.

[5] M.D. Uchic, D.M. Dimiduk, J.N. Florando, and W.D. Nix. Sample dimensions influence strength and crystal plasticity. *Science*, 305(5686):986, 2004.

[6] C. Motz, T. Schöberl, and R. Pippan. Mechanical properties of micro-sized copper bending beams machined by the focused ion beam technique. *Acta Materialia*, 53(15):4269–4279, 2005.

[7] D. Kiener, W. Grosinger, G. Dehm, and R. Pippan. A further step towards an understanding of size-dependent crystal plasticity: In situ tension experiments of miniaturized single-crystal copper samples. *Acta Materialia*, 56(3):580–592, 2008.

[8] J.R. Greer, W.C. Oliver, and W.D. Nix. Size dependence of mechanical properties of gold at the micron scale in the absence of strain gradients. *Acta Materialia*, 53(6):1821–1830, 2005.

[9] D.M. Norfleet, D.M. Dimiduk, S.J. Polasik, M.D. Uchic, and M.J. Mills. Dislocation structures and their relationship to strength in deformed nickel microcrystals. *Acta Materialia*, 56(13):2988–3001, 2008.

[10] E. Demir, F. Roters, and D. Raabe. Bending of single crystal microcantilever beams of cube orientation: Finite element model and experiments. *Journal of the Mechanics and Physics of Solids*, 58(10):1599–1612, 2010.

[11] A.T. Jennings and J.R. Greer. Tensile deformation of electroplated copper nanopillars. *Philosophical Magazine*, 91(7-9):1108–1120, 2011.

[12] S.H. Oh, M. Legros, D. Kiener, P. Gruber, and G. Dehm. In situ TEM straining of single crystal Au films on polyimide: Change of deformation mechanisms at the nanoscale. *Acta Materialia*, 55(16):5558–5571, 2007.

[13] G. Richter, K. Hillerich, D.S. Gianola, R. Mönig, O. Kraft, and C.A. Volkert. Ultrahigh Strength Single Crystalline Nanowhiskers Grown by Physical Vapor Deposition. *Nano letters*, 9(8):3048–3052, 2009.

[14] H. Bei, S. Shim, G.M. Pharr, and E.P. George. Effects of pre-strain on the compressive stress-strain response of Mo-alloy single-crystal micropillars. *Acta Materialia*, 56(17):4762–4770, 2008.

[15] P. Sudharshan Phani, K.E. Johanns, E.P. George, and G.M. Pharr. A simple stochastic model for yielding in specimens with limited number of dislocations. *Acta Materialia*, 61(7):2489–2499, 2013.

[16] T.A. Parthasarathy, S.I. Rao, D.M. Dimiduk, M.D. Uchic, and D.R. Trinkle. Contribution to size effect of yield strength from the stochastics of dislocation source lengths in finite samples. *Scripta Materialia*, 56(4):313–316, 2007.

[17] J.R. Greer and W.D. Nix. Nanoscale gold pillars strengthened through dislocation starvation. *Physical Review B*, 73(24):245410, 2006.

[18] S.I. Rao, D.M. Dimiduk, M. Tang, T.A. Parthasarathy, M.D. Uchic, and C. Woodward. Estimating the strength of single-ended dislocation sources in micron-sized single crystals. *Philosophical Magazine*, 87(30):4777–4794, 2007.

[19] S. Korte and W. Clegg. Discussion of the dependence of the effect of size on the yield stress in hard materials studied by microcompression of MgO. *Philosophical Magazine*, 91(7-9):1150–1162, 2011.

[20] R. Dou and B. Derby. A universal scaling law for the strength of metal micropillars and nanowires. *Scripta Materialia*, 61(5):524–527, 2009.

[21] S.I. Rao, D.M. Dimiduk, T.A. Parthasarathy, M.D. Uchic, M. Tang, and C. Woodward. Athermal mechanisms of size-dependent crystal flow gleaned from three-dimensional discrete dislocation simulations. *Acta Materialia*, 56(13):3245–3259, 2008.

[22] D.J. Dunstan and A.J. Bushby. The scaling exponent in the size effect of small scale plastic deformation. *International Journal of Plasticity*, 40(0):152–162, 2013.

[23] E. Hall. The deformation and ageing of mild steel: III discussion of results. *Proceedings of the Physical Society. Section B*, 64(9):747, 1951.

[24] N. Petch. The cleavage strength of polycrystals. *J. Iron Steel Inst*, 174(1):25–28, 1953.

[25] H. Gleiter. Nanocrystalline materials. *Progress in Materials Science*, 33(4):223–315, 1989.

[26] M.A. Meyers, A. Mishra, and D.J. Benson. Mechanical properties of nanocrystalline materials. *Progress in Materials Science*, 51(4):427–556, 2006.

[27] L. Lu, Y. Shen, X. Chen, L. Qian, and K. Lu. Ultrahigh strength and high electrical conductivity in copper. *Science*, 304(5669):422, 2004.

[28] N. Mara, D. Bhattacharyya, P. Dickerson, R. Hoagland, and A. Misra. Deformability of ultrahigh strength 5 nm Cu/Nb nanolayered composites. *Applied physics letters*, 92:231901, 2008.

[29] D. Bhattacharyya, N.A. Mara, P. Dickerson, R.G. Hoagland, and A. Misra. Compressive flow behavior of Al-TiN multilayers at nanometer scale layer thickness. *Acta Materialia*, 59(10):3804–3816, 2011.

[30] J.Y. Zhang, G. Liu, and J. Sun. Comparisons between homogeneous boundaries and heterophase interfaces in plastic deformation: Nanostructured Cu micropillars vs. nanolayered Cu-based micropillars. *Acta Materialia*, 61(18):6868–6881, 2013.

[31] J.Y. Zhang, S. Lei, Y. Liu, J.J. Niu, Y. Chen, G. Liu, X. Zhang, and J. Sun. Length scale-dependent deformation behavior of nanolayered Cu/Zr micropillars. *Acta Materialia*, 60(4):1610–1622, 2012.

[32] A. Rinaldi, P. Peralta, C. Friesen, and K. Sieradzki. Sample-size effects in the yield behavior of nanocrystalline nickel. *Acta Materialia*, 56(3):511–517, 2008.

[33] J.Y. Zhang, G. Liu, and J. Sun. Strain rate effects on the mechanical response in multi- and single-crystalline Cu micropillars: Grain boundary effects. *International Journal of Plasticity*, 50(0):1–17, 2013.

[34] X.W. Gu, C.N. Loynachan, Z. Wu, Y.-W. Zhang, D.J. Srolovitz, and J.R. Greer. Size-Dependent Deformation of Nanocrystalline Pt Nanopillars. *Nano letters*, 12(12):6385–6392, 2012.

[35] D. Jang, C. Cai, and J.R. Greer. Influence of Homogeneous Interfaces on the Strength of 500 nm Diameter Cu Nanopillars. *Nano letters*, 2011.

[36] D. Jang and J.R. Greer. Size-induced weakening and grain boundary-assisted deformation in 60 nm grained Ni nanopillars. *Scripta Materialia*, 64(1):77–80, 2011.

[37] D. Jang, X. Li, H. Gao, and J.R. Greer. Deformation mechanisms in nanotwinned metal nanopillars. *Nature Nanotechnology*, 2012.

[38] K.S. Ng and A.H.W. Ngan. Deformation of micron-sized aluminium bi-crystal pillars. *Philosophical Magazine*, 89(33):3013–3026, 2009.

[39] H. Fan, Z. Li, and M. Huang. Toward a further understanding of intermittent plastic responses in the compressed single/bicrystalline micropillars. *Scripta Materialia*, 66(10):813–816, 2012.

[40] A. Kunz, S. Pathak, and J.R. Greer. Size effects in Al nanopillars: Single crystalline vs. bicrystalline. *Acta Materialia*, 59(11):4416–4424, 2011.

[41] G.J. Tucker, Z.H. Aitken, J.R. Greer, and C.R. Weinberger. The mechanical behavior and deformation of bicrystalline nanowires. *Modelling and Simulation in Materials Science and Engineering*, 21(1):015004, 2013.

[42] Z.H. Aitken, D. Jang, C.R. Weinberger, and J.R. Greer. Grain Boundary Sliding in Aluminum Nano-Bi-Crystals Deformed at Room Temperature. *Small*, 2013.

[43] N. Kheradmand, A. Barnoush, and H. Vehoff. Investigation of the role of grain boundary on the mechanical properties of metals. *Journal of Physics: Conference Series*, IOP Publishing, 240(1), 2010.

[44] N. Kheradmand, J. Dake, A. Barnoush, and H. Vehoff. Novel methods for micromechanical examination of hydrogen and grain boundary effects on dislocations. *Philosophical Magazine*, 92(25-27):3216–3230, 2012.

[45] N. Kheradmand and H. Vehoff. Orientation Gradients at Boundaries in Micron-Sized Bicrystals. *Advanced Engineering Materials*, 14(3):153–161, 2012.

[46] N. Kheradmand, H. Vehoff, and A. Barnoush. An insight into the role of the grain boundary in plastic deformation by means of a bicrystalline pillar compression test and atomistic simulation. *Acta Materialia*, 61(19):7454–7465, 2013.

[47] V. Sriram, J.-M. Yang, J. Ye, and A.M. Minor. In-situ metrology and testing of nanotwinned copper pillars for potential air gap applications. *Microelectronic Engineering*, 87(11):2046–2049, 2010.

[48] L.L. Li, X.H. An, P.J. Imrich, P. Zhang, Z.J. Zhang, G. Dehm, and Z.F. Zhang. Microcompression and cyclic deformation behaviors of coaxial copper bicrystals with a single twin boundary. *Scripta Materialia*, 69(2):199–202, 2013.

[49] G. Moser, H. Felber, B. Rashkova, P.J. Imrich, C. Kirchlechner, W. Grosinger, C. Motz, G. Dehm, and D. Kiener. Sample Preparation by Metallography and Focused Ion Beam for Nanomechanical Testing. *Practical Metallography*, 49(6):343–355, 2012.

[50] C. Kirchlechner, J. Keckes, J.-S. Micha, and G. Dehm. In Situ mu Laue: Instrumental Setup for the Deformation of Micron Sized Samples. *Advanced Engineering Materials*, 13(8):837–844, 2011.

[51] E. Van der Giessen and A. Needleman. Discrete dislocation plasticity: a simple planar model. *Modelling and Simulation in Materials Science and Engineering*, 3(5):689, 1999.

[52] D. Weygand, L.H. Friedman, E.V.d. Giessen, and A. Needleman. Aspects of boundary-value problem solutions with three-dimensional dislocation dynamics. *Modelling and Simulation in Materials Science and Engineering*, 10(4):437, 2002.

[53] D. Weygand and P. Gumbsch. Study of dislocation reactions and rearrangements under different loading conditions. *Materials Science and Engineering: A*, 400-401(0):158–161, 2005.

[54] C. Motz, D. Weygand, J. Senger, and P. Gumbsch. Micro-bending tests: A comparison between three-dimensional discrete dislocation dynamics simulations and experiments. *Acta Materialia*, 56(9):1942–1955, 2008.

[55] O. Kraft, P.A. Gruber, R. Mönig, and D. Weygand. Plasticity in confined dimensions. *Annual Review of Materials Research*, 40:293–317, 2010.

[56] Y. Xiang and J.J. Vlassak. Bauschinger and size effects in thin-film plasticity. *Acta Materialia*, 54(20):5449–5460, 2006.

[57] P.A. Gruber, J. Böhm, F. Onuseit, A. Wanner, R. Spolenak, and E. Arzt. Size effects on yield strength and strain hardening for ultra-thin Cu films with and without passivation: A study by synchrotron and bulge test techniques. *Acta Materialia*, 56(10):2318–2335, 2008.

[58] Z. Shan, R.K. Mishra, S.A.S. Asif, O.L. Warren, and A.M. Minor. Mechanical annealing and source-limited deformation in submicrometre-diameter Ni crystals. *Nature Materials*, 7(2):115–119, 2007.

[59] C.A. Volkert and E.T. Lilleodden. Size effects in the deformation of sub-micron Au columns. *Philosophical Magazine*, 86(33-35):5567–5579, 2006.

[60] H.P. Stüwe. *Mechanische Anisotropie*. Springer, Vienna, 1974.

[61] B. Daum, G. Dehm, H. Clemens, M. Rester, F.D. Fischer, and F.G. Rammerstorfer. Elastoplastic buckling as source of misinterpretation of micropillar tests. *Acta Materialia*, 61(13):4996–5007, 2013.

[62] D. Kiener, C. Motz, and G. Dehm. Micro-compression testing: A critical discussion of experimental constraints. *Materials Science and Engineering: A*, 505(1-2):79–87, 2009.

[63] F. Mompiou, D. Caillard, M. Legros, and H. Mughrabi. In situ TEM observations of reverse dislocation motion upon unloading in tensile-deformed UFG aluminium. *Acta Materialia*, 60(8):3402–3414, 2012.

[64] G. Dehm, T.J. Balk, H. Edongué, and E. Arzt. Small-scale plasticity in thin Cu and Al films. *Microelectronic Engineering*, 70(2-4):412–424, 2003.

[65] Z.H. Jin, P. Gumbsch, E. Ma, K. Albe, K. Lu, H. Hahn, and H. Gleiter. The interaction mechanism of screw dislocations with coherent twin boundaries in different face-centred cubic metals. *Scripta Materialia*, 54(6):1163–1168, 2006.

[66] M. Chassagne, M. Legros, and D. Rodney. Atomic-scale simulation of screw dislocation/coherent twin boundary interaction in Al, Au, Cu and Ni. *Acta Materialia*, 59(4):1456–1463, 2011.

[67] T. Lee, I. Robertson, and H. Birnbaum. An In Situ transmission electron microscope deformation study of the slip transfer mechanisms in metals. *Metallurgical Transactions A*, 21(9):2437–2447, 1990.

[68] D. Hull and D.J. Bacon. *Introduction to dislocations*. Butterworth-Heinemann, Oxford, fourth ed. edition, 2001.

4

In situ TEM microcompression of single and bicrystalline samples: insights and limitations

Peter J. Imrich[a], Christoph Kirchlechner[b,c], Daniel Kiener[c], Gerhard Dehm[b,c]

[a]Erich Schmid Institute of Materials Science, Austrian Academy of Sciences, Leoben, Austria

[b]Max-Planck-Institut für Eisenforschung, Düsseldorf, Germany

[c]Department of Materials Physics, Montanuniversität Leoben, Austria

How would you...

...describe the overall significance of this paper?

This manuscript describes the challenges and limitations of in situ (S)TEM small scale mechanical testing with the help of compression experiments on Cu samples containing a twin boundary. Guidelines are given how to set-up the experiment in a way that meaningful mechanical data can be obtained and the sample quality permits to observe dislocation plasticity.

...describe this work to a materials science and engineering professional with no experience in your technical speciality?

Interlinking the mechanical behavior to the underlying and evolving microstructure is mandatory for mechanism based material models. Possibilities and challenges of miniaturized in situ compression experiments in the TEM are demonstrated for a fundamental problem in materials science where high spatial resolution is required: The dislocation-twin boundary interaction.

...describe this work to a layperson?

Current technologies, e. g. in the area of microelectronics and nanoengineered materials, all utilize very small structures, which have (just by their mere dimension) different mechanical properties than the same materials at large scales. In situ micromechanical experiments offer the possibility to characterize and understand these properties for improving materials for modern applications.

Abstract

In situ micromechanical compression experiments in a transmission electron microscope enable the study and analysis of small scale deformation behavior. The implementation of instrumented indenter systems allows measuring force and displacement, providing additionally insights on sample strength and flow behavior. Using focused ion beam sample preparation, single- and bicrystalline specimens can be fabricated to study the influence of individual grain boundaries on the mechanical behavior. Taperless single crystalline and bicrystalline Cu compression pillars including a coherent

twin boundary were deformed in scanning- and conventional transmission electron microscopy mode to study the applicability of both techniques for examining dislocation dynamics and interaction with the boundary. Based on experimental results, possibilities and limitations of such experiments are critically discussed, including sample preparation, in situ annealing to remove ion beam induced defects, imaging of dislocations, and acquisition of stress-strain data. Finally, an outlook is given on the potential of micromechanical in situ transmission electron microscopic experiments for analyzing the influence of grain boundaries on the mechanical behavior.

4.1. Introduction

The mechanical properties of materials in small dimensions have been intensely studied in the last decade. It was found that, for example, the strength changes by simply reducing the sample size in one dimension (thin films[1,2]), two dimensions (thin wires[3,4]) or three dimensions (micromechanical samples[5–7]). The development of techniques to manufacture micromechanical compression pillars by focused ion beam (FIB) milling sparked this new era of investigations and showed that no strain gradients are required to explain the high strength of samples in the low micrometer region[8]. This mechanical size effect in metals, frequently described by increasing strength with decreasing sample size, is now well established and explained by a reduction in the number of dislocation sources[9], shutdown of active sources (dislocation exhaustion)[10], decrease in source size due to intersection with the sample surface (source truncation)[11], and reduction in dislocation density by escape to the free surface (dislocation starvation)[12].

To better understand the dislocation processes accountable for these effects, more and more transmission electron microscopy (TEM) experiments are being conducted. Conventionally, in situ experiments were carried out either using straining holders, where a thin film was strained along with the sample support[13–16], or in heating holders, where a thin film on a thinned substrate was heated and deformed due to the mismatch in thermal expansion[17,18]. Both options allow the observation of dislocation motion, however, stress and strain can only be measured locally by analyzing the curvature of dislocation segments and image correlation, respectively[10,15,16]. The introduction of microelectromechanical systems (MEMS) further broadened the prospects of in situ TEM testing, reaching from structures used in straining holders with stress and strain measuring capabilities through TEM imaging[19] to elaborate active MEMS with thermal actuators and capacitive sensors[20] or simple push to pull devices that need indenters for operation[21,22]. The introduction of in situ inden-

ters combined with FIB manufacturing opened up countless possibilities of sample designs including compression, tension or bending experiments with exact indenter positioning and defined strain rate, while simultaneously measuring force and displacement[23].

Important contributions to the understanding of the deformation behavior in miniaturized samples were made with the help of such integrated indenter systems. Shan et al.[24] observed that micromechanical Ni samples can lose defects upon mechanical compression as proposed by Greer et al.[12]. Kiener et al. found that in Cu compression samples not only yield but also hardening is determined by source availability[25], that tensile samples in multi-slip orientation show sustained plastic deformation while single slip samples fail by slip localization[26], and that source truncation and exhaustion hardening occur simultaneously while Taylor hardening breaks down in small samples[27]. Chisholm et al.[28] showed that yield strength and deformation behavior of Mo fibers depend on the dislocation density, leading to catastrophic failure for dislocation free fibers and substantial plastic deformation for fibers containing lots of dislocations.

Nanoindentation devices for the TEM are increasingly used for quantitative mechanical tests of submicron sized objects[29]. Complex sample preparation and careful execution are fundamental; however, if used properly invaluable information of deformation mechanisms can be gathered. Therefore, this article is aimed at demonstrating the benefits and challenges of micromechanical experiments in the TEM, with a special focus on miniaturized samples containing a single grain boundary, where Cu was selected as a model material.

4.2. Experimental Details

This section describes the sample preparation and testing procedure.

A Kleindiek micromanipulator was used to lift $40 \times 20 \times 4\,\mu m^3$ sized lamellae out of a macroscopic bicrystal that was grown by the Bridgman method from OFHC copper with 99.999 % purity. The lamellae were attached to an Omniprobe® Lift-Out grid using tungsten deposition, and electron transparent windows were milled with a Zeiss Auriga® dual beam FIB workstation with currents reaching from 120 pA down to 20 pA. Compression samples with a nominal size of either $400 \times 400 \times 200\,nm^3$ or $650 \times 650 \times 200\,nm^3$ leading to aspect ratios of 2:1 or 3.3:1, respectively, were cut in both single crystalline parts as well as the bicrystalline region. To generate parallel surfaces of the compression samples the lamellae were overtilted by 1–2° during milling to compensate for taper. The bicrystalline compression pillar contained a coherent twin

boundary that spanned from top to bottom of the sample nearly parallel to the $[1\bar{1}0]$ compression direction. To enable observation of the twin boundary plane during compression testing, the samples were prepared such that the boundary was inclined to the electron beam at 0° goniometer tilt (Fig. 4.1). All samples were heated in situ in the TEM to 480 °C for 25 min at 2×10^{-7} mbar using a Gatan heating holder in order to reduce FIB damage (Fig. 4.2) as suggested by Kiener et al.[30]. After annealing, the samples were compressed with a B-doped diamond flat punch in a Hysitron PI 95 PicoIndenter® using the displacement controlled mode with a 78 kHz feedback loop inside a Jeol 2100F TEM operated at 200 kV. A displacement rate of 1 nm/s, leading to a strain rate of $\sim 2 \times 10^{-3}\,\mathrm{s}^{-1}$ was used while observing the samples in either TEM or scanning transmission electron microscopy (STEM) mode. Video acquisition was performed at 8 fps or 0.7 fps, for TEM and STEM, respectively, while force and displacement data was acquired at 200 points per second and plotted using a sliding average filter with 7 measurements for each plotted point.

FEM simulations on $0.2 \times 0.4 \times 0.4.\,\mu\mathrm{m}^3$ and $0.2 \times 0.65 \times 0.65\,\mu\mathrm{m}^3$ sized samples on a $0.2 \times 2.5 \times 3\,\mu\mathrm{m}^3$ lamella were conducted using a NX Nastran solver and isotropic elastic properties of bulk polycrystalline Cu to estimate the elastic deformation of the pillar and the sample base.

4.3. Results and Discussion

Miniaturized experiments performed in situ in the TEM offer precious insights into the small scale deformation behavior. Flow stresses of such microsamples were shown to be determined by the microstructure, the dislocation density and the dislocation-dislocation and dislocation-boundary interactions[31], all of which can be observed in the TEM[16]. This chapter will present experimental data to address and discuss insights and challenges during micromechanical in situ experiments in the TEM. Section 4.3.1 will discuss sample preparation, section 4.3.2 will focus on the visualization of dislocations and the challenges that occur during elastic loading, section 4.3.3 will concentrate on the deformation behavior and the imaging of moving dislocations, and finally section 4.3.4 will review challenges regarding the sample compliance.

4.3.1. Sample preparation

Figure 4.1 shows the two macrosamples (MS) and a magnified image of the bicrystalline compression pillar of MS2. To allow the observation of dislocations during in situ TEM experiments, the sample has to be electron transparent, but should not

be too thin as to achieve useful mechanical data, avoid buckling, as well as probe enough volume for the observation of dislocation movement. The approach taken for the present experiments was first shaping an electron transparent lamella with parallel surfaces and roughly 200 nm thickness before realizing the sample shape by milling perpendicular to the compression direction (including an overtilt of $\sim 2°$). The downsides of this method are an increased fabrication time and a more compliant substrate (depending on the size of the transparent windows); the benefits are a constant cross-section across the gauge length and the possibility of making the sample wider to enlarge the volume of each grain. The latter point is especially important for the observation of bicrystalline samples, making more room for dislocations to travel to the boundary and increasing the area that is visible in the TEM. As shown in Fig. 4.1 c, the twin boundary is inclined to the electron beam, allowing the observation of the grain boundary plane for easier identification of dislocation-grain boundary interactions.

After the FIB manufacturing process, the samples possess many surface defects as depicted in Fig. 4.2 a. As suggested in[30] an in situ heat treatment was performed to reduce the FIB induced damage. If this is done with an in situ heating stage, annealing times and temperature can be systematically changed to obtain high quality specimens. Note that excessive heating may cause geometrical changes due to minimization of surface energy or even loss of material by melting or evaporation. Well annealed samples exhibit clear dislocation contrast, allowing to accurately trace dislocation movement (Fig. 4.2 b).

4.3.2. Elastic loading

The outstanding advantage of in situ micromechanical experiments in the TEM, besides the possibility of measuring mechanical properties of materials (Fig. 4.3), is to visualize the processes responsible for the deformation of the sample. In the case of crystalline metals, this is of course visualizing dislocations and dislocation interaction processes. However, the complex setup and the manipulation of the material pose difficulties compared to static TEM observations, which are reported in this section.

To achieve good dislocation contrast, the sample is generally oriented in a two-beam imaging condition using either bright field or dark field imaging, with weak beam dark field imaging being preferred due to a higher signal to noise ratio for dislocations imaged in bright contrast[26,27,32]. To use this technique the diffraction vectors in both grains have to be the same, which is only possible in very few orientations for a twin boundary and impossible for most arbitrary boundaries. Therefore using

Figure 4.1.: SEM images of the macrosamples (MS): (a) MS1 attached to the liftout grid on the left side. Inset: Calculated decrease in apparent modulus due to the elastic bending of the macrosample (continuous line) and measured elastic moduli. (b) MS2 is fixed by W deposition on both sides. (c) Magnified view of the bicrystalline micropillar of MS2. The position of the twin boundary is marked with a dotted line.

two different diffraction vectors in bright field mode is obligatory for imaging most bicrystals. Even then, only a very limited number of double two beam conditions can be achieved when using a single tilt holder which tilts solely about the goniometer axis. Possibly high index reflections have to be used for at least one grain resulting in inferior dislocation contrast which is a common limitation of most nanoindentation holders.

Two methods which both have advantages and disadvantages were pursued to attain best static and dynamic dislocation contrast: STEM and TEM imaging. The choice of working in STEM mode for MS1 was made to minimize the influence of bend contours and maximize the dislocation contrast. The achieved imaging quality is good, showing clear dislocation contrast in single- as well as bicrystals, as illustrated in Fig. 4.4. During elastic loading the dislocation contrast was lost at times

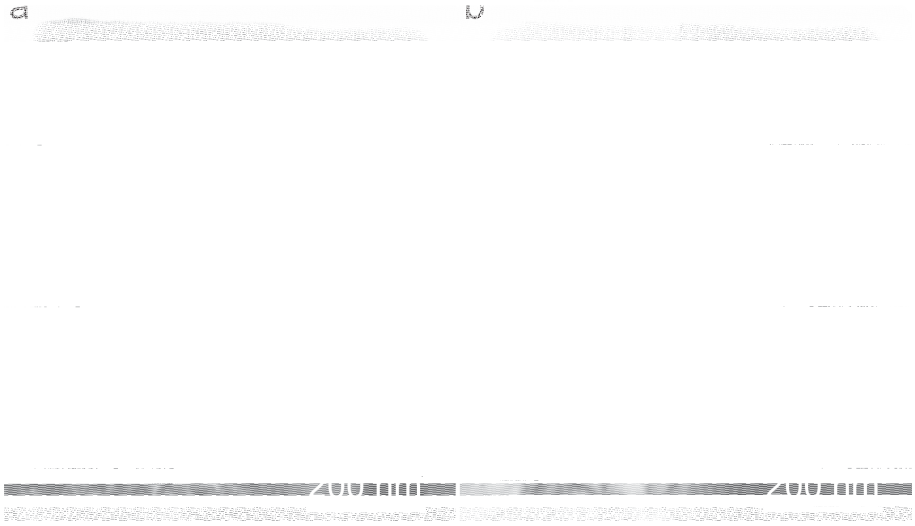

Figure 4.2.: TEM micrographs of the bicrystalline sample on MS2 (a) before and (b) after in situ annealing at 480 °C for 25 min.

due to slight reorientation or bending (0.5–1°) of the sample (Fig. 4.5 a). Several factors play a role in this problem: Experimental misorientation, sample rotation during plastic deformation due to constraints and elastic or elastoplastic buckling. During manufacturing of the sample, careful attention was paid to assure correct sample orientation and the top surface was cut using an overtilt to account for the FIB taper. However, perfect alignment is hard to achieve in sub-micrometer experiments. Moreover, the lateral constraints imposed by the indenter setup lead to a crystallographic rotation of the sample during deformation by inhibiting the lateral shift of the sample[33–36]. Therefore, the sample was loaded and fully unloaded in successive steps, thereby also allowing for the acquisition of (S)TEM micrographs which are not influenced by indenter vibrations in the unloaded out-of-contact situation. While it is possible to adjust the goniometer tilt during deformation to regain dislocation contrast, this was omitted to avoid vibrations that could lead to instabilities in the indenter system and consequently damage the sample. However, the tilt can be adjusted between each incremental deformation step to regain optimal imaging conditions, which was the approach pursued in the experiments presented here.

All samples on MS2 were tested using TEM imaging, with the advantage of a faster frame rate of 8 fps to image dynamic dislocation processes as discussed in the next section. While TEM imaging provides good dislocation contrast, as shown in Fig. 4.6, it is inferior to STEM imaging and increasingly influenced by bend contours, possibly leading to shadowing of dislocations during compression. Figure 4.5 b illustrates the

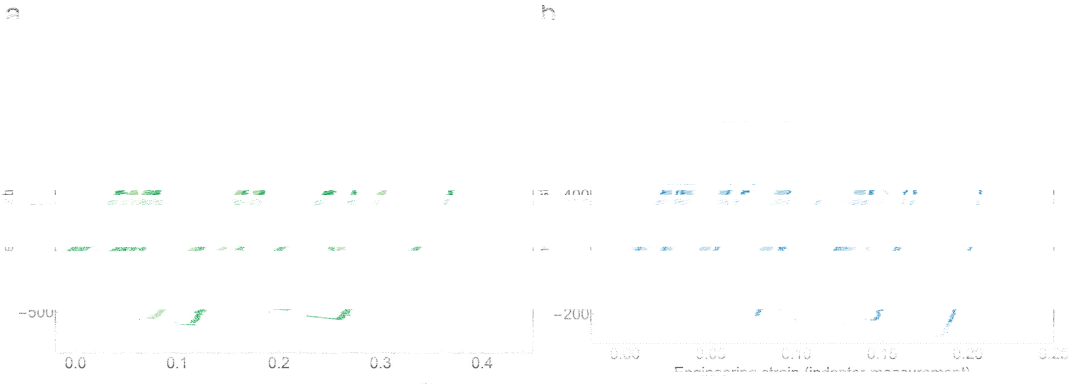

Figure 4.3.: Selected stress-strain curves of single crystalline (light color) and bicrystalline (dark color) compression samples of (a) MS1 and (b) MS2. MS1 shows higher flow stresses and lower apparent elastic moduli than MS2. The arrows mark strain bursts that are followed by load drops.

lost contrast during compression of a single crystalline sample on MS2.

Another important and much debated point is the aspect ratio of the compression pillars: large ratios probe a bigger volume and allow glide that is not obstructed by the pillar base and the flat punch[33], but are more prone to elastic or elastoplastic buckling[37]. Therefore, an aspect ratio of 2:1 to 3:1 (length:thickness) is usually recommended for compression samples[36,38] and was used for our experiments.

4.3.3. Onset of plasticity

The use of an instrumented indenter inside the TEM allows recording of force-displacement data, giving direct information on mechanical properties of the specimens. All tested pillars exhibit the characteristic stochastic flow, as commonly seen for samples in these dimensions and discussed elsewhere[24,25]. The stress-strain curves in Fig. 4.3 illustrate that the flow stresses of the bicrystalline pillars are similar to the single crystals, showing that the twin boundary does not lead to significant strengthening or hardening. For a discussion on this phenomenon, the reader is referred to recent publications[39,40]. One point that stands out is the difference in yield strengths for MS1 and MS2, ranging from 1000 MPa up to 1750 MPa and 400 MPa up to 950 MPa for MS1 and MS2, respectively. Both lamellae were lifted out of the same material within 50 µm distance, prepared and measured in the same FIB using the same ion currents and annealed and tested in the same TEM with the identical indenter system, so preparation and measuring errors cannot explain the significant differences. The thicknesses deviate by less than 5 %, excluding a strength increase

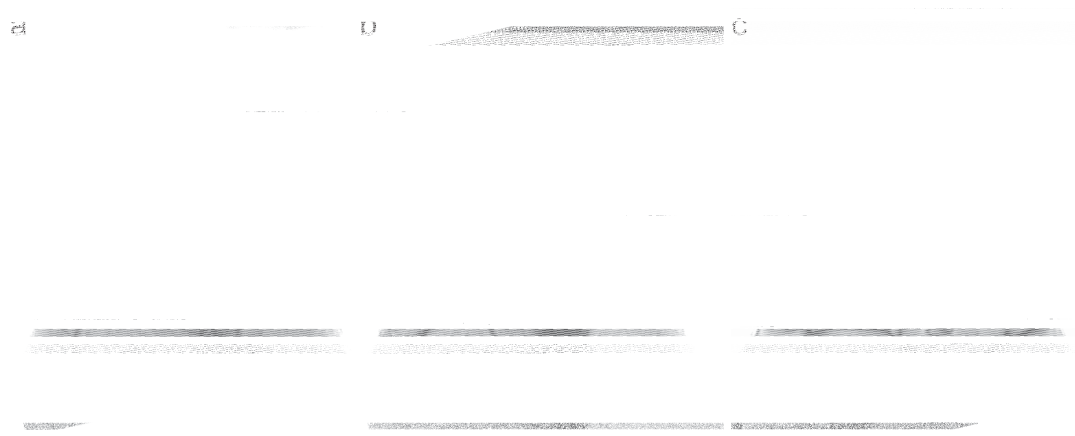

Figure 4.4.: STEM micrographs of samples on MS1. Video frame of the bicrystalline pillar (a) before and (b) during deformation. (c) STEM scan of a single crystalline sample before deformation.

due to the mechanical size effect[8]. The only discernible differences are the attachment of the macrosample and the deviation of aspect ratios. As discussed further below, the difference in sample fixture should not influence the yield stresses; the change in aspect ratio from 2:1 to 3.3:1, however, can have an effect on the stress-strain behavior since a larger volume is probed. This leads to a higher likelihood of encountering a dislocation source that is easy to activate. Furthermore, the dislocation density in the bicrystal on MS2 shows a more constant dislocation density that stays at a higher level compared to the one on MS1[40]. It is worth mentioning that the noise in the stress-strain curves varies for the different pillars, which is due to changing subtle vibrations of the surrounding environment although the TEM room is shielded against electromagnetic fields, sudden temperature fluctuations, and acoustically insulated. It was observed that the strain determined from the indenter displacement does not correspond to the strain measured from in situ TEM images, highlighting the importance of in situ observations. This discrepancy is due to system compliance and plastic deformation of the pillar base. A promising method to gain correct and continuous displacement data is digital image correlation, which is well developed and frequently used for in situ SEM tests[41,42], but still in an early stage for TEM use[16]. The movement of high contrast features such as bend contours and dislocations makes it hard for the software to consistently recognize individual features. However, manual strain measurements using in situ images were acquired with an error of 0.002–0.003 per pixel, and a second strain axis based on this data was introduced in Fig. 4.3. It is important to understand that the difficulty of measuring strain does not translate to problems in stress measurement, which is paramount for

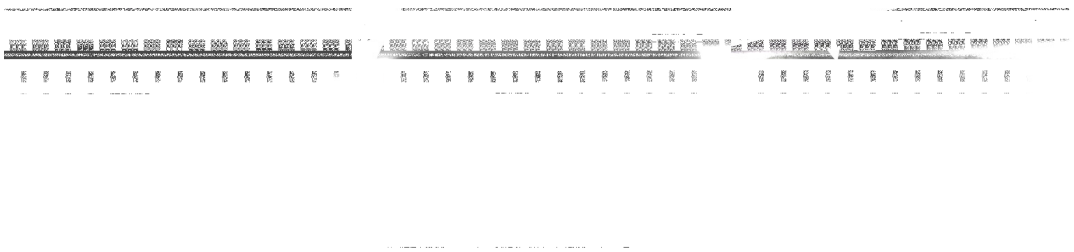

Figure 4.5.: Imaging difficulties during compression testing. (a) Slight sample rotation causes loss of diffraction contrast in the left grain. (b) Bend contours shadow dislocation movement in TEM mode. (c) Limited frame rate during STEM scanning leads to abrupt change in contrast at strain bursts (marked by arrow). Note that the micrographs were rotated during post processing, leading to a diagonal scan line.

analyzing size effects in small dimensions. As shown in a previous publication[40], the activation of dislocation sources can only be properly analyzed when the activation event is slow enough to be captured. The formation of a favorable dislocation source leads to a load drop in perfectly displacement controlled systems. However, the 78 kHz feedback loop of the used indenter system is not fast enough to sustain the specified displacement, leading to strain bursts (arrows in Fig. 4.3) with high dislocation speeds due to the large amount of energy stored in the transducer springs. These bursts are followed by load drops when the feedback control starts regulating the displacement after the overshoot. This effect is commonly observed in similar experiments[12,24–28,32,41] and poses a drawback for the analysis of dislocation source activation processes. The increased frame rate of 8 fps using TEM imaging compared to 0.7 fps using STEM facilitated the observation of dynamic processes, but was too slow to capture dislocation avalanches. A frame rate of approx. 10^{11}–10^{12} fps would be necessary to track dislocations travelling at the speed of sound[43]. Strain bursts with a lower dislocation speed such as observed in Fig. 4.3 would still require frame rates exceeding 10^6 fps. Modern camera systems such as direct electron detectors that are currently in development[44,45] with up to 1600 fps will be able to image dislocation movement to greater temporal detail, but will still fail to capture all of the deformation process, unless more stable indenter systems are used. Consequently, this implies that a sharp dislocation image is to be regarded as a quasi-static representation of the dislocation structure, an important consideration for evaluating

Figure 4.6.: TEM micrographs of samples on MS2. Bicrystalline pillar (a) before and (b) during compression testing. (c) Single crystalline sample during compression testing.

stresses from dislocation curvature analysis[15].

4.3.4. Unloading

The elastic properties of materials are best evaluated during unloading to minimize the effects from the initial contact situation. The slopes of the unloading curves of MS1 exhibit a great variation of 18 GPa to 70 GPa for all samples on MS1 (not all shown in Fig. 4.3 a). This scatter in compliance, which is depicted as points in the overlay in Fig. 4.1 a, can be explained by considering the geometry of the macrosample. Figure 4.1 a shows an SEM image of MS1, revealing that the lift-out lamella is fixed to the Cu grid only on one side, thus acting as a cantilever. This shortcoming can be addressed by adding the elastic deflection of the lift-out lamella at the position of the sample to the theoretical elastic strain of the pillar, based on which an apparent modulus can be calculated. This apparent modulus drops from 130 GPa down to 66 GPa for the sample at the very right side (Fig. 4.1 a: solid line in overlay). Such a strong influence might not be expected and shows that sound sample preparation and rigid fixation are important factors. The lamella of MS2 presented in Fig. 4.1 b was attached on both sides, which is reflected in the steeper and parallel unloading curves in Fig. 4.3. However, even for MS2 the measured apparent elastic modulus of 56 GPa is too low, which is a quite common feature for micromechanical tests[27,38,46].

For a better estimate of the elastic sink in due to the compliant sample base in this configuration, FEM simulations were performed. Figure 4.7 shows the normalized displacement for pillars with similar shape as in the experiments. Only 36 % or 41 %

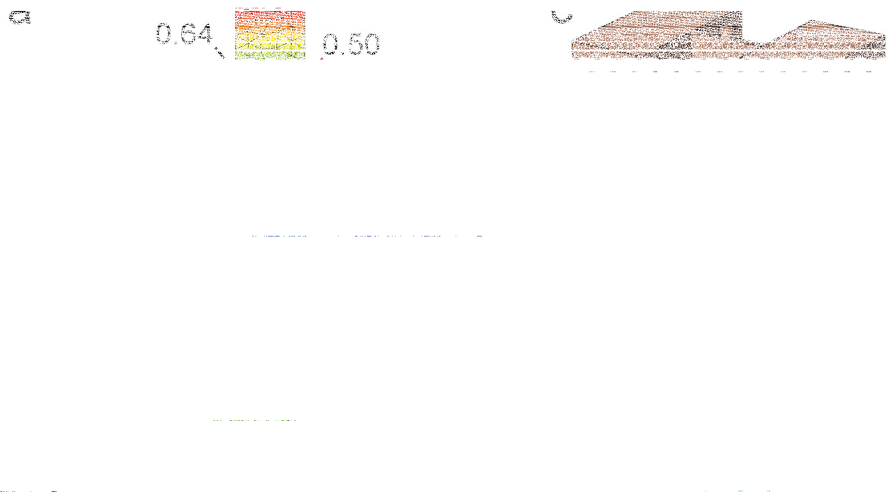

Figure 4.7.: FEM analysis of elastic sample sink-in during loading. The normalized displacement is plotted for (a) 400 nm sized and (b) 650 nm sized samples, respectively. Thick black lines indicate significant displacement of the base, accounting for (a) 0.64, (b) 0.59 of the entire displacement. (c) Schematic of the simulation setup.

of the total elastic deformation is localized in the pillar itself for MS1 or MS2, respectively, while the rest is accommodated by the thin sample base shown in Fig. 4.7 c. This compliance leads to a reduction in apparent elastic modulus from 130 GPa to approx. 47 GPa and 53 GPa, respectively. Thus, by accounting for the compliance of the system and the cantilever effect, the low measured elastic moduli of samples on MS1 can be explained.

This raises the question whether such a sample geometry is practical to study bicrystalline deformation behavior. The increased compliance makes an evaluation of the Young's modulus impractical and influences the strain measurement. However, the analysis of dislocation source activation or grain boundary strength require predominantly an accurate stress measurement (which is not influenced by a lowered compliance) and enough volume for dislocation sources to operate and emitted dislocations to glide to the twin boundary. Therefore, a rectangular cross-section with increased width is expedient, which cannot be realized by other pillar manufacturing processes such as lathe milling or annular milling[8,12]. Regarding the compliance of

the sample base, even a perfect electron transparent cylindrical pillar on an infinite half-space would show plastic sink-in additional to the elastic sink-in calculated by Sneddon[47] due to the high strength of the micropillar compared to the bulk support.

Lastly, Fig. 4.3 shows that the samples get pulled in tension after unloading due to adhesion between flat diamond tip and sample top, until they finally separate. Interestingly, a nonlinearity in the unloading slope is observable, even at compressive stresses, but most prominent in the tensile regime. This goes along with the observation of reverse dislocation motion in the TEM, which increases when reaching tensile stresses (Fig. 4.3 a). Such observations of an early Bauschinger effect during unloading were also made in micro-bending beams[7,48–50] and in ultrafine-grained films[51,52]. These findings are relevant for the interpretation of post-mortem TEM analyses, since the dislocation structures at load and after unloading do not coincide.

4.4. Outlook

To gain further insights into the interactions of dislocations with boundaries, additional experiments are necessary. Sample bending and the use of a single tilt holder complicate the observation of deformation processes. Utilizing tensile samples would improve on this issue by reducing bending during deformation and allowing for higher aspect ratios, leading to a larger observable volume. That said, the downside of tensile experiments in the TEM is that they require tedious sample preparation, independently whether a gripper[27] or a push to pull device[28] is used.

If the interaction process of dislocations with the boundary is the sole purpose of the experiment and stress-strain information is irrelevant, indentation of a conventionally prepared wedge[53] with a wedge shaped indenter could offer a simple experimental possibility. A well-chosen sample orientation leads to the generation of dislocations on a defined slip system and subsequent interaction with the boundary upon indentation[54].

Another crucial point regarding the observation of dislocation movement is their high speed. The development of fast direct electron detectors will increase temporal resolution, but it is questionable if fast moving dislocations will be detectable in the near future. To observe dislocation source activation and interaction processes, the use of truly displacement controlled indenters is more profitable, since it leads to load drops instead of strain bursts once a new dislocation source is activated, causing an arrest until the activation stress is reached again.

The development of advanced digital image correlation software which does not rely on large fiducial markers that shadow parts of the TEM sample could provide

continuous local strain data, regardless of compliance and plastic deformation of the sample base. Finally, the generation of tensile stresses during unloading of the pillars due to adhesion of the sample surface and the flat punch is unwanted for compression experiments but offers the possibility to conduct in situ compression-tension fatigue experiments in the TEM with little additional effort[55].

4.5. Summary

The possibility of imaging single dislocations, observe their movement, dynamics and interactions while capturing continuous stress-strain data is unique to in situ TEM nanoindentation experiments. It allows comparing the plastic flow behavior of single- and bicrystalline compression samples and analyzing the occurring dislocation processes. The use of STEM imaging provides good dislocation contrast while lacking imaging speed. Therefore STEM is useful for e.g. dislocation density analyses, whereas TEM imaging grants higher frame rates at the cost of a greater influence due to bend contours, making it more suitable for the observation of dynamic processes such as dislocation source activation. For investigating dislocation-grain boundary interactions, in situ (S)TEM shows a high potential, especially in combination with faster detectors and truly displacement controlled indenter systems.

Acknowledgments

The authors thank Linlin Li, Xianghai An and Zhefeng Zhang of the Shenyang National Laboratory for Materials Science in China for providing the bulk Cu bicrystals.

References for Chapter 4

[1] W.D. Nix. Mechanical properties of thin films. *Metallurgical and Materials Transactions A*, 20(11):2217–2245, 1989.

[2] G. Dehm. Miniaturized single-crystalline fcc metals deformed in tension: New insights in size-dependent plasticity. *Progress in Materials Science*, 54(6):664–688, 2009.

[3] B. Wu, A. Heidelberg, and J.J. Boland. Mechanical properties of ultrahigh-strength gold nanowires. *Nature Materials*, 4(7):525–529, 2005.

[4] B. Yang, C. Motz, W. Grosinger, W. Kammrath, and G. Dehm. Tensile behaviour of micro-sized copper wires studied using a novel fibre tensile module. *International journal of materials research*, 99(7):716–724, 2008.

[5] J.R. Greer, W.C. Oliver, and W.D. Nix. Size dependence of mechanical properties of gold at the micron scale in the absence of strain gradients. *Acta Materialia*, 53(6):1821–1830, 2005.

[6] D. Kiener, W. Grosinger, G. Dehm, and R. Pippan. A further step towards an understanding of size-dependent crystal plasticity: In situ tension experiments of miniaturized single-crystal copper samples. *Acta Materialia*, 56(3):580–592, 2008.

[7] C. Motz, T. Schöberl, and R. Pippan. Mechanical properties of micro-sized copper bending beams machined by the focused ion beam technique. *Acta Materialia*, 53(15):4269–4279, 2005.

[8] M.D. Uchic, D.M. Dimiduk, J.N. Florando, and W.D. Nix. Sample dimensions influence strength and crystal plasticity. *Science*, 305(5686):986, 2004.

[9] H. Bei, S. Shim, G.M. Pharr, and E.P. George. Effects of pre-strain on the compressive stress-strain response of Mo-alloy single-crystal micropillars. *Acta Materialia*, 56(17):4762–4770, 2008.

[10] S.I. Rao, D.M. Dimiduk, M. Tang, T.A. Parthasarathy, M.D. Uchic, and C. Woodward. Estimating the strength of single-ended dislocation sources in micron-sized single crystals. *Philosophical Magazine*, 87(30):4777–4794, 2007.

[11] T.A. Parthasarathy, S.I. Rao, D.M. Dimiduk, M.D. Uchic, and D.R. Trinkle. Contribution to size effect of yield strength from the stochastics of dislocation source lengths in finite samples. *Scripta Materialia*, 56(4):313–316, 2007.

[12] J.R. Greer and W.D. Nix. Nanoscale gold pillars strengthened through dislocation starvation. *Physical Review B*, 73(24):245410, 2006.

[13] H. Wilsdorf. A Study of Dislocations in Thin Aluminum Foils Elongated in the Electron Microscope. In *Symposium on Advances in Electron Microscopy, ASTM STP*, page 43, 1958.

[14] Z. Shen, R.H. Wagoner, and W.A.T. Clark. Dislocation and grain boundary interactions in metals. *Acta Metallurgica*, 36(12):3231–3242, 1988.

[15] A. Couret, J. Crestou, S. Farenc, G. Molenat, N. Clement, A. Coujou, and D. Caillard. In situ deformation in T.E.M.: recent developments. *Microscopy Microanalysis Microstructures*, 4(2-3):153–170, 1993.

[16] M. Legros. In situ mechanical TEM: Seeing and measuring under stress with electrons. *Comptes Rendus Physique*, 15(2):224–240, 2014.

[17] G. Dehm, T.J. Balk, H. Edongué, and E. Arzt. Small-scale plasticity in thin Cu and Al films. *Microelectronic Engineering*, 70(2-4):412–424, 2003.

[18] B.J. Inkson, G. Dehm, and T. Wagner. In situ TEM observation of dislocation motion in thermally strained Al nanowires. *Acta Materialia*, 50(20):5033–5047, 2002.

[19] M. Haque and M. Saif. In situ tensile testing of nanoscale freestanding thin films inside a transmission electron microscope. *Journal of Materials Research*, 20(07):1769–1777, 2005.

[20] H.D. Espinosa, Y. Zhu, and N. Moldovan. Design and Operation of a MEMS-Based Material Testing System for Nanomechanical Characterization. *Microelectromechanical Systems, Journal of*, 16(5):1219–1231, 2007.

[21] Y. Lu, Y. Ganesan, and J. Lou. A Multi-step Method for In Situ Mechanical Characterization of 1-D Nanostructures Using a Novel Micromechanical Device. *Experimental Mechanics*, 50(1):47–54, 2010.

[22] H. Guo, K. Chen, Y. Oh, K. Wang, C. Dejoie, S.A. Syed Asif, O.L. Warren, Z.W. Shan, J. Wu, and A.M. Minor. Mechanics and Dynamics of the Strain-Induced M1-M2 Structural Phase Transition in Individual VO2 Nanowires. *Nano letters*, 11(8):3207–3213, 2011.

[23] O.L. Warren, Z. Shan, S.A.S. Asif, E.A. Stach, J.W. Morris Jr, and A.M. Minor. In situ nanoindentation in the TEM. *Materials Today*, 10(4):59–60, 2007.

[24] Z. Shan, R.K. Mishra, S.A.S. Asif, O.L. Warren, and A.M. Minor. Mechanical annealing and source-limited deformation in submicrometre-diameter Ni crystals. *Nature Materials*, 7(2):115–119, 2007.

[25] D. Kiener and A.M. Minor. Source-controlled yield and hardening of Cu(100) studied by in situ transmission electron microscopy. *Acta Materialia*, 59(4):1328–1337, 2011.

[26] D. Kiener, P. Kaufmann, and A.M. Minor. Strength, Hardening, and Failure Observed by In Situ TEM Tensile Testing. *Advanced Engineering Materials*, 14(11):960–967, 2012.

[27] D. Kiener and A. Minor. Source truncation and exhaustion: insights from quantitative in situ TEM tensile testing. *Nano letters*, 11(9):3816–3820, 2011.

[28] C. Chisholm, H. Bei, M.B. Lowry, J. Oh, S.A. Syed Asif, O.L. Warren, Z.W. Shan, E.P. George, and A.M. Minor. Dislocation starvation and exhaustion hardening in Mo alloy nanofibers. *Acta Materialia*, 60(5):2258–2264, 2012.

[29] G. Dehm, J.M. Howe, and J. Zweck. *In-situ Electron Microscopy: Applications in Physics, Chemistry and Materials Science*. John Wiley & Sons, 2012.

[30] D. Kiener, Z. Zhang, S. Å turm, S. Cazottes, P.J. Imrich, C. Kirchlechner, and G. Dehm. Advanced nanomechanics in the TEM: effects of thermal annealing on FIB prepared Cu samples. *Philosophical Magazine*, 92(25-27):3269–3289, 2012.

[31] O. Kraft, P.A. Gruber, R. Mönig, and D. Weygand. Plasticity in confined dimensions. *Annual Review of Materials Research*, 40:293–317, 2010.

[32] M.B. Lowry, D. Kiener, M.M. LeBlanc, C. Chisholm, J.N. Florando, J.W. Morris Jr, and A.M. Minor. Achieving the ideal strength in annealed molybdenum nanopillars. *Acta Materialia*, 58(15):5160–5167, 2010.

[33] C. Kirchlechner, J. Keckes, C. Motz, W. Grosinger, M.W. Kapp, J.S. Micha, O. Ulrich, and G. Dehm. Impact of instrumental constraints and imperfections on the dislocation structure in micron-sized Cu compression pillars. *Acta Materialia*, 59(14):5618–5626, 2011.

[34] P.A. Shade, R. Wheeler, Y.S. Choi, M.D. Uchic, D.M. Dimiduk, and H.L. Fraser. A combined experimental and simulation study to examine lateral constraint effects on microcompression of single-slip oriented single crystals. *Acta Materialia*, 57(15):4580–4587, 2009.

[35] M. Schamel. *The influence of interfaces on small-scale mechanical behavior: From fcc metals to polymer/ceramic composites*. PhD thesis, ETH Zurich, 2014.

[36] D. Raabe, D. Ma, and F. Roters. Effects of initial orientation, sample geometry and friction on anisotropy and crystallographic orientation changes in single crystal microcompression deformation: A crystal plasticity finite element study. *Acta Materialia*, 55(13):4567–4583, 2007.

[37] B. Daum, G. Dehm, H. Clemens, M. Rester, F.D. Fischer, and F.G. Rammerstorfer. Elastoplastic buckling as source of misinterpretation of micropillar tests. *Acta Materialia*, 61(13):4996–5007, 2013.

[38] H. Zhang, B.E. Schuster, Q. Wei, and K.T. Ramesh. The design of accurate micro-compression experiments. *Scripta Materialia*, 54(2):181–186, 2006.

[39] P.J. Imrich, C. Kirchlechner, C. Motz, and G. Dehm. Differences in deformation behavior of bicrystalline Cu micropillars containing a twin boundary or a large-angle grain boundary. *Acta Materialia*, 73(0):240–250, 2014.

[40] P.J. Imrich, C. Kirchlechner, D. Kiener, and G. Dehm. Internal and external stresses: In situ TEM compression of Cu bicrystals containing a twin boundary. *Scripta Materialia*, 100(0):94–97, 2015.

[41] D. Gianola and C. Eberl. Micro-and nanoscale tensile testing of materials. *Journal of the Minerals, Metals and Materials Society*, 61(3):24–35, 2009.

[42] F. Di Gioacchino and W.J. Clegg. Mapping deformation in small-scale testing. *Acta Materialia*, 78(0):103–113, 2014.

[43] P. Gumbsch. Dislocations Faster than the Speed of Sound. *Science*, 283(5404):965–968, 1999.

[44] E.A. Stach, D. Zakharov, R.D. Rivas, P. Longo, M. Lent, A. Gubbens, and C. Czarnik. Exploiting a direct detection camera for in-situ microscopy. *Microscopy and Microanalysis*, 19(S2):392–393, 2013.

[45] H.-G. Liao, D. Zherebetskyy, H. Xin, C. Czarnik, P. Ercius, H. Elmlund, M. Pan, L.-W. Wang, and H. Zheng. Facet development during platinum nanocube growth. *Science*, 345(6199):916–919, 2014.

[46] A. Dubach, R. Raghavan, J.F. Löffler, J. Michler, and U. Ramamurty. Micropillar compression studies on a bulk metallic glass in different structural states. *Scripta Materialia*, 60(7):567–570, 2009.

[47] I.N. Sneddon. The relation between load and penetration in the axisymmetric Boussinesq problem for a punch of arbitrary profile. *International Journal of Engineering Science*, 3(1):47–57, 1965.

[48] C. Motz, D. Weygand, J. Senger, and P. Gumbsch. Micro-bending tests: A comparison between three-dimensional discrete dislocation dynamics simulations and experiments. *Acta Materialia*, 56(9):1942–1955, 2008.

[49] C. Kirchlechner, W. Grosinger, M. Kapp, P. Imrich, J.-S. Micha, O. Ulrich, J. Keckes, G. Dehm, and C. Motz. Investigation of reversible plasticity in a micron-sized, single crystalline copper bending beam by X-ray $\hat{\mathrm{I}}\frac{1}{4}$ Laue diffraction. *Philosophical Magazine*, 92(25-27):3231–3242, 2012.

[50] M.W. Kapp, C. Kirchlechner, R. Pippan, and G. Dehm. Importance of dislocations pile-ups on the mechanical properties and the Bauschinger effect in micro cantilevers. *Journal of Materials Research*, 2015.

[51] F. Mompiou, D. Caillard, M. Legros, and H. Mughrabi. In situ TEM observations of reverse dislocation motion upon unloading in tensile-deformed UFG aluminium. *Acta Materialia*, 60(8):3402–3414, 2012.

[52] J. Rajagopalan, J.H. Han, and M.T.A. Saif. Bauschinger effect in unpassivated freestanding nanoscale metal films. *Scripta Materialia*, 59(7):734–737, 2008.

[53] G. Moser, H. Felber, B. Rashkova, P.J. Imrich, C. Kirchlechner, W. Grosinger, C. Motz, G. Dehm, and D. Kiener. Sample Preparation by Metallography and Focused Ion Beam for Nanomechanical Testing. *Practical Metallography*, 49(6):343–355, 2012.

[54] S. Kondo, N. Shibata, T. Mitsuma, E. Tochigi, and Y. Ikuhara. Dynamic observations of dislocation behavior in SrTiO3 by in situ nanoindentation in a transmission electron microscope. *Applied physics letters*, 100(18):181906, 2012.

[55] S. Lee, J. Im, Y. Yoo, E. Bitzek, D. Kiener, G. Richter, B. Kim, and S.H. Oh. Reversible cyclic deformation mechanism of gold nanowires by twinning-detwinning transition evidenced from in situ TEM. *Nat Commun*, 5, 2014.

5

Internal and external stresses: In situ TEM compression of Cu bicrystals containing a twin boundary

Peter J. Imrich[a], Christoph Kirchlechner[b,c], Daniel Kiener[b], Gerhard Dehm[c]

[a]Erich Schmid Institute of Materials Science, Austrian Academy of Sciences, Leoben, Austria

[b]Department of Materials Physics, Montanuniversität Leoben, Austria

[c]Max-Planck-Institut für Eisenforschung, Düsseldorf, Germany

5. Internal and external stresses: In situ TEM compression of Cu bicrystals containing a twin boundary

Numerous micromechanical experiments have shown that metallic samples below tens of micrometers in diameter exhibit a mechanical size effect that is characterized by more stochastic flow, an increased yield strength and stronger scatter in yield strength with decreasing sample diameter. This is explained by the reduced number of dislocation sources[1], dislocation exhaustion[2], source truncation[3] and dislocation starvation[4]. For gaining further insights, in situ transmission electron microscopy (TEM) deformation proved to be a powerful tool, since it allows the analysis of dislocation interaction mechanisms and dislocation density evolution. Conventional deformation experiments in the TEM are based on mechanical straining[5,6] or heating[7,8] of macroscopic samples locally thinned to electron transparency and feature no fully quantitative stress or strain measurement. However, dislocations that bow out under stress can be used as probes for evaluating the local internal stresses acting on the dislocations[2,9]. On the other hand, the introduction of modern indenter systems that are incorporated into the TEM permits the direct measurement of the global force and displacement when deforming miniaturized mechanical samples[10]. With the use of such instruments interesting experimental insights into the mechanical behavior of miniaturized samples could be given, e. g.: dislocation starvation by mechanical annealing in Ni[11], yield strength and hardening behavior in Cu controlled by dislocation source availability[12], extended homogenous deformation in multi-slip oriented samples with dislocation densities in the order of 5 to $50\times10^{13}\,\mathrm{m}^{-2}$ in Cu[13] and deformation behavior determined by dislocation density in Mo fibers[14]. The force and displacement measurement that was applied in the mentioned studies was essential to gain quantitative stress information, but was never combined with dislocation source and curvature analysis to gain in addition information on the local internal stresses. The aim of this study is to combine both measurements for a Cu bicrystal with a coherent twin boundary to see if they are in agreement and follow model predictions[3]. Furthermore, the dislocation density evolution will be mapped up to 20 % strain.

Multiple $40 \times 20 \times 4\,\mu\mathrm{m}^3$ sized lamellae were lifted out of a Cu bicrystal that was grown by the Bridgman method from OFHC copper with 99.999 % purity and contained a single coherent twin boundary. Electron transparent taperless compression samples with a nominal size of either $400 \times 400 \times 200\,\mathrm{nm}^3$ or $650 \times 650 \times 200\,\mathrm{nm}^3$ leading to aspect ratios of 2:1 or 3.3:1, respectively, were cut using a Zeiss Auriga dual beam focused ion beam (FIB) workstation with currents reaching from 120 pA down to 20 pA. The bicrystalline compression pillar contained a coherent twin boundary that spanned from top to bottom of the sample parallel to the $[\bar{1}10]$ compression direction, but inclined to the electron beam to ensure that the boundary region can

be observed during the in situ experiment. The width of the samples was deliberately similar to the length to provide a larger observation area and more room for dislocation movement before interaction with the boundary, while it is known that the shortest dimension, i. e. the thickness, will govern the sample strength[15]. Out of the 12 lift out lamellae 2 lead to successful experiments which are presented here. Each of the lamellae contained one bicrystalline and several single crystalline compression pillars. To reduce the amount of surface damage induced by the Ga^+ milling[16] the samples were heated in situ in the TEM to 480 °C for 25 min at 2×10^{-7} mbar with a Gatan heating holder[17]. Compression experiments were performed using the displacement controlled mode (78 kHz feedback loop) of a Hysitron PI 95 PicoIndenter® inside a Jeol 2100F TEM operated at 200 kV. All samples were loaded with 1 nm/s, leading to a strain rate of $\sim 2 \times 10^{-3}\,s^{-1}$ and observed in either TEM or scanning transmission electron microscopy (STEM) mode with a frame rate of 8 fps or 0.7 fps (full STEM frames), respectively. The force displacement data was recorded at 200 points per second and plotted utilizing a sliding average filter using seven measurements per plotted point. The dislocation density evolution was evaluated with a line intersection method using the same (200) or (220) two-beam condition for the left grain and the bicrystals containing a coherent twin boundary (hereafter labeled as twinned bicrystal) or the right grain, respectively. The error bar represents the number of uncertain intersection points.

Figure 5.1 shows representative stress-strain curves of two single crystals and one twinned bicrystal that is comprised of the two single crystal orientations. Upon loading plastic flow shows strong scatter for the single crystals as well as the twinned bicrystal and occurs in a range from 400 MPa to 950 MPa engineering stress. The stress-strain curve exhibits a serrated flow which is typical for samples of this size and arises from the dislocation source controlled deformation[18]. During unloading tensile stresses occur due to adhesion between the pillar top and the flat punch. No significant difference can be discerned between the stress-strain curves of the single- and bicrystals, which means that for this orientation the twin boundary does not pose a strong barrier for the dislocation movement at the applied stresses or at least counteracts the strengthening by other effects (e. g., by acting as a dislocation source).

The $[\bar{1}10]$ compression direction that was used for the experiments presented here, features four slip systems with the highest Schmid factor of 0.41, two of which have Burgers vectors parallel to the boundary that are shared in both grains. Full screw dislocations in these systems should be able to cross-slip from one grain to the other as suggested in and calculated in[19,20]. For a thorough explanation of this mechanism we refer to recently performed compression experiments on larger micron-sized samples

Figure 5.1.: Engineering stress–strain curves of the single crystalline and twinned bicrystalline compression samples. Only one curve for each representative single crystal orientation and the twinned bicrystal is shown for clarity. Black, gray: single crystals, green: bicrystal, arrow: selected strain burst.

of the same material and compression direction[21]. In the in situ TEM experiments presented here multiple dislocations that exited the boundary on the main slip system were observed (see Supplementary material video 5.1 and Fig. S5.1). However, it was not possible to trace the full movement of dislocations from one grain to the other, thus making it impossible to distinguish whether dislocations penetrated the boundary by cross-slip or were nucleated at it. For an impenetrable boundary such as a high angle grain boundary that is not oriented for easy slip transfer dislocation pile-up would be expected consequently leading to stress concentrations and a change in stress-strain behavior[21]. Yet, this was never observed in the present in situ TEM experiments.

The arrow in Fig. 5.1 shows a strong strain burst that is followed by a load drop, which should not happen in a perfectly displacement controlled experiment. This effect is common[4,11–14,22] and arises due to the insufficient control rate of the indenter system. While it complicates the observation of dislocation source activation in the in situ videos, the stress and strain measurements are not affected except during strain bursts. Another deviation from an ideal compression test is the low apparent elastic modulus, which is frequently observed in micromechanical tests[22–24]. The distorted strain measurement due to system compliance and the influence of plastic deformation

of the sample base was corrected by adding a second strain axis in Fig. 5.1 using in situ images for displacement measurement.

Table 5.1.: Correlation of stresses from the indenter force measurement and stresses calculated from dislocation source activation events or dislocation curvature analysis by in situ TEM in the twinned bicrystals.

In situ video: Internal stress measurement		External stress measurement	Ratio internal stress to external stress
Measured source size or fitted curvature* [nm]	Calculated activation stress [MPa]	$\tau = \sigma \cdot m$ [MPa]	
141 ± 14.1	99 ± 9.9	74 ± 8.8	1.34
75 ± 9.4	167 ± 21.0	122 ± 11.7	1.37
62 ± 8.5*	195 ± 26.8	251 ± 19.5	0.78
109 ± 11.8	123 ± 13.3	198 ± 16.3	0.62
109 ± 11.8	123 ± 13.3	125 ± 11.9	0.98

As mentioned earlier, previous studies have either calculated the stresses acting inside the sample by analyzing the dislocation curvature[8,9,25,26] or taken the force measurement from the indenter system to evaluate the stresses imposed on the sample[11–13,17,22]. The combination of both techniques, however, allows verifying whether the internal stresses acting locally on the dislocations inside the sample actually correspond to the externally applied stresses from the indenter. The shear stress τ acting on a dislocation source is given according to Rao et al.[2] by:

$$\tau(L) = kG\frac{\ln(L/b)}{L/b} \tag{5.1}$$

with k being a constant between 0.06 and 0.18 depending on the source type, G the shear modulus, L the source length or twice the radius of curvature and b the Burgers vector. Heat-treating the samples as proposed by Kiener et al.[17] is seen as necessary for monitoring dislocations in FIB-prepared Cu samples and lead to materials behavior that is not influenced by the FIB preparation route. Furthermore, the knowledge of crystal orientation and acting slip planes is essential to accurately measure the dislocation source length or the dislocation curvature. It must be noted that the measured stress will deviate if the dislocation is not isolated but piles up at a boundary or interacts with other dislocations. Table 5.1 shows that the calculated values from the TEM images correspond well with the shear stresses calculated from the force measurement. This proves that the evaluation of stresses using the dislocation curvature method is valid even in micromechanical samples if the test is carefully conducted.

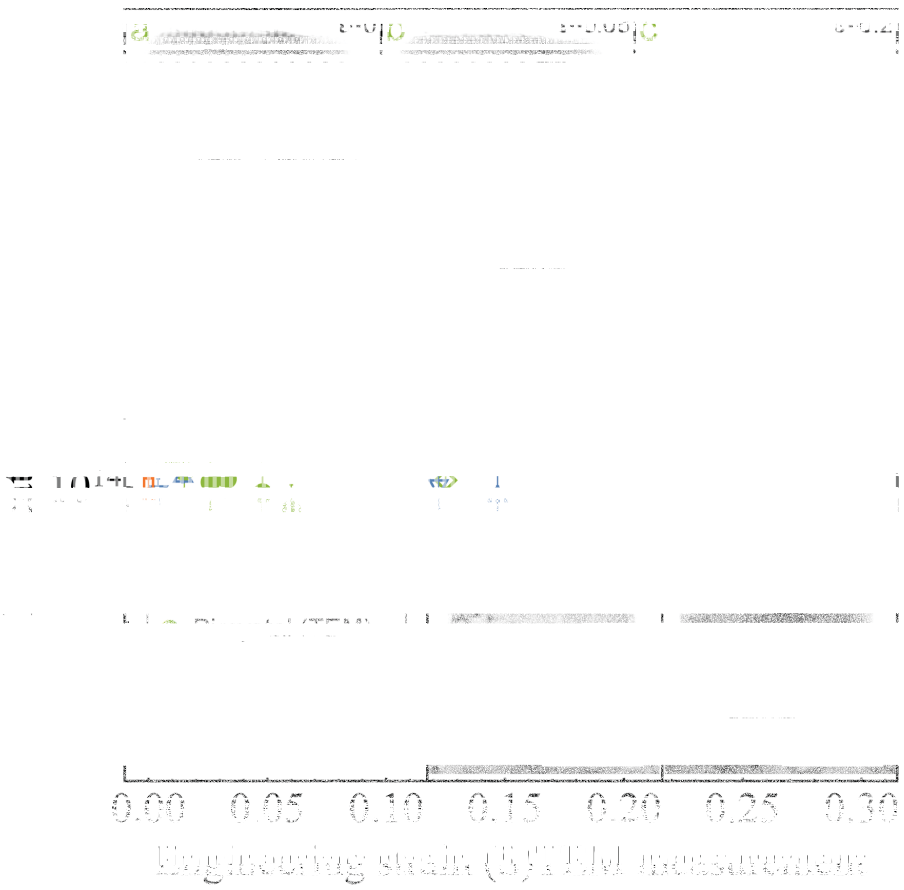

Figure 5.2.: Evolution of the dislocation density during subsequent deformation steps for the twinned bicrystals and the single crystals. Insets: STEM images of the twinned bicrystal (a) before testing, (b) after the fourth and (c) after the sixth deformation step and STEM images of the single crystal of (d) the left and (e) the right grain at certain strain values ϵ.

Figure 5.3 a–c depicts a dislocation that was nucleated near the sample-flat punch interface and cross-slipped onto the main slip system after having traveled approximately halfway along the length of the pillar (see Supplementary material video 5.2). The dislocation first moved on the green slip plane in Fig. 5.3 c, which should not experience high shear stresses since it is nearly parallel to the compression direction. In this case the internal and external stresses were not the same locally because of the imperfect loading (local indentation due to surface roughness), but in the middle of the sample the global stress dominated over the local stress, which leads to cross-slip of the dislocation. An evaluation of the shear stress at this stage (Fig. 5.3 b) yields 195 ± 26.8 MPa and 251 ± 19.5 MPa for analysis via dislocation radius and indenter force measurement, respectively, again showing agreement.

It has to be mentioned that nearly all dislocation source activation events that were reported occurred during loading of the sample before significant plastic strain. Bow-out of these dislocations and the subsequent source activation could only be observed once; later on, stable sources which produced many dislocations after formation lead to strain bursts with dislocation speeds that could not be resolved at the used frame rate.

For both bicrystals and two single crystals of each orientation, the dislocation density was evaluated between the deformation steps to monitor the dislocation density evolution. As depicted in Fig. 5.2, the two bicrystals show a distinctly different behavior. The dislocation density of one bicrystal decreases steadily during deformation but maintains a high level of $\sim 10^{14}\,\mathrm{m}^{-2}$ throughout the whole experiment. The other shows a different evolution by dropping by a factor of ~ 4 during the first deformation step and in the end increasing by a factor of ~ 3 compared to the initial value. For the single crystals, the left orientation exhibits lower dislocation densities than samples in the right grain. In none of the experiments a total dislocation starved state is reached through mechanical annealing as proposed for small enough samples[4,11,14]. This agrees with in situ TEM experiments performed on Al and Cu[22] tensile samples and pre-strained Ni compression pillars[27]. Analyses of the in situ videos show an increase in dislocation density during deformation and a decrease during unloading, especially in the tensile regime (due to adhesion between the pillar surface and the flat punch). This suggests that even at the lowest dislocation density of $3.7 \times 10^{13} \pm 3.1 \times 10^{12}\,\mathrm{m}^{-2}$, which corresponds to a total dislocation line length of $\sim 1.2\,\mu\mathrm{m}$ in a $0.4 \times 0.4 \times 0.2\,\mu\mathrm{m}^3$ pillar, a sufficient number of dislocations remain in the sample to allow for dislocation-dislocation interactions and dislocation multiplication.

For small enough grains in polycrystalline materials, it was found that the dislocation character changes from full to partial dislocations. In situ experiments on single crystalline Cu wires showed a sharp transition from full to partial dislocation mediated plasticity at a thickness of 150 nm, with the first contribution of partials below $\sim 200\,\mathrm{nm}$. For the in situ experiments presented here, most of the deformation was governed by full dislocations in the 200 nm thick samples, but the movement of partial dislocations was observed at times. Most partial dislocation activity was found in single crystalline samples of the left component orientation as depicted in Fig. 5.3 d; especially between strains of 0.05 and 0.1 where low dislocation densities were measured. For these samples the slip planes with the highest Schmid factor intersect the sample surface perpendicular to the compression direction (see Supplementary material Fig. S5.1), which seems to make them more prone to dislocation

Figure 5.3.: (a–c) STEM images of the twinned bicrystalline sample with a cross-slip event from a slip system with low Schmid factor (green) to one with high Schmid factor (red). The arrows point at the cross-slipping dislocation. (d) Single crystalline sample of the left grain shows the movement of a partial dislocation (arrow), which leaves behind a stacking fault.

starvation. Note that the intersection lines of slip planes and sample surfaces seem asymmetric due to the inclination of the twin boundary; even though perfect symmetry exists (see Supplementary material video 5.3). It is interesting that the loss in dislocation density and the need for partial dislocation nucleation from the surface are not strongly reflected in the flow stress of the pillars. Twinned bicrystals much smaller than 200 nm in thickness might show a change in deformation mechanism since single partial dislocations cannot cross-slip at the twin boundary and more complicated interactions could be expected.

Results presented here show that it is possible to visualize dislocation source activation processes and use dislocation curvature to calculate stresses even in miniaturized FIB-prepared samples. The unwanted contrast from FIB-induced surface damage can

be effectively reduced by heat and the additional use of an indenter system proves that the internally measured stresses match the externally applied loads even in this size regime. The bicrystals with a coherent twin boundary along the compression direction exhibit the same stress-strain signatures as their single crystalline counterparts without any signs of strengthening or creation of a local stress concentration. This means that at this orientation the twin boundary does not pose a significant barrier to dislocation movement, or at least counteracts the strengthening effects of the boundary by acting as a dislocation source with nucleation stresses comparable to external stress levels. The dislocation density evolution during deformation of the pillars tested in this study shows some difference; yet, the dislocation density remains high enough ($\geq 3\times10^{13}\,\mathrm{m}^{-2}$) in all samples to lead to dislocation multiplication without significantly altering the flow stress of the sample.

Acknowledgments

The authors thank LL Li, XH An and ZF Zhang of the Shenyang National Laboratory for Materials Science in China for providing the bulk Cu bicrystals. J Kreith of the Montanuniversität Leoben in Austria is acknowledged for the help with crystal orientations and coordinate transformations.

Supplementary Material

The supplementary videos are included digitally on the storage medium located at the end of this thesis.

Suppl. Figure S 5.1: Schematics of the slip planes with highest Schmid factor in the twinned bicrystalline sample. The striped gray plane represents the twin boundary and the dotted and full black line the dislocations that move from the boundary into the left grain.

References for Chapter 5

[1] H. Bei, S. Shim, G.M. Pharr, and E.P. George. Effects of pre-strain on the compressive stress-strain response of Mo-alloy single-crystal micropillars. *Acta Materialia*, 56(17):4762–4770, 2008.

[2] S.I. Rao, D.M. Dimiduk, M. Tang, T.A. Parthasarathy, M.D. Uchic, and C. Woodward. Estimating the strength of single-ended dislocation sources in micron-sized single crystals. *Philosophical Magazine*, 87(30):4777–4794, 2007.

[3] T.A. Parthasarathy, S.I. Rao, D.M. Dimiduk, M.D. Uchic, and D.R. Trinkle. Contribution to size effect of yield strength from the stochastics of dislocation source lengths in finite samples. *Scripta Materialia*, 56(4):313–316, 2007.

[4] J.R. Greer and W.D. Nix. Nanoscale gold pillars strengthened through dislocation starvation. *Physical Review B*, 73(24):245410, 2006.

[5] Z. Shen, R.H. Wagoner, and W.A.T. Clark. Dislocation and grain boundary interactions in metals. *Acta Metallurgica*, 36(12):3231–3242, 1988.

[6] P. Castany and M. Legros. Preparation of H-bar cross-sectional specimen for in situ TEM straining experiments: A FIB-based method applied to a nitrided Ti-6Al-4V alloy. *Materials Science and Engineering: A*, 528(3):1367–1371, 2011.

[7] G. Dehm, T.J. Balk, H. Edongué, and E. Arzt. Small-scale plasticity in thin Cu and Al films. *Microelectronic Engineering*, 70(2-4):412–424, 2003.

[8] T.J. Balk, G. Dehm, and E. Arzt. Parallel glide: unexpected dislocation motion parallel to the substrate in ultrathin copper films. *Acta Materialia*, 51(15):4471–4485, 2003.

[9] A. Couret, J. Crestou, S. Farenc, G. Molenat, N. Clement, A. Coujou, and D. Caillard. In situ deformation in T.E.M.: recent developments. *Microscopy Microanalysis Microstructures*, 4(2-3):153–170, 1993.

[10] O.L. Warren, Z. Shan, S.A.S. Asif, E.A. Stach, J.W. Morris Jr, and A.M. Minor. In situ nanoindentation in the TEM. *Materials Today*, 10(4):59–60, 2007.

[11] Z. Shan, R.K. Mishra, S.A.S. Asif, O.L. Warren, and A.M. Minor. Mechanical annealing and source-limited deformation in submicrometre-diameter Ni crystals. *Nature Materials*, 7(2):115–119, 2007.

[12] D. Kiener and A.M. Minor. Source-controlled yield and hardening of Cu(100) studied by in situ transmission electron microscopy. *Acta Materialia*, 59(4):1328–1337, 2011.

[13] D. Kiener, P. Kaufmann, and A.M. Minor. Strength, Hardening, and Failure Observed by In Situ TEM Tensile Testing. *Advanced Engineering Materials*, 14(11):960–967, 2012.

[14] C. Chisholm, H. Bei, M.B. Lowry, J. Oh, S.A. Syed Asif, O.L. Warren, Z.W. Shan, E.P. George, and A.M. Minor. Dislocation starvation and exhaustion hardening in Mo alloy nanofibers. *Acta Materialia*, 60(5):2258–2264, 2012.

[15] N.M. Jennett, R. Ghisleni, and J. Michler. Enhanced yield strength of materials: The thinness effect. *Applied physics letters*, 95(12):–, 2009.

[16] D. Kiener, C. Motz, M. Rester, M. Jenko, and G. Dehm. FIB damage of Cu and possible consequences for miniaturized mechanical tests. *Materials Science and Engineering: A*, 459(1-2):262–272, 2007.

[17] D. Kiener, Z. Zhang, S. Å turm, S. Cazottes, P.J. Imrich, C. Kirchlechner, and G. Dehm. Advanced nanomechanics in the TEM: effects of thermal annealing on FIB prepared Cu samples. *Philosophical Magazine*, 92(25-27):3269–3289, 2012.

[18] M.D. Uchic, P.A. Shade, and D.M. Dimiduk. Plasticity of micrometer-scale single crystals in compression. *Annual Review of Materials Research*, 39:361–386, 2009.

[19] M. Chassagne, M. Legros, and D. Rodney. Atomic-scale simulation of screw dislocation/coherent twin boundary interaction in Al, Au, Cu and Ni. *Acta Materialia*, 59(4):1456–1463, 2011.

[20] Z.H. Jin, P. Gumbsch, E. Ma, K. Albe, K. Lu, H. Hahn, and H. Gleiter. The interaction mechanism of screw dislocations with coherent twin boundaries in different face-centred cubic metals. *Scripta Materialia*, 54(6):1163–1168, 2006.

[21] P.J. Imrich, C. Kirchlechner, C. Motz, and G. Dehm. Differences in deformation behavior of bicrystalline Cu micropillars containing a twin boundary or a large-angle grain boundary. *Acta Materialia*, 73(0):240–250, 2014.

[22] D. Kiener and A. Minor. Source truncation and exhaustion: insights from quantitative in situ TEM tensile testing. *Nano letters*, 11(9):3816–3820, 2011.

[23] H. Zhang, B.E. Schuster, Q. Wei, and K.T. Ramesh. The design of accurate micro-compression experiments. *Scripta Materialia*, 54(2):181–186, 2006.

[24] A. Dubach, R. Raghavan, J.F. Löffler, J. Michler, and U. Ramamurty. Micropillar compression studies on a bulk metallic glass in different structural states. *Scripta Materialia*, 60(7):567–570, 2009.

[25] F. Mompiou, D. Caillard, M. Legros, and H. Mughrabi. In situ TEM observations of reverse dislocation motion upon unloading in tensile-deformed UFG aluminium. *Acta Materialia*, 60(8):3402–3414, 2012.

[26] M. Legros. In situ mechanical TEM: Seeing and measuring under stress with electrons. *Comptes Rendus Physique*, 15(2):224–240, 2014.

[27] A.S. Schneider, D. Kiener, C.M. Yakacki, H.J. Maier, P.A. Gruber, N. Tamura, M. Kunz, A.M. Minor, and C.P. Frick. Influence of bulk pre-straining on the size effect in nickel compression pillars. *Materials Science and Engineering: A*, 559(0):147–158, 2013.

6

Influence of inclined twin boundaries on the deformation behavior of Cu micropillars

Peter J. Imrich[a], Christoph Kirchlechner[b,c], Gerhard Dehm[b]

[a]Erich Schmid Institute of Materials Science, Austrian Academy of Sciences, Leoben, Austria

[b]Max-Planck-Institut für Eisenforschung, Düsseldorf, Germany

[c]Department of Materials Physics, Montanuniversität Leoben, Austria

6. Influence of inclined twin boundaries on the deformation behavior of Cu micropillars

Abstract

In situ micromechanical compression tests on Cu pillars were performed to evaluate the influence of twin boundaries on the mechanical behavior. The 1 µm sized Cu samples on a Si substrate prepared by focused ion beam milling were either single crystalline or contained 2–5 twin boundaries that were inclined to the compression direction. The strengths of the pillars vary, depending on the crystal orientation, associated twin boundary inclination and orientation of slip systems. Results show, that multiple slip systems are activated in each pillar. However, slip parallel to the twin boundaries prevails due to the long mean free path for dislocation movement.

6.1. Introduction

Grain boundaries greatly influence the mechanical properties of metals. In the 1950s Hall and Petch[1,2] showed, that the yield strength of metals scales inversely with the square root of the grain size. This is explained by the reduced mean free path and the pile-up of dislocations at boundaries. While the influence of a reduced grain size can easily be described in macroscopic dimensions, the effects of the individual boundaries and the exact interaction processes with dislocations remain fairly unknown. Miniaturized sample testing, which has gained more and more importance since the introduction of focused ion beam (FIB) preparation techniques[3] provides a convenient tool to study such interaction processes. Compression[3,4], tension[5], or bending[6] samples can be prepared at specifically selected boundaries which makes it possible to incorporate a single grain boundary or several boundaries of the same type into one sample. This eliminates the averaging influence of numerous different grain boundaries of bulk mechanical testing.

First experiments on bicrystalline Al micropillars with a vertical high angle grain boundary were performed by Ng et al.[7]. The 6 µm sized bicrystals show increased yield strength, stronger hardening and less serrated deformation behavior compared to the single crystals. This is explained by dislocation pile-up at the boundary and increased dislocation-dislocation interactions. Similar results were presented by Imrich et al.[8] for 7 µm sized Cu bicrystals incorporating an arbitrary high angle grain boundary. Slightly different observations were made by Schamel[9] for Au; while the yield strengths for single- and bicrystals in the compression tests were found to be similar, the Au pillars in the size range of 440 nm–2.7 µm exhibit stronger hardening and a drastic reduction in load drops. Schamel explains this behavior also by a dislocation pile-up at the boundary and suppression of dislocation avalanches. Ex-

periments by Kunz et al.[10] on the other hand show lower hardening and larger strain bursts for 400 nm–2 µm sized Al bicrystals. Based on TEM observations of low dislocation densities near the boundary, they come to the conclusion that low dislocation storage is the reason for the enhanced stochastic behavior. Kheradmand et al.[11–13] propose that the influence of the boundary is important for Ni bicrystals smaller than 1 µm but negligible for larger sized samples where dislocation-dislocation interactions dominate.

Numerous experiments on nanotwinned Cu with twin lamella spacings down several nanometer show very high strength and ductility[14,15], even for micropillars[16,17]. However, Imrich et al.[8] reveal that approx. 4 µm sized Cu bicrystals with a single coherent twin boundary along the compression direction exhibit the same stress-strain behavior as single crystalline samples, due to an easy dislocation transmission process by cross slip. A lack of strengthening was also found for smaller bicrystals with 200 nm thickness tested in the TEM, even if a dislocation transmission mechanism could not be unambiguously identified[18]. The objective of this article is twofold; it aims for at better understanding of the influence of twin boundaries on the mechanical behavior by using Cu microcompression samples containing up to 5 twin boundaries. Additionally, the twin boundary orientation is inclined to the compression direction as opposed to being parallel as in earlier studies.

6.2. Experimental Details

A 3 µm thick Cu film was magnetron sputtered under ultrahigh vacuum conditions on a (001) oriented Si single crystal substrate. The Si substrate had been passivated with a bilayer consisting of 50 nm thick amorphous SiO_x and 50 nm thick amorphous SiN_x to avoid Cu-Si interdiffusion. The film was annealed in the deposition chamber at 600 °C for approx. 10 min to obtain a columnar microstructure with lateral grain sizes of typically 1–2 times the film thickness. The nominally $1 \times 1 \times 3\,\mu m^3$ sized Cu compression samples were milled near the edge of the macrosample to allow for observation in the SEM during deformation using a Leo XB1450 Dual Beam focused ion beam (FIB) workstation. The front and back surfaces were milled from the top (along the compression direction) with an overtilt of $\sim 2°$ to account for the FIB taper and assure parallel sidewalls. Afterwards the side surfaces were cut perpendicular to the compression axis, leading to a slightly trapezoidal (due to FIB taper) but constant cross-section throughout the pillar length. Ion currents reaching from 5 nA to 100 pA were used for course to fine milling, respectively. The pillars were either single crystalline or contained 2–5 twin boundaries all lying parallel to each other on

the same set of {111} planes inclined to the compression axis.

Mechanical testing was performed utilizing a Hysitron PI85 PicoIndenter® in displacement controlled mode with a feedback loop of 78 kHz using a strain rate of $10^{-3}\,s^{-1}$ to deform the pillars while recording force-displacement data. The deformation was carried out in consecutive loading and unloading steps up to a total strain of 7–25% and images were recorded before, during and after deformation. Due to the rigid Si base, deformation is assured to be localized in the Cu pillar itself. For some samples electron backscatter diffraction (EBSD) analyses were conducted before deformation in a LEO 1525 SEM using an EDAX EBSD system. Furthermore, for selected pillars a liftout was performed after deformation and EBSD slices were acquired in a Zeiss Auriga workstation equipped with an EDAX EBSD system.

6.3. Results

The tested samples are split into two types of approximate orientation pairs to ease discussion: Type A: [111]/[115] and type B: [100]/[122], each representing the compression direction of the matrix and the twinned part. Out of the 27 tested samples, 19 experiments were regarded successful and used for the interpretation. The other 8 experiments were rejected due to incorrect alignment or indenter instabilities.

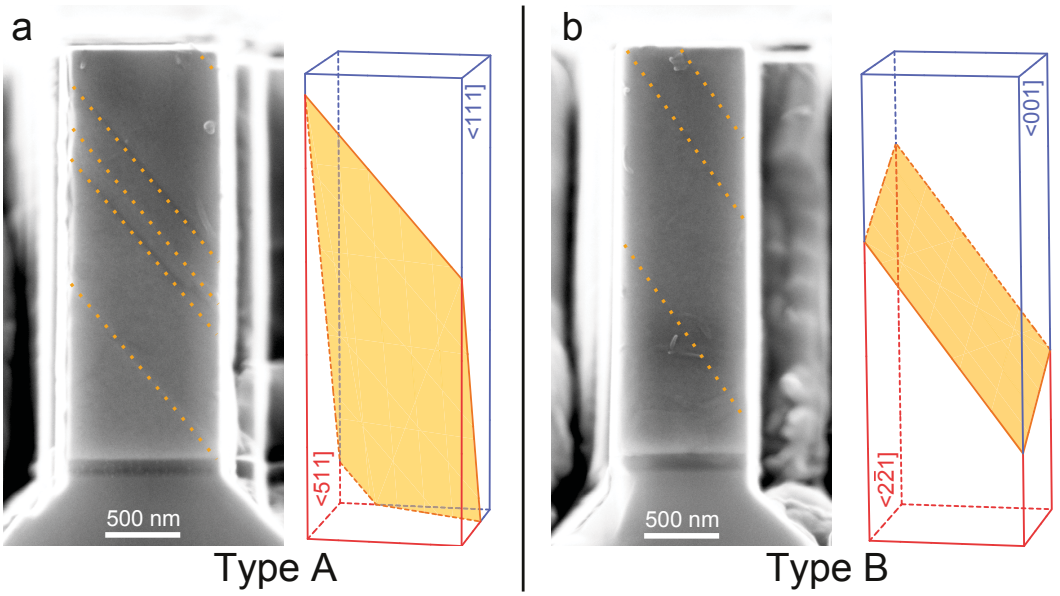

Figure 6.1.: SEM micrographs before deformation for two representative pillars of type A and type B orientation. The twin-surface intersections are indicated with dashed lines. Corresponding schematic drawings show the differing twin boundary orientation (only one boundary plane is indicated for clarity).

Figure 6.1 shows representative samples of type A and type B before compression testing and corresponding schematic drawings of the twin boundary orientation. The intersections of the twin boundaries with the surface are indicated by dashed lines. Only one boundary is depicted in each schematic drawing for increased clarity (the twin boundaries inside the pillars were parallel to each other). Note that the inclination of the boundary strongly differs in type A and B samples. The representative pillars after deformation to 0.13 and 0.12 strain for type A and type B, respectively, are presented in Fig. 6.2, along with orientation imaging microscopy maps (OIMs) of the top surface. The color represents the compression direction measured by electron backscatter diffraction (EBSD). Slight barreling is discernible in the type A sample accompanied with a lack of distinct slip systems. However, localized deformation indicated by an arrow can be seen (Fig. 6.2 a). The type B sample on the other hand exhibits a more distinct slip step (marked by arrow in Fig. 6.2 b) and noticeable lateral displacement.

The stress-strain behavior of all tested samples matches results documented in literature of compression tests in such dimensions, i. e., exhibiting serrated flow with numerous load drops and increased yield strength[3–5,19]. The engineering stress-strain curves for the pillars depicted in the previous figures are shown in Fig. 6.3. All pillar tests were performed in consecutive compression steps to allow for detailed SEM imaging without indenter contact between the steps and to reduce the constraints imposed by the lateral stiffness of the indenter setup[9,20–22]. The tensile stresses during unloading of the pillars are due to adhesion between the Cu surface and the diamond flat punch indenter.

The flow stresses measured at 1, 2, 3, 4 and 5% strain of all successful compression tests are plotted in Fig. 6.4, giving additional information on the strengthening of the micropillars. For each pillar with orientation information the Schmid factors for slip parallel to the twin boundary were evaluated and the highest value was used for the plot, as explained in the discussion section. In the accepted data set, four pillars had exact EBSD information of the compression axis, which are plotted as dark blue squares. For a set of two pillars the orientation was deduced from EBSD slice images acquired after a sample liftout leading to a possible misorientation of up to 10° (light blue diamonds) and the flow stresses of twinned pillars without orientation information are plotted as green stars (separated from the diagram by a dashed line in Fig. 6.4). The pillars on the same macrosample which proved to be single crystalline and either of [111] or close to [100] orientation are included for comparison.

6.4. Discussion

In the following part the flow stresses of type A and type B pillars are related to crystal and twin plane orientation and corresponding Schmid factors. Furthermore, experiments on compression pillars incorporating boundaries are discussed in general.

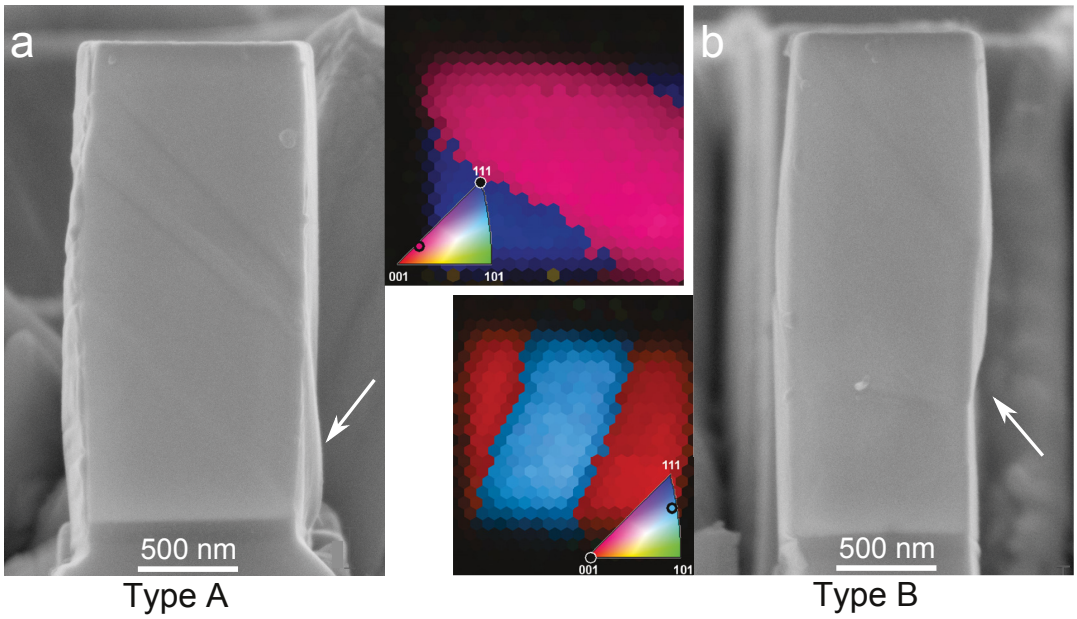

Figure 6.2.: SEM micrographs of two representative pillars after deformation to (a) 0.13 and (b) 0.12 for type A and type B, respectively. The according EBSD images of the top surfaces show the compression direction before deformation. The inverse pole figures indicate the matrix and twin orientations by full and open circles, respectively

6.4.1. Compression testing of Cu micropillars with inclined twin boundaries

The flow stresses of miniaturized Cu samples are dependent on the following parameters: dislocation source size (dependent mainly on pillar size)[23], available slip systems (high Schmid factor systems are preferred) and long mean free path for dislocations (preferably intersecting the side surfaces of the pillar to avoid any pile up)[20]. The longest mean free path for dislocations without interaction with the boundary is parallel to it. Since the twin boundary plane is of (111) type, three such slip systems exist in each grain.

Depending on the inclination of the twin plane, which is dependent on the crystallographic orientation of both grains, two cases are possible: (i) the boundary

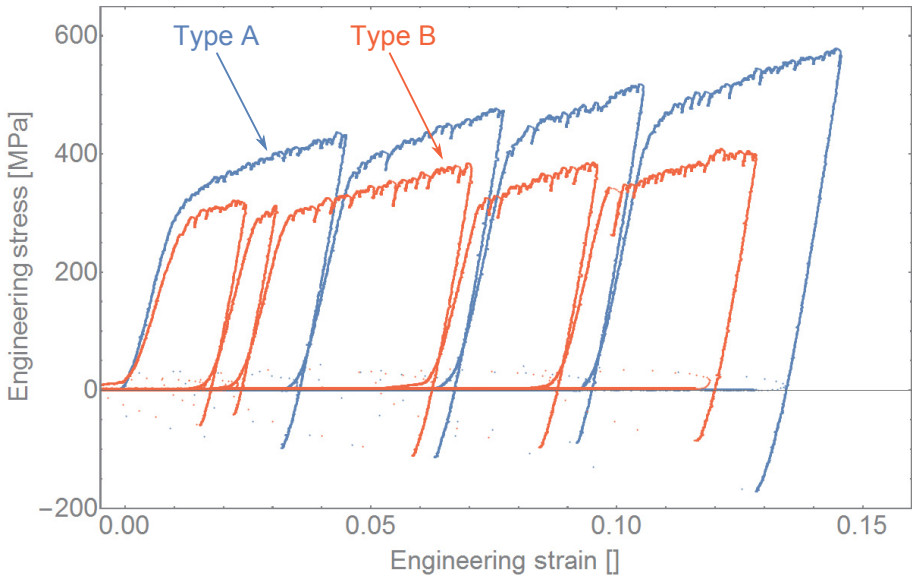

Figure 6.3.: Engineering stress-strain curves of type A and type B pillars depicted in Fig. 6.1 and 6.2. The type A pillar shows increased strength compared to type B and similar stochastic flow.

intersects only the side surfaces of the pillar but not the top surface and the sample base. In this orientation dislocations can slip through the pillar and escape at the free surface. (ii) The twin boundary also intersects the sample base and/or top surface, suppressing dislocation escape and leading to a dislocation pile-up. In case (i) a pillar can deform similarly to a single crystal given that sufficient sources are placed in the region of unhindered slip. In case (ii) a long mean free path for dislocations is provided, however, they will pile up at the pillar base and/or top surface after significant strain.

Dislocations on slip systems which are not parallel to the twin will inevitably interfere with the boundary. The interactions between dislocations and twin boundaries can vary from pile-up[24], to dissociation into the twin[25] or transfer by cross-slip[8,24,26] depending on dislocation type, slip system and twin boundary orientation. Latter is possible for slip systems with Burgers vectors parallel to the twin plane and provides long mean free paths, if the dislocations can traverse through the whole sample and the applied stress is sufficient to overcome the energy barrier for cross-slip. Therefore, slip transmission should also be taken into account when analyzing the slip systems in the tested pillars.

Fig. 6.5 presents schematic drawings of slip systems in simplified bicrystalline pillars with a single boundary located at the center of the sample. Slip systems with high Schmid factor that run either parallel to the boundary or are oriented for easy

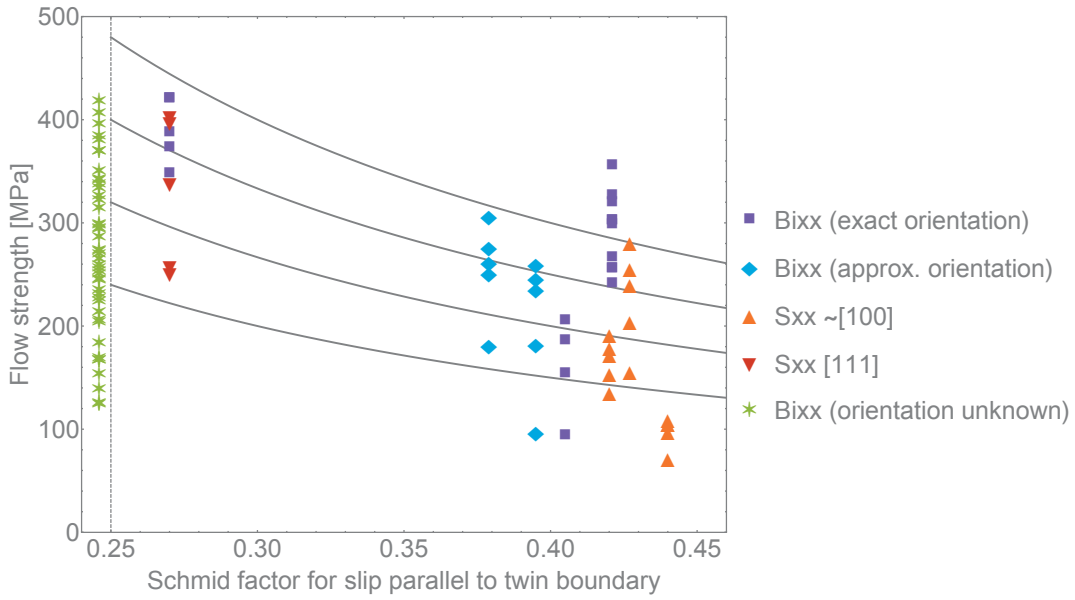

Figure 6.4.: Flow stresses of all successful pillar tests at 1–5% strain plotted over the maximum Schmid factor for slip parallel to the twin boundary. The gray lines represent constant shear stress.

slip transmission are shown in Fig. 6.5 for type A and type B pillars, respectively. Firstly, type B pillars will be discussed: Due to the inclination of the twin boundary, a large volume that allows for unconstrained slip and dislocation escape to the surface is provided (see Fig. 6.5 c). The depicted slip systems in Fig. 6.5 c have the highest Schmid factor, m, of 0.41 which is 78% higher than for the successive slip system in the [122] grain and equal to the others in the [100] grain (for a full list of Schmid factors see Table 6.1). This combination leads to easy deformation, similar to single crystals, if enough dislocation sources are present on these two slip systems. This is reflected in the low flow stresses presented in Fig. 6.4 at $m = 0.41$. Regarding easy slip transfer in type B pillars, one of the two equivalent sets of slip systems is depicted in Fig. 6.5 d. These slip systems have Schmid factors of 0.41 and 0.14 in [100] and [122], respectively. Therefore the probability of slip transfer is low, since dislocations produced in the [100] grain would rather cross-slip within the same grain onto a slip plane parallel to the boundary, which has a high Schmid factor of 0.41, than transferring into the next grain with lower shear stresses. These arguments are supported by the post mortem SEM images, showing that the largest slip step (indicated by arrow in Fig. 6.2 b) is on a slip system parallel to the twin boundaries. For type A pillars the interpretation is more complex. The highest Schmid factors are found in

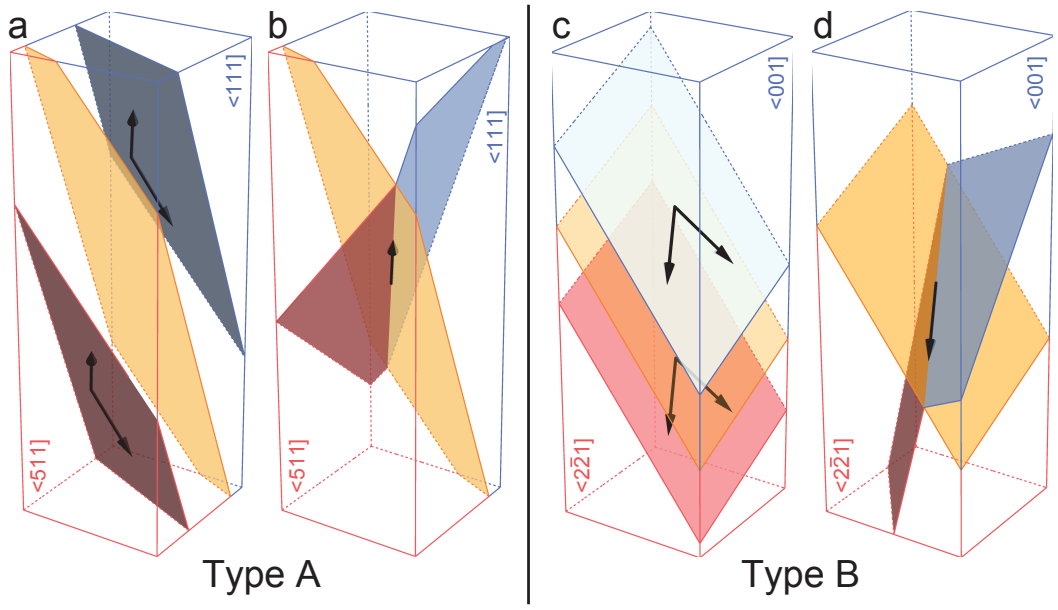

Figure 6.5.: Slip systems in type A pillars (a) parallel to the twin boundary and (b) oriented for easy slip transfer. Slip systems in type B pillars (c) parallel to the twin boundary and (d) oriented for easy slip transfer.

slip systems that are oriented for dislocation transmission by cross slip. Figure 6.5 b shows one such set of slip systems with m = 0.27 and m = 0.45 for [111] and [115], respectively. Since the pillar is comprised of multiple parallel twins, several cross-slip processes are necessary for dislocations to cross the whole pillar. In fcc metals the activation of dislocation sources and not the stress needed for dislocation movement is regarded as decisive for the strength of micropillars (assuming an unobstructed slip path)[23]. Therefore, dislocations produced by sources on high Schmid factor slip systems may also move in systems with low Schmid factor after crossing the boundary. Hence, dislocation source activation in the [115] grain with high Schmid factor would also lead to dislocation movement in the [111] grain. However, the difference in Young's moduli, i. e., 190 GPa for [111] and 77 GPa for [115] should not be disregarded. Due to the large inclination of the twin boundary in type A samples, both grains are not compressed in series, but approach iso-strain conditions which leads to a stress decrease in the softer [115] grain, thus countering the effect of the higher Schmid factor. Additionally, the dislocation source size has to decrease in samples that deform by slip transfer if the twin spacing is smaller than the pillar diameter.

Despite having a lower Schmid factor of 0.27 and intersecting the pillar base and/or pillar top, the slip systems parallel to the twin boundary (Fig. 6.5 a) still provide long mean free paths and the dislocation source size is unaffected by the twin lamella

Table 6.1.: List of Schmid factors for slip systems in type A and type B pillars. *parallel to the twin boundary, †slip transfer by cross-slip

Type A		Type B	
111	115	100	122
0.27*	0.45†	0.41*	0.41*
0.27*	0.45†	0.41*	0.41*
0.27†	0.42	0.41†	0.23
0.27†	0.42	0.41†	0.23
0.27	0.30	0.41	0.18
0.27	0.30	0.41	0.18
0.00	0.27*	0.41	0.14†
0.00	0.27*	0.41	0.14†
0.00	0.15	0.00	0.05
0.00	0.15	0.00	0.05
0.00	0.00	0.00	0.00
0.00	0.00	0.00	0.00

spacing. No large, distinct slip steps can be made out on the sample surface in Fig. 6.2 a; however, localized plasticity parallel to a twin lamella (marked by arrow) suggests dislocation activity on such slip systems. Furthermore, Fig. 6.4 shows that the flow stresses of the twinned pillar conform with the flow stresses of the [111] single crystal (that only features slip systems with $m = 0.27$), showing little influence of the softer slip systems in the [115] grain. Lines of constant shear stress in Fig. 6.4 show a good correspondence for slip parallel to the grain boundary, suggesting that these systems are being favored despite the lower shear stress.

As a result of the multislip orientation (especially [111] and [100] grains), providing up to eight slip systems with highest Schmid factor, an activation of slip systems which are not parallel to the boundary cannot be excluded. The sparsity of large, distinct slip steps on the pillar surfaces and slight barreling hints at considerable amounts of dislocation-dislocation interactions. Dislocation sources on unfavorable slip systems lead to dislocation pile-up at the boundaries and a general rise in the dislocation density. This may be amplified by the high dislocation density of typically 10^{13}–$10^{14}\,\mathrm{m}^{-2}$ reported in literature for Cu films[27,28]. Due to the large mismatch in thermal expansion coefficients between Cu and Si, biaxial tensile stresses in the order of 100–200 MPa develop in the Cu layer during cooling from the annealing temperature to room temperature; the biaxial thermal tensile stresses lead to plastic deformation that is comparable to a uniaxial compression normal to the film surface[29,30]. However, compared to the microcompression experiments there are no free

pillar surfaces, leading to dislocation storage and consequently a higher dislocation density in the Cu film. Nevertheless, the most pronounced and localized deformation is taking place parallel to the boundaries for both samples.

6.4.2. Choosing a boundary orientation for bicrystalline micropillar compression tests

Some grain boundary orientations do not strongly influence the stress-strain behavior of a material, simply because the dislocations do not have to interact with them. This raises the question, how a boundary should be oriented in a pillar compression experiment to gain useful information. Fig. 6.6 shows compression pillars with an aspect ratio of 1:3 and a single centered boundary. In Fig 6.6 a the boundary is oriented normal to the compression direction. In this case, dislocations will interact with it depending on aspect ratio and slip plane orientation. For samples with a sufficiently high aspect ratio, single crystal slip in each grain will be dominant and little influence of the boundary is expected. For short aspect ratios the influence of the boundary will increase, as will the influence due to the constricted volume that is not able to slip without interaction with the sample base or the flat punch[20,31]. Therefore, this orientation is not recommended for testing single grain boundaries. However, it can be used when testing samples with numerous interfaces that are evenly spread across the pillar length, rendering unobstructed slip impossible and requiring dislocation-boundary interactions[16,32].

The orientation depicted in Fig. 6.6 b is similar to Fig. 6.6 a. Deformation for slip systems parallel to the boundary is alleviated while slip systems that meet the boundary at an angle will interfere with it. Depending on the slip systems with high Schmid factor, single crystal like slip or strong interaction with the boundary could be the case. For large aspect ratios, however, the boundary influence will decrease similar to Fig. 6.6 a.

Fig. 6.6 c shows a slanted boundary that intersects the sample top as well as sample base, assuring that no dislocation slip is possible without interaction with the boundary, the sample base or sample top. However, large mean free paths are available for dislocations travelling parallel to the boundary in either grain. For substantial deformation an interaction with the boundary is expected. A factor that has to be taken into consideration, however, is the Young's modulus of both grains. Depending on the inclination of the boundary, the influence of elastic anisotropy will increase until reaching a maximum when the boundary is parallel to the compression direction[33]. A large difference in elastic properties leads to higher stresses in the stiffer grain

and therefore facilitates dislocation source activation in this grain until plastification (depending on available slip systems and their Schmid factors).

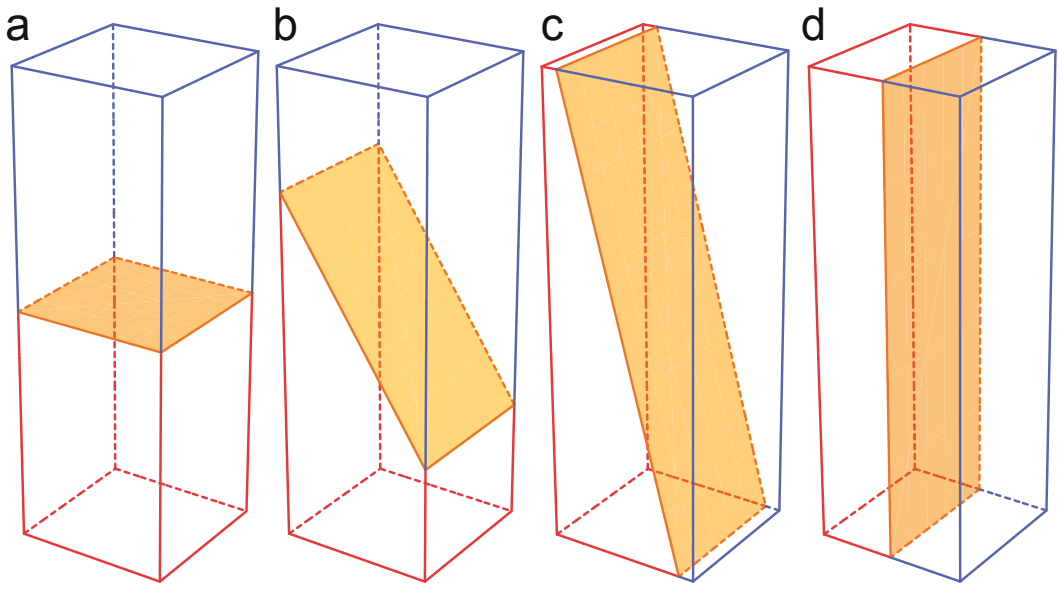

Figure 6.6.: Schematic drawings of general grain boundary orientations in micropillars.

A boundary orientation that makes intersection with the boundary unavoidable, irrespective of aspect ratio is shown in Fig. 6.6 d. In this case the slip plane orientation has only a little influence on the mean free path of the dislocations. Therefore this orientation certainly leads to dislocation-grain boundary interactions and presents the easiest way to assure dislocation-grain boundary interaction.

That being said, the influence of boundaries on the mechanical behavior is also dependent on the boundary type and the activated slip systems. For a fixed misorientation between two grains, slip transmission might be favorable for one pillar orientation and unfavorable for another, simply depending on the activated slip systems that vary with the compression direction[34]. For example, the mechanical response can be the same for a single crystal and a twinned pillar with vertical twin boundary if slip transmission at low threshold stresses is possible[8].

6.5. Summary and Conclusion

Compression experiments on micrometer sized Cu pillars including several inclined twin boundaries on a Si substrate were performed. While multiple slip systems are activated in each pillar, results suggest, that slip parallel to the twin bound-

aries amounts to the biggest part of deformation due to the long mean free paths for dislocation slip and the larger possible dislocation source size. However, testing micropillars with boundaries is an intricate subject. Many factors influence the mechanical behavior of twinned micropillars such as: crystal orientation, available slip systems parallel to the boundary or oriented for easy slip transmission, anisotropy of the Young's modulus, dislocation density, twin lamella spacing and stochastic dislocation source distribution, aggravating the interpretation of dislocation-boundary interactions. The easiest way to investigate dislocation-boundary interactions is to test bicrystals with vertical boundaries. However, the influence of boundaries is dependent on their orientation. Therefore, a thorough analysis of slip systems and Schmid factors and preferably the choice of a single slip orientation are recommended, when specific dislocation-boundary interactions are of interest.

Acknowledgments

Financial support by the Austrian Science Fund (FWF) within project number P24429-N20 is gratefully acknowledged.

References for Chapter 6

[1] E. Hall. The deformation and ageing of mild steel: III discussion of results. *Proceedings of the Physical Society. Section B*, 64(9):747, 1951.

[2] N. Petch. The cleavage strength of polycrystals. *J. Iron Steel Inst*, 174(1):25–28, 1953.

[3] M.D. Uchic, D.M. Dimiduk, J.N. Florando, and W.D. Nix. Sample dimensions influence strength and crystal plasticity. *Science*, 305(5686):986, 2004.

[4] J.R. Greer, W.C. Oliver, and W.D. Nix. Size dependence of mechanical properties of gold at the micron scale in the absence of strain gradients. *Acta Materialia*, 53(6):1821–1830, 2005.

[5] D. Kiener, W. Grosinger, G. Dehm, and R. Pippan. A further step towards an understanding of size-dependent crystal plasticity: In situ tension experiments of miniaturized single-crystal copper samples. *Acta Materialia*, 56(3):580–592, 2008.

[6] C. Motz, T. Schöberl, and R. Pippan. Mechanical properties of micro-sized copper bending beams machined by the focused ion beam technique. *Acta Materialia*, 53(15):4269–4279, 2005.

[7] K.S. Ng and A.H.W. Ngan. Deformation of micron-sized aluminium bi-crystal pillars. *Philosophical Magazine*, 89(33):3013–3026, 2009.

[8] P.J. Imrich, C. Kirchlechner, C. Motz, and G. Dehm. Differences in deformation behavior of bicrystalline Cu micropillars containing a twin boundary or a large-angle grain boundary. *Acta Materialia*, 73(0):240–250, 2014.

[9] M. Schamel. *The influence of interfaces on small-scale mechanical behavior: From fcc metals to polymer/ceramic composites*. PhD thesis, ETH Zurich, 2014.

[10] A. Kunz, S. Pathak, and J.R. Greer. Size effects in Al nanopillars: Single crystalline vs. bicrystalline. *Acta Materialia*, 59(11):4416–4424, 2011.

[11] N. Kheradmand, H. Vehoff, and A. Barnoush. An insight into the role of the grain boundary in plastic deformation by means of a bicrystalline pillar compression test and atomistic simulation. *Acta Materialia*, 61(19):7454–7465, 2013.

[12] N. Kheradmand, A. Barnoush, and H. Vehoff. Investigation of the role of grain boundary on the mechanical properties of metals. *Journal of Physics: Conference Series*, IOP Publishing, 240(1), 2010.

[13] N. Kheradmand and H. Vehoff. Orientation Gradients at Boundaries in Micron-Sized Bicrystals. *Advanced Engineering Materials*, 14(3):153–161, 2012.

[14] L. Lu, X. Chen, X. Huang, and K. Lu. Revealing the maximum strength in nanotwinned copper. *Science*, 323(5914):607, 2009.

[15] S. Zhang, J. Zhou, Y. Wang, L. Wang, and S. Dong. Simulation on the deformation behaviors of nanotwinned Cu considering the angle effect between loading axis and twin boundary. *Computational Materials Science*, 77(0):322–329, 2013c.

[16] D. Jang, X. Li, H. Gao, and J.R. Greer. Deformation mechanisms in nanotwinned metal nanopillars. *Nature Nanotechnology*, 2012.

[17] D. Jang, C. Cai, and J.R. Greer. Influence of Homogeneous Interfaces on the Strength of 500 nm Diameter Cu Nanopillars. *Nano letters*, 2011.

[18] P.J. Imrich, C. Kirchlechner, D. Kiener, and G. Dehm. Internal and external stresses: In situ TEM compression of Cu bicrystals containing a twin boundary. *Scripta Materialia*, 100(0):94–97, 2015.

[19] O. Kraft, P.A. Gruber, R. Mönig, and D. Weygand. Plasticity in confined dimensions. *Annual Review of Materials Research*, 40:293–317, 2010.

[20] C. Kirchlechner, J. Keckes, C. Motz, W. Grosinger, M.W. Kapp, J.S. Micha, O. Ulrich, and G. Dehm. Impact of instrumental constraints and imperfections on the dislocation structure in micron-sized Cu compression pillars. *Acta Materialia*, 59(14):5618–5626, 2011.

[21] P.A. Shade, R. Wheeler, Y.S. Choi, M.D. Uchic, D.M. Dimiduk, and H.L. Fraser. A combined experimental and simulation study to examine lateral constraint effects on microcompression of single-slip oriented single crystals. *Acta Materialia*, 57(15):4580–4587, 2009.

[22] D. Raabe, D. Ma, and F. Roters. Effects of initial orientation, sample geometry and friction on anisotropy and crystallographic orientation changes in single crystal microcompression deformation: A crystal plasticity finite element study. *Acta Materialia*, 55(13):4567–4583, 2007.

[23] T.A. Parthasarathy, S.I. Rao, D.M. Dimiduk, M.D. Uchic, and D.R. Trinkle. Contribution to size effect of yield strength from the stochastics of dislocation source lengths in finite samples. *Scripta Materialia*, 56(4):313–316, 2007.

[24] M.J. Whelan, P.B. Hirsch, R.W. Horne, and W. Bollmann. Dislocations and Stacking Faults in Stainless Steel. *Proceedings of the Royal Society of London. Series A*, 240(1223):524–538, 1957.

[25] Z.H. Jin, P. Gumbsch, E. Ma, K. Albe, K. Lu, H. Hahn, and H. Gleiter. The interaction mechanism of screw dislocations with coherent twin boundaries in different face-centred cubic metals. *Scripta Materialia*, 54(6):1163–1168, 2006.

[26] M. Chassagne, M. Legros, and D. Rodney. Atomic-scale simulation of screw dislocation/coherent twin boundary interaction in Al, Au, Cu and Ni. *Acta Materialia*, 59(4):1456–1463, 2011.

[27] M. Legros, M. Cabié, and D.S. Gianola. In situ deformation of thin films on substrates. *Microscopy Research and Technique*, 72(3):270–283, 2009.

[28] R.-M. Keller, S.P. Baker, and E. Arzt. Quantitative analysis of strengthening mechanisms in thin Cu films: Effects of film thickness, grain size, and passivation. *Journal of Materials Research*, 13(05):1307–1317, 1998.

[29] T.J. Balk, G. Dehm, and E. Arzt. Parallel glide: unexpected dislocation motion parallel to the substrate in ultrathin copper films. *Acta Materialia*, 51(15):4471–4485, 2003.

[30] G. Dehm, T.J. Balk, H. Edongué, and E. Arzt. Small-scale plasticity in thin Cu and Al films. *Microelectronic Engineering*, 70(2-4):412–424, 2003.

[31] H. Zhang, B.E. Schuster, Q. Wei, and K.T. Ramesh. The design of accurate micro-compression experiments. *Scripta Materialia*, 54(2):181–186, 2006.

[32] J.Y. Zhang, G. Liu, and J. Sun. Comparisons between homogeneous boundaries and heterophase interfaces in plastic deformation: Nanostructured Cu micropillars vs. nanolayered Cu-based micropillars. *Acta Materialia*, 61(18):6868–6881, 2013.

[33] I. Tiba, T. Richeton, C. Motz, H. Vehoff, and S. Berbenni. Incompatibility stresses at grain boundaries in Ni bicrystalline micropillars analyzed by an anisotropic model and slip activity. *Acta Materialia*, 83(0):227–238, 2015.

[34] T. Lee, I. Robertson, and H. Birnbaum. Anomalous slip in an FCC system. *Ultramicroscopy*, 29(1):212–216, 1989.

7 Conclusion

Grain boundaries greatly influence the mechanical behavior and can lead to a drastic improvement in mechanical properties in bulk materials. This effect is controlled by the interactions of dislocations with grain boundaries, which is why it is important to investigate the governing mechanisms at the microscale.

Micromechanical experiments conducted on Cu samples in situ in the SEM and TEM illustrate the major differences that grain boundaries can have on the materials behavior. While bicrystalline compression pillars with an arbitrary large angle grain boundary along the compression direction show increased yield strength, pronounced hardening and less serrated flow than single crystals of the constituent crystal orientations, samples with a coherent twin boundary exhibit no change in deformation characteristics. This can be traced back to the dislocation-grain boundary interactions that greatly differ for both grain boundary types.

The tested large angle grain boundary acts as a barrier to dislocation movement, leading to exhaustion hardening and preventing dislocation avalanches to cross the entire sample. The coherent twin boundary on the other hand allows easy slip transfer for specific orientations by dislocation cross-slip due to the symmetric arrangement of slip systems and slip parallel to the twin when the boundary is inclined. This illustrates that many factors including grain boundary type, grain boundary orientation and orientation of slip systems in reference to the grain boundary influence the effect

on the mechanical behavior.

In situ tests inside the TEM provide further insights into dislocation processes, confirm the lack of strengthening in twinned bicrystals and demonstrate that there are no stress concentrations due to twin boundary. Furthermore, they expose the need of truly displacement controlled indenters for the determination of dislocation-grain boundary interactions.

8

List of Publications

8.1. Main Author Papers

1st Publication (Chapter 3)
P. J. Imrich, C. Kirchlechner, C. Motz, G. Dehm
Differences in deformation behavior of bicrystalline Cu micropillars containing a twin boundary or a large-angle grain boundary
Acta Materialia, 73(0):240–250, 2014.

2nd Publication (Chapter 5)
P. J. Imrich, C. Kirchlechner, D. Kiener, G. Dehm
Internal and external stresses: In situ TEM compression of Cu bicrystals containing a twin boundary
Scripta Materialia, 100(0):94–97, 2015.

3rd Publication (Chapter 4)
P. J. Imrich, C. Kirchlechner, D. Kiener, G. Dehm
In situ TEM microcompression of single and bicrystalline samples: insights and limitations
JOM, 2015. (accepted)

4th Publication (Chapter 6)
P. J. Imrich, C. Kirchlechner, G. Dehm
Influence of inclined twin boundaries on the deformation behavior of Cu micropillars (in preparation)

8.2. Co-Author Papers

G. Moser, H. Felber, B. Rashkova, P. J. Imrich, C. Kirchlechner, C. Motz, G. Dehm, D. Kiener
Sample Preparation by Metallography and Focused Ion Beam for Nanomechanical Testing
Practical Metallography, 49(6):343–355, 2012.

C. Kirchlechner, P. J. Imrich, W. Grosinger, M. W. Kapp, J. Keckes, J.-S. Micha, O. Ulrich, O. Thomas, S. Labat, C. Motz, G. Dehm
Expected and unexpected plastic behavior at the micron scale: An in situ μLaue tensile study
Acta Materialia, 60(3): 1252–1258, 2012.

C. Kirchlechner, W. Grosinger, M. W. Kapp, P. J. Imrich, J.-S. Micha, O. Ulrich, J. Keckes, G. Dehm, C. Motz
Investigation of reversible plasticity in a micron-sized, single crystalline copper bending beam by X-ray μLaue diffraction
Philosophical Magazine, 92(25–27):3231–3242, 2012.

D. Kiener, Z. Zhang, S. Šturm, S. Cazottes, P. J. Imrich, C. Kirchlechner, G. Dehm
Advanced nanomechanics in the TEM: effects of thermal annealing on FIB prepared Cu samples
Philosophical Magazine, 92(25–27):3269–3289, 2012.

L. L. Li, X. H. An, P. J. Imrich, P. Zhang, Z. J. Zhang, G. Dehm, Z. F. Zhang
Microcompression and cyclic deformation behaviors of coaxial copper bicrystals with a single twin boundary
Scripta Materialia, 69(2):199–202, 2013.

S. Wurster, R. Treml, M. W. Kapp, E. Langs, M. Alfreider, C. Ruhs, P. J. Imrich, G. Felber, D. Kiener
Novel Methods for the Site Specific Preparation of Micromechanical Structures
Practical Metallography, 52(3):131–146, 2015.

C. Kirchlechner, P. J. Imrich, W. Liegl, J. Pörnbacher, J.-S. Micha, O. Ulrich, C. Motz
On the reversibility of dislocation slip during small scale low cycle fatigue
Acta Materialia, 2015. (accepted)

List of Tables

List of Figures

Appendix

A. Additional Images and Figures

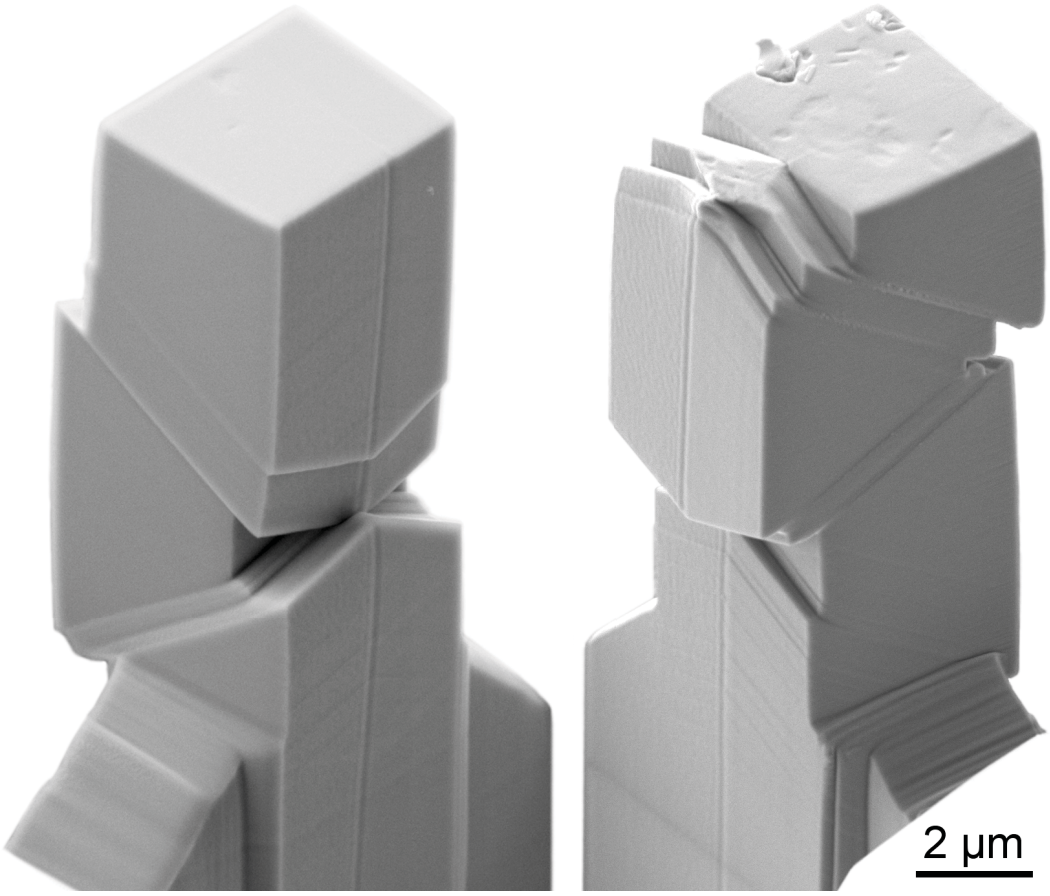

Figure A.1.: Cropped SEM images of compression pillars with twin boundary from chapter 3.

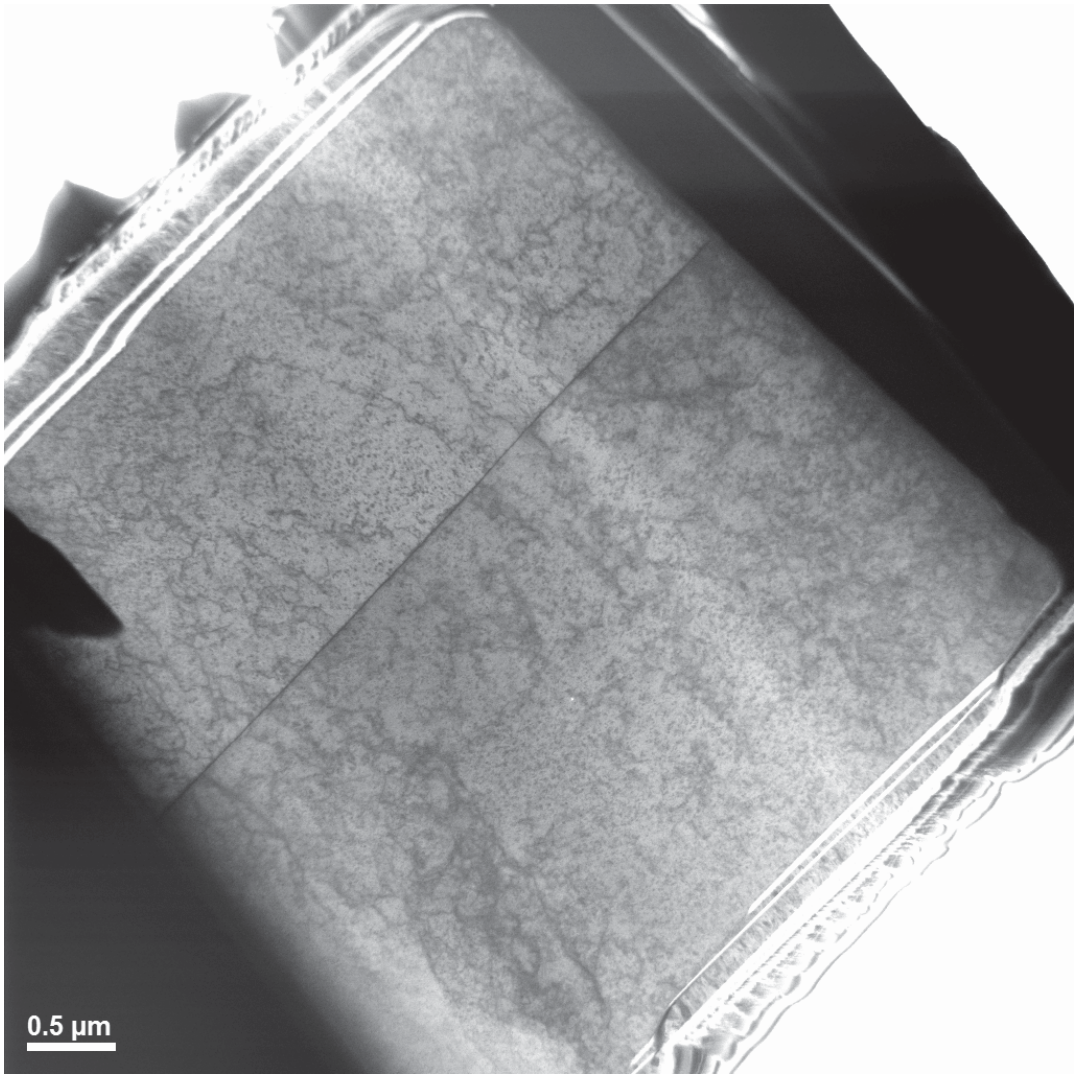

Figure A.2.: STEM image of part of the pillar with twin boundary from chapter 3.

Figure A.3.: Stress-strain comparison of pillars from chapter 3. Green: single crystal and bicrystal from the CTB sample, red: single and bicrystal from the LAGB sample.

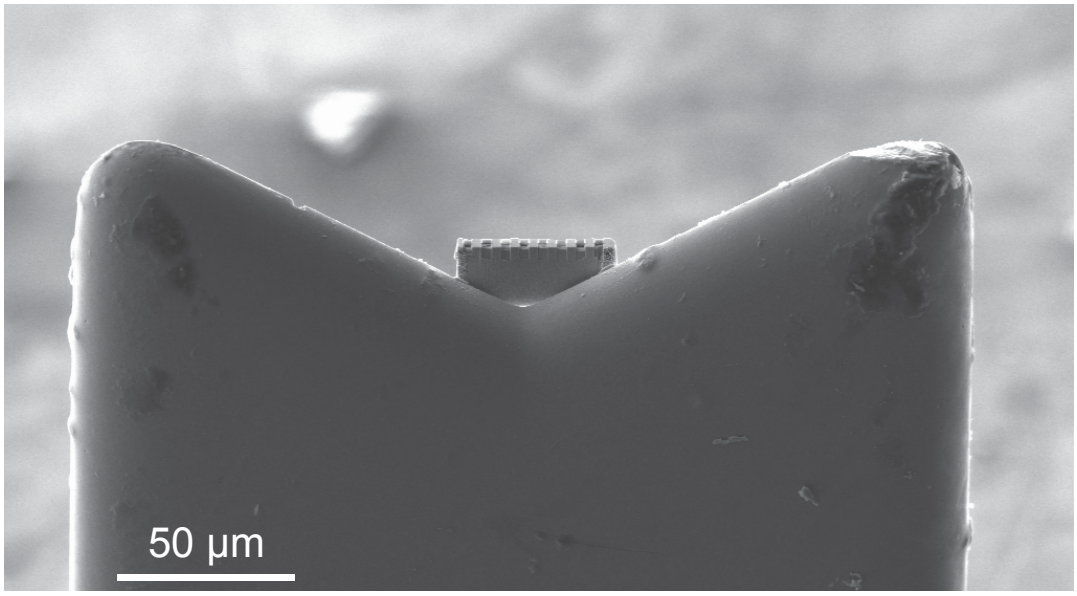

Figure A.4.: SEM overview image of MS2 of chapter 4 and 5 attached to an Omniprobe^{TM} lift-out grid.

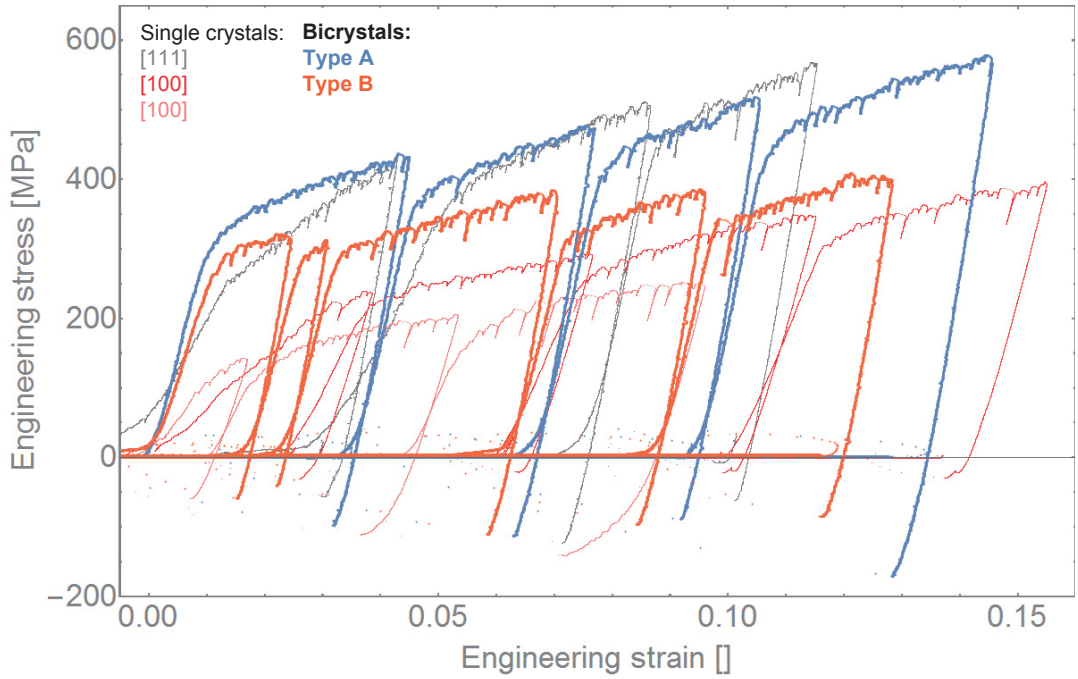

Figure A.5.: Engineering stress-strain curves of single crystals and twinned bicrystals with inclined boundaries from chapter 6.

B. Mathematica Codes

All codes are included digitally on the storage medium located at the end of this thesis.

B.1. Visualization of the atoms and slip systems at a twin boundary

```
SetDirectory[NotebookDirectory[]];
(*List of points for drawing the crystal*)
coord={{1,0,0},{0,1,0},{0,0,1},{1,1,0},{1,0,1},{0,1,1},{1,1,1},{0.5,0.5,0};
{0.5,0.5,1},{0,0.5,0.5},{1,0.5,0.5},{0.5,0,0.5},{0.5,1,0.5}};
numb1={{1,2,3},{1,5,3},{2,6,3},{1,2,4}};
numb2={{1,4,7,5},{2,4,7,6},{3,5,7,6}};
numb3={1,2,3,4,5,6,7,8,9,10,11,12,13};
d=0.09;
opc=0.25;
ops=0.5};

Manipulate[
Graphics3D[{
(*Define planes and atoms in truncated unit cell*)
grp={
{Opacity[opc],EdgeForm[Transparent],
GraphicsComplex[coord,{Polygon[numb1],Polygon[numb2]}]}
};
gra={
{Opacity[ops], GraphicsComplex[coord,{Sphere[numb3,d]}]
}};
(*Draw planes or atoms, when boxes are checked*)
If[p1,{Blue,grp},{Opacity[0],Point[{1,0,0}]}],
If[p2,{Blue,gra},{Opacity[0],Point[{1,0,0}]}],
{Translate[
GeometricTransformation[{
If[p3,{Red,grp},{Opacity[0],Point[{1,0,0}]}],
If[p4,{Red,gra},{Opacity[0],Point[{1,0,0}]}],

If[p5,{Green,Polygon[{{0,1,0},{1,0,0},{1,1,1},{0,1,0}}]},
{Opacity[0],Point[{1,0,0}]}],
```

```
If[p6,{LightGreen,Polygon[{{0,0,1},{0,1,0},{1,1,1},{0,0,1}}]},
{Opacity[0],Point[{1,0,0}]}],
ReflectionMatrix[{1,1,1}]],
{0.67,0.67,0.67}]},
(*Draw slip planes, when boxes are checked*)
If[p5,{Green,Polygon[{{0,1,0},{1,0,0},{1,1,1},{0,1,0}}]},
{Opacity[0],Point[{1,0,0}]}],
If[p6,{LightGreen,Polygon[{{0,0,1},{0,1,0},{1,1,1},{0,0,1}}]},
{Opacity[0],Point[{1,0,0}]}],
(*Move dislocation from one grain to the other*)
If[mov<1,
{Thick,Yellow,Arrowheads[0.05],Arrow[Tube[{{1,1-mov,1-mov},{1-mov,1,1-mov}}]]},
{Translate[GeometricTransformation[{{Thick,Yellow,Arrowheads[0.05],
Arrow[Tube[{{1,-1+mov,-1+mov},{-1+mov,1,-1+mov}}]]}},
ReflectionMatrix[{1,1,1}]],{0.67,0.67,0.67}]}]
},Boxed->False,ImageSize->700],
(*Define checkboxes*)
Style["Crystal 1",12,Bold],
{{p1,True,"Planes"},{True,False}},
{{p2,False,"Atoms"},{True,False}},
Delimiter,
Style["Crystal 2",12,Bold],
{{p3,True,"Planes"},{True,False}},
{{p4,False,"Atoms"},{True,False}},
Delimiter,
Style["Slip Planes",12,Bold],
{{p5,False,"(1,1,-1)"},{True,False}},
{{p6,False,"(-1,1,1)"},{True,False}},
{{mov,0,"move"},0,2}
]
```

Figure B.6.: Interactive visualization of atoms and slip planes at a coherent twin boundary. The Burgers vector of a dislocation that can cross-slip at the twin boundary is shown as yellow arrow.

B.2. Visualization of the TEM bicrystal

```
SetDirectory[NotebookDirectory[]];
(*hkl direction along z-axis (compression direction) in the XYZ sample
coordinate system (SCS)*)
vectcomp1 = {-1, 1, 0};
(*unit vectors of the crystal coordinate system (CCS) axes hkl in the
XYZ SCS*)
vecthp = Normalize[Normalize[{-1, -1, 2}] + Normalize[{1, 1, 1}]];
vectkp = Normalize[Normalize[{-1, -1, 2}] - Normalize[{1, 1, 1}]];
vectlp = Normalize[{1, -1, 0}];
(*Rotation matrix from hkl CCS to XYZ SCS*)
hkltoXYZ = {vecthp, vectkp, vectlp};
(*Transformation Matrix for reflection at (111) plane*)
R = ReflectionMatrix[{1, 1, 1}];
(*List of slip systems: {plane, Burgers vector} *)
slipsys = {
{{1,-1,1},{-1,0,1}},{{1,-1,1},{0,1,1}},{{1,-1,1},{1,1,0}},
{{-1,1,1},{-1,0,-1}},{{-1,1,1},{0,1,-1}},{{-1,1,1},{1,1,0}},
{{1,1,-1},{-1,0,-1}},{{1,1,-1},{0,1,1}},{{1,1,-1},{-1,1,0}},
{{-1,-1,-1},{0,1,-1}},{{-1,-1,-1},{-1,1,0}},{{-1,-1,-1},{-1,0,1}}
};
(*List of points for drawing the sample*)
numbr1={{1,11,12,2,1,5,10,9,6,5},{6,2}};
numbr2={{11,12,2,1,11},{1,2,6,5,1},{1,11,10,5,1},{10,5,6,9,10},{12,2,6,9,12}};
numbr3={{4,11,12,3,4,8,10,9,7,8},{7,3}};
numbr4={{11,4,3,12,11},{11,10,8,4,11},{4,3,7,8,4},{10,8,7,9,10},{12,3,7,9,12}};
numbr5={9,10,11,12,9};
(*Opacity of edges and planes of the sample*)
opl = 1;
opp = 0.05;
factors = {};
zaxis = {{0,0,1},{0,0,1},{0,0,1},{0,0,1}};
(*Calculation of the Schmid factor (in the hkl CCS)*)
schmid1[plane_, burg_] :=  Module[
  {ba, na, fact},
  ba = VectorAngle[vectcomp1, plane];
```

```
  na = VectorAngle[vectcomp1, burg];
  fact = Abs[Cos[na]*Cos[ba]];
  Return[N[fact]];
  ]
(*Intersection between slip planes and edges of the sample
Crystal 1: edges 1-3, crystal 2: edges 2-4
Plane intersects origin and has to be defined solely by plane normal.
Edges are defined by the lower corner and the vector [001]
untersection of plane p.n=0 and line p=point+t*[0,0,1]
substitute p and solve equation*)
intersect[plane_, rotationAngle2_] := Module[
   {points, st, help, t, intersections},
   points = {{3,-1,-3}, {3,1,-3}, intersecttwin[rotationAngle2][[1]],
   intersecttwin[rotationAngle2][[2]], {-3, -1, -3}, {-3, 1, -3}};
   intersections = {};
   For[i = 1, i < 7, i++,
    st = Solve[plane.points[[i]] + t*{0,0,1}.plane == 0, t];
    help = t /. st;
    intersections = Append[intersections, points[[i]] + help[[1]]*{0,0,1}];
    ];
   Return[intersections]
   ];
intersecttwin[rotationAngle_] := Module[
   {points, st, help, t, intersections, plane},

   points = {{-3,1,-3}, {-3,-1,-3}};
   plane = RotationMatrix[rotationAngle, {0,0,1}].hkltoXYZ.{1,1,1};
   intersections = {};
   For[i = 1, i < 3, i++,
    st = Solve[plane.points[[i]] + t*{1,0,0}.plane == 0, t];
    help = t /. st;
    intersections =
     Append[intersections, points[[i]] + help[[1]]*{1,0,0}];
    ];
   Return[intersections]
   ];
(*Calculation of Schmid factors for all slip systems and generation of
```

```
a list that contains the slip systems sorted by descending Schmid factor
e.g. maxSchmid[[1]]...position of slip system with highest Schmid factor
-> slipsys1[[maxSchmid1[[1]]]]...Slip system with highest Schmid factor*)
factors1 = schmid1 @@@ slipsys;
maxSchmid1 = Ordering[factors1, All, Greater];
(*Generate matrix with slip planes and Burgers vectors sorted by
Schmid factor*)
slipburg1 = {};
For[i = 1, i < 13, i++,
  slipburg1 = Append[slipburg1, slipsys[[maxSchmid1[[i]]]]];
  slipburg1 = Append[slipburg1, factors1[[maxSchmid1[[i]]]]];
  ];
(*Display sample and slip systems*)
Manipulate[
 Graphics3D[{
  (*Definition of the coordinates of the sample corners*)
  coords={{3,-1,3}, {3,1,3}, {-3,1,3}, {-3,-1,3},
  {3,-1,-3}, {3,1,-3}, {-3,1,-3}, {-3,-1,-3},
  intersecttwin[rotateCA][[1]], intersecttwin[rotateCA][[2]],
  intersecttwin[rotateCA][[2]] + {0,0,6} intersecttwin[rotateCA][[1]]
  + {0,0,6}};
   (*Define the grains and the boundary*)
   crystal1 = {Blue,
     {Opacity[opp], EdgeForm[Transparent],
      GraphicsComplex[coords, {Polygon[numbr2]}]},
     {Opacity[opl], GraphicsComplex[coords, {Line[numbr1]}]}
     };
   crystal2 = {Red,
     {Opacity[opp], EdgeForm[Transparent],
      GraphicsComplex[coords, {Polygon[numbr4]}]},
     {Opacity[opl], GraphicsComplex[coords, {Line[numbr3]}]}
     };
   boundary = {Yellow,
     {Opacity[0.3], EdgeForm[Transparent],
      Polygon[{intersecttwin[rotateCA][[1]],
        intersecttwin[rotateCA][[2]],
        intersecttwin[rotateCA][[2]] + {0,0,6},
```

```
    intersecttwin[rotateCA][[1]] + {0,0,6}}]},
  {Opacity[opl],
   Line[{intersecttwin[rotateCA][[1]],
    intersecttwin[rotateCA][[2]],
    intersecttwin[rotateCA][[2]] + {0,0,6},
    intersecttwin[rotateCA][[1]] + {0,0,6},
    intersecttwin[rotateCA][[1]]}]}
  };
(*Define the slip systems with highest Schmid factor*)
p13D = {
  {LightBlue, Polygon[intersect[Normalize[
        RotationMatrix[rotateCA, {0,0,1}].hkltoXYZ.slipsys[[
            maxSchmid1[[1]]]][[1]]]
       , rotateCA][[1;;4]] - zaxis*1.3]},
  {Black, Arrow[Tube[{
      intersect[Normalize[
          RotationMatrix[rotateCA, {0,0,1}].hkltoXYZ.slipsys[[
              maxSchmid1[[1]]]][[1]]]
         , rotateCA][[4]] - {0,0,1.3},
      intersect[Normalize[
          RotationMatrix[rotateCA, {0,0,1}].hkltoXYZ.slipsys[[
              maxSchmid1[[1]]]][[1]]]
         , rotateCA][[4]] - {0,0,1.3} -

       RotationMatrix[
         rotateCA, {0,0,1}].hkltoXYZ.slipsys[[maxSchmid1[[1]]]][[
         2]]}]]
   }
  };
p13Dt = {
  LightBlue, Polygon[intersect[Normalize[

       RotationMatrix[
         rotateCA, {0,0,1}].hkltoXYZ.R.slipsys[[
          maxSchmid1[[1]]]][[1]]], rotateCA][[3;;6]] - zaxis*1.3]
  };
```

```
p23D = {
  {LightBlue, Polygon[intersect[Normalize[
        RotationMatrix[rotateCA, {0,0,1}].hkltoXYZ.slipsys[[
            maxSchmid1[[4]]]][[1]]]
       , rotateCA][[1;;4]] + zaxis*1.3]},
  {Black, Arrow[Tube[{
      intersect[Normalize[
          RotationMatrix[rotateCA, {0,0,1}].hkltoXYZ.slipsys[[
              maxSchmid1[[4]]]][[1]]],rotateCA][[4]] + {0,0,1.3},
      intersect[Normalize[
          RotationMatrix[rotateCA, {0, 0, 1}].hkltoXYZ.slipsys[[
              maxSchmid1[[4]]]][[1]]], rotateCA][[4]] + {0,0,1.3} +
       RotationMatrix[
         rotateCA, {0,0,1}].hkltoXYZ.slipsys[[maxSchmid1[[4]]]][[2]]}]]
   }
  };
p23Dt = {
  LightGreen, Polygon[intersect[Normalize[

       RotationMatrix[
         rotateCA, {0,0,1}].hkltoXYZ.R.slipsys[[
          maxSchmid1[[4]]]][[1]]], rotateCA][[3;;6]] + zaxis*1.3]
  };
(*Draw both grains and the boundary*)
Rotate[{crystal1, crystal2, boundary}, spin, {0,0,1}],
(*Draw the slip systems if the checkbox is checked*)‘
If[p1,
 {Rotate[{p13D, p13Dt}, spin, {0,0,1}]},
 {Opacity[0], Point[{1,0,0}]}],
If[p2,
 {Rotate[{p23D, p23Dt}, spin, {0, 0, 1}]},
 {Opacity[0], Point[{1,0,0}]}],
If[p3, {
  {Gray, Arrow[{{0,0,0}, {1,0,0}}], Text["X", {1,0,0}],
   Arrow[{{0,0,0}, {0,1,0}}], Text["Y", {0,1,0}],
   Arrow[{{0,0,0}, {0,0,1}}], Text["Z", {0,0,1}]
   },
```

```
    {Opacity[0], Point[{1,0,0}]}],
  (*Draw transparent sphere for visualization with minimum size
  change during rotation*)
  {Opacity[0], Sphere[{0,0,0}, 3.2]}
  },
 Boxed -> False, ImageSize -> 700, ViewAngle -> All,
 RotationAction -> "Clip", SphericalRegion -> True,
 ViewPoint -> {0,-4,0}],
(*Define Checkboxes*)
{{p1, False, slipsys[[maxSchmid1[[1]]]]}, {True, False}},
{{p2, False, slipsys[[maxSchmid1[[4]]]]}, {True, False}},
Delimiter,
{{rotateCA, 0.169646, "Rotate around compression direction"}, -Pi/8, Pi*5/8},
{{spin, 0, "Rotate the sample"}, -Pi/5, Pi/5},
{{p3, False, "Coordinate axes"}, {True, False}}
]
```

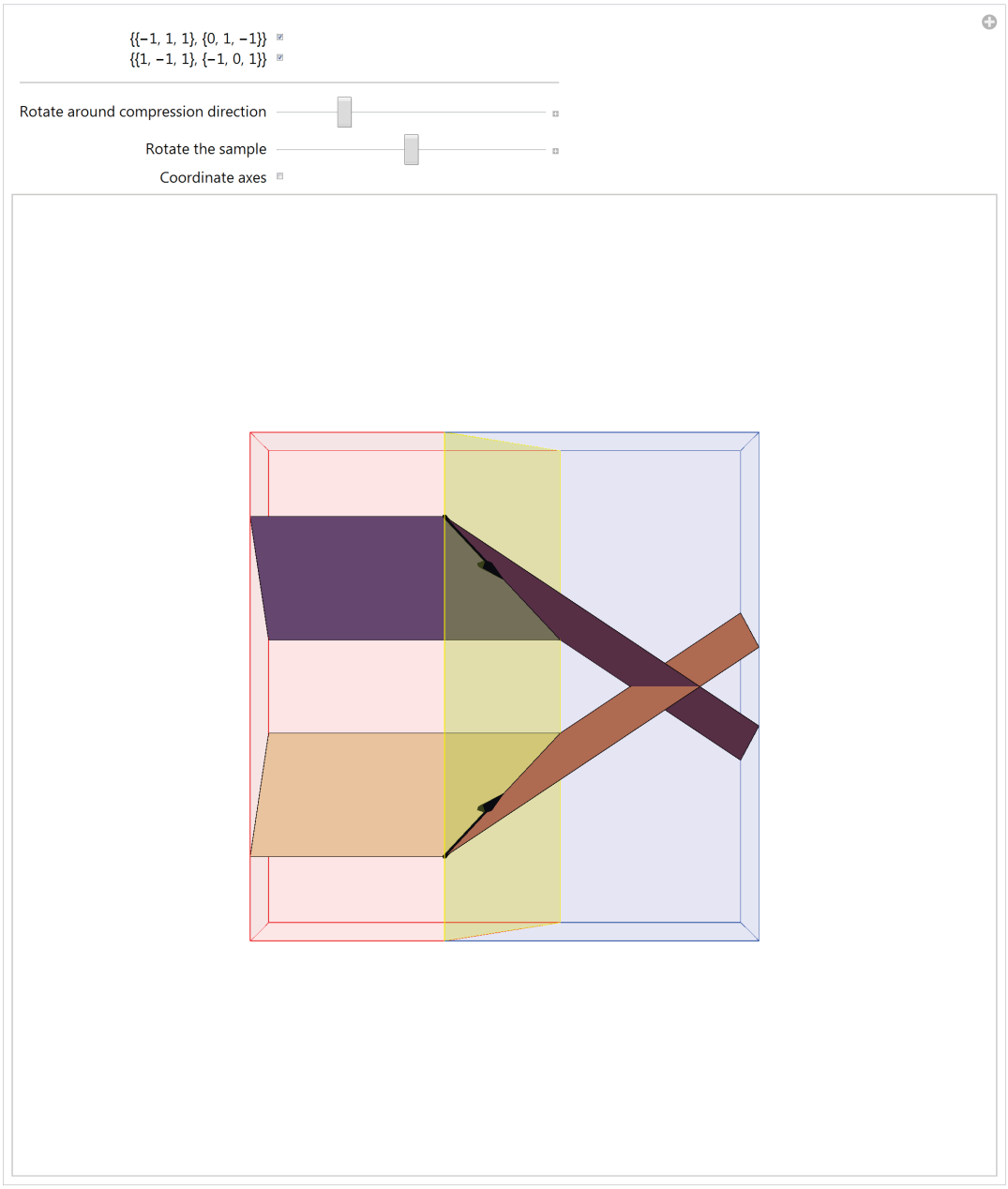

Figure B.7.: Interactive visualization of the TEM bicrystals from chapter 4 and 5 using Mathematica including the two slip systems with highest Schmid factor and Burgers vector parallel to the twin boundary.

B.3. Visualization of the LAGB bicrystal

```
SetDirectory[NotebookDirectory[]];
(*hkl directions along z-axis (compression direction) in the ABC sample
coordinate system (SCS)*)
vectcomp1={0.954087,0.299386,-0.00921794};
vectcomp2={0.968598,-0.0147054,-0.248199};
(*unit vectors of the crystal coordinate system (CCS) axes hkl in the
 XYZ SCS*)
vecth1p={0.954087,-0.296254,0.0441687};
vectk1p={0.299386,0.947748,-0.110185};
vectl1p={-0.00921794,0.11835,0.992929};
vecth2p={0.968598,0.0325104,0.246499};
vectk2p={-0.0147054,0.99717,-0.0737315};
vectl2p={-0.248199,0.0677913,0.966334};
rotAxisp={0.01625163464069407,-0.5245746552300102,0.8512088744912316};
(*J1: Rotation from CCS hkl1 to SCS ABC,
J12: Rotation from CCS hkl1 to CCS hkl2,
TM: Rotation from SCS ABC to display coordinate system (DCS) XYZ,
XYZ1: Rotation from CCS hkl1 to DCS XYZ,
XYZ2: Rotation from CCS hkl2 to DCS XYZ *)
J1={{0.954087,0.299386,-0.00921794},{-0.296254,0.947748,0.11835},
{0.0441687,-0.110185,0.992929}};
J2={{0.968598,-0.0147054,-0.248199},{0.0325104,0.99717,0.0677913},
{0.246499,-0.0737315,0.966334}};
J12={{0.9253829643657,0.29363585509219997,0.23967513316288},
{-0.31270245665385005,0.9487873876031,0.044940478431375996},
{-0.21420516655740002,-0.1165337486116,0.96981203613106}};
TM={{0,1/Sqrt[2],1/Sqrt[2]},{0,-(1/Sqrt[2]),1/Sqrt[2]},{1,0,0}};
XYZ1=TM.J1;
XYZ2=TM.J2;
(*List of slip systems: {plane, Burgers vector} *)
slipsys={
{{1,-1,1},{-1,0,1}},{{1,-1,1},{0,1,1}},{{1,-1,1},{1,1,0}},
{{-1,1,1},{-1,0,-1}},{{-1,1,1},{0,1,-1}},{{-1,1,1},{1,1,0}},
{{1,1,-1},{-1,0,-1}},{{1,1,-1},{0,1,1}},{{1,1,-1},{-1,1,0}},
{{-1,-1,-1},{0,1,-1}},{{-1,-1,-1},{-1,1,0}},{{-1,-1,-1},{-1,0,1}} };
```

```
(*List of points for drawing the sample*)
coord={{1,-1,3},{1,1,3},{-1,1,3},{-1,-1,3},
{1,-1,-3},{1,1,-3},{-1,1,-3},{-1,-1,-3}};
numb1={6,2,3,7,6,5,1,2};
numb2={{1,2,3,1},{1,5,6,2,1},{3,2,6,7,3},{5,6,7,5}};
numb3={8,4,3,7,8,5,1,4};
numb4={{1,4,3,1},{1,5,8,4,1},{3,4,8,7,3},{5,8,7,5}};
numb5={1,5,7,3,1};
(*Opacity of edges and planes of the sample*)
opc=1;
ops=0.05;
factors={};
(*Calculation of the Schmid factor (in the hkl CCS)*)
schmid1[plane_,burg_]:=  Module[
{ba,na,fact},
ba=VectorAngle[vectcomp1,plane];
na=VectorAngle[vectcomp1,burg];
fact=Abs[Cos[na]*Cos[ba]];
Return[N[fact]];
]
schmid2[plane_,burg_]:=  Module[
{ba,na,fact},
ba=VectorAngle[vectcomp2,plane];
na=VectorAngle[vectcomp2,burg];
fact=Abs[Cos[na]*Cos[ba]];
Return[N[fact]];
]
(*Intersection between slip planes and edges of the sample
Crystal 1: edges 1-3, crystal 2: edges 2-4
Plane intersects origin and has to be defined solely by plane normal.
Edges are defined by the lower corner and the vector [001]
intersection of plane p.n=0 and line p=point+t*[0,0,1]
substitute p and solve equation*)
intersect[plane_]:=Module[
{points,st,help,t,intersections},
points={{1,1,-3},{1,-1,-3},{-1,1,-3},{-1,-1,-3}};
intersections={};
```

```
For[i=1,i<5,i++,
st=Solve[plane.points[[i]]+t*{0,0,1}.plane==0,t];
help=t/.st;
intersections=Append[intersections,points[[i]]+help[[1]]*{0,0,1}];
];
Return[intersections]
]
(*Calculation of Schmid factors for all slip systems and generation
of a list that contains the slip systems sorted by descending
Schmid factor e.g. maxSchmid[[1]]...position of slip system with
highest Schmid factor -> slipsys1[[maxSchmid1[[1]]]]...Slip system
with highest Schmid factor*)
factors1=schmid1@@@slipsys;
maxSchmid1=Ordering[factors1,All,Greater];
factors2=schmid2@@@slipsys;
maxSchmid2=Ordering[factors2,All,Greater];
(*Generate matrix with slip planes and Burgers vectors sorted by Schmid factor*)
slipburg1={};
slipburg2={};
For[i=1,i<13,i++,
slipburg1=Append[slipburg1,slipsys[[maxSchmid1[[i]]]]];
slipburg1=Append[slipburg1,factors1[[maxSchmid1[[i]]]]];
slipburg2=Append[slipburg2,slipsys[[maxSchmid2[[i]]]]];
slipburg2=Append[slipburg2,factors2[[maxSchmid2[[i]]]]];
];
(*Display sample and slip systems*)
Manipulate[
Graphics3D[{
(*Define the grains and the boundary*)
crystal1={
{Opacity[ops],EdgeForm[Transparent],GraphicsComplex[coord,{Polygon[numb2]}]},
{Opacity[opc],GraphicsComplex[coord,{Line[numb1]}]}
};
crystal2={
{Opacity[ops],EdgeForm[Transparent],GraphicsComplex[coord,{Polygon[numb4]}]},
{Opacity[opc],GraphicsComplex[coord,{Line[numb3]}]}
};
```

```
boundary={
{Opacity[0.3],EdgeForm[Transparent],GraphicsComplex[coord,{Polygon[numb5]}]},
{Opacity[opc],GraphicsComplex[coord,{Line[numb5]}]}
};
(*Draw the grains and the boundary*)
{Blue,crystal1},
{Red,crystal2},
{Yellow,boundary},
(*Define the slip systems with highest Schmid factor*)
p1D={
{Green,Polygon[intersect[XYZ1.slipsys[[maxSchmid1[[1]]]][[1]]][[1;;3]]]},
{Black,Arrow[Tube[{intersect[XYZ1.slipsys[[maxSchmid1[[1]]]][[1]]][[1]],
intersect[XYZ1.slipsys[[maxSchmid1[[1]]]][[1]]][[1]]-
XYZ1.slipsys[[maxSchmid1[[1]]]][[2]]}]]}
};
p2D={
{LightGreen,Polygon[intersect[XYZ1.slipsys[[maxSchmid1[[2]]]][[1]]][[1;;3]]]},
{Black,Arrow[Tube[{intersect[XYZ1.slipsys[[maxSchmid1[[2]]]][[1]]][[1]],
intersect[XYZ1.slipsys[[maxSchmid1[[2]]]][[1]]][[1]]+
XYZ1.slipsys[[maxSchmid1[[2]]]][[2]]}]]}
};
p3D={
{Red,Polygon[intersect[XYZ1.slipsys[[maxSchmid1[[3]]]][[1]]][[1;;3]]]},
{Black,Arrow[Tube[{intersect[XYZ1.slipsys[[maxSchmid1[[3]]]][[1]]][[2]],
intersect[XYZ1.slipsys[[maxSchmid1[[3]]]][[1]]][[2]]-
XYZ1.slipsys[[maxSchmid1[[3]]]][[2]]}]]}
};
p4D={
{Green,Polygon[intersect[XYZ2.slipsys[[maxSchmid2[[1]]]][[1]]][[2;;4]]]},
{Black,Arrow[Tube[{intersect[XYZ2.slipsys[[maxSchmid2[[1]]]][[1]]][[3]],
intersect[XYZ2.slipsys[[maxSchmid2[[1]]]][[1]]][[3]]+
XYZ2.slipsys[[maxSchmid2[[1]]]][[2]]}]]}
};
p5D={
{LightGreen,Polygon[intersect[XYZ2.slipsys[[maxSchmid2[[2]]]][[1]]][[2;;4]]]},
{Black,Arrow[Tube[{intersect[XYZ2.slipsys[[maxSchmid2[[2]]]][[1]]][[2]],
intersect[XYZ2.slipsys[[maxSchmid2[[2]]]][[1]]][[2]]-
```

```
XYZ2.slipsys[[maxSchmid2[[2]]]][[2]]}]]}
};
p6D={
{Red,Polygon[intersect[XYZ2.slipsys[[maxSchmid2[[3]]]][[1]]][[2;;4]]]},
{Black,Arrow[Tube[{intersect[XYZ2.slipsys[[maxSchmid2[[3]]]][[1]]][[4]],
intersect[XYZ2.slipsys[[maxSchmid2[[3]]]][[1]]][[4]]+
XYZ2.slipsys[[maxSchmid2[[3]]]][[2]]}]]}
};
p7D={
{Gray,Arrow[{{0,0,0},{1,0,0}}],Text["X",{1,0,0}],
Arrow[{{0,0,0},{0,1,0}}],Text["Y",{0,1,0}],
Arrow[{{0,0,0},{0,0,1}}],Text["Z",{0,0,1}]}
};
(*Define the slip systems with highest Schmid factor*)
If[p1,p1D,{Opacity[0],Point[{1,0,0}]}],
If[p2,p2D,{Opacity[0],Point[{1,0,0}]}],
If[p3,p3D,{Opacity[0],Point[{1,0,0}]}],
If[p4,p4D,{Opacity[0],Point[{1,0,0}]}],
If[p5,p5D,{Opacity[0],Point[{1,0,0}]}],
If[p6,p5D,{Opacity[0],Point[{1,0,0}]}],
If[p7,p7D,{Opacity[0],Point[{1,0,0}]}]
},
Boxed->False,ImageSize->350
],
(*Draw the slip systems if the checkbox is checked*)
Style["Crystal1 (blue):",12,Bold],
{{p1,True,slipsys[[maxSchmid1[[1]]]]},{True,False}},
{{p2,True,slipsys[[maxSchmid1[[2]]]]},{True,False}},
{{p3,False,slipsys[[maxSchmid1[[3]]]]},{True,False}},
Delimiter,
Style["Crystal2 (red):",12,Bold],
{{p4,True,slipsys[[maxSchmid2[[1]]]]},{True,False}},
{{p5,True,slipsys[[maxSchmid2[[2]]]]},{True,False}},
{{p6,False,slipsys[[maxSchmid2[[3]]]]},{True,False}},
Delimiter,
{{p7,False,"Coordinate axes"},{True,False}}
]
```

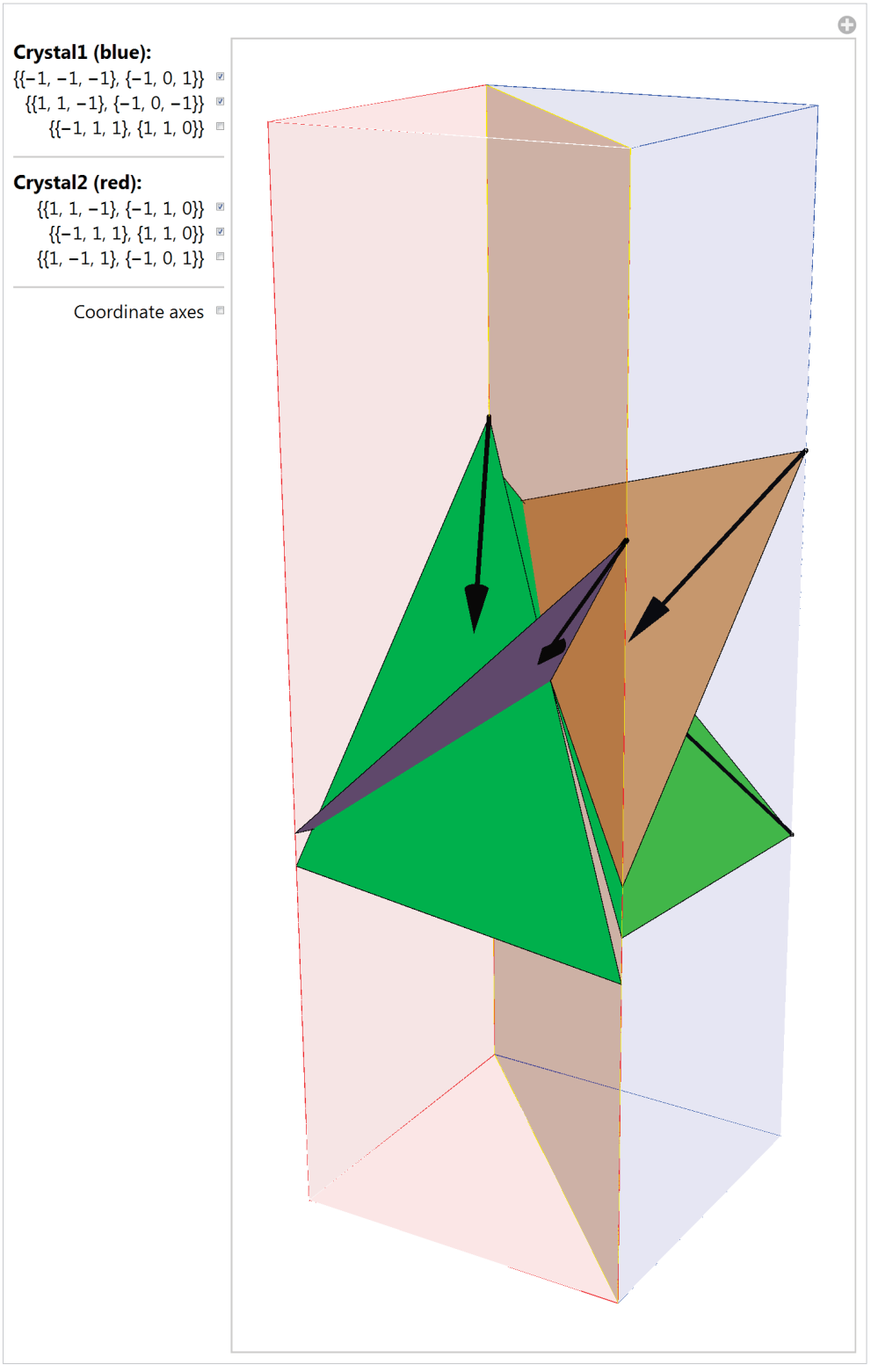

Figure B.8.: Interactive visualization of the LAGB bicrystal from chapter 3 using Mathematica including the two slip systems with highest Schmid factor and corresponding Burgers vectors for each grain.